Electrochemically tunable mechanical behavior of bulk nanoporous gold/polypyrrole

Vom Promotionsausschuss der
Technischen Universität Hamburg
zur Erlangung des akademischen Grades

Doktor-Ingenieur (Dr.-Ing.)

genehmigte Dissertation

von
Jie Li

aus
Zaozhuang, China

2021

Promotionskommission

Erstgutachter: *Prof. Dr.-Ing. Jörg Weißmüller, Technischen Universität Hamburg*

Zweitgutachter: *Prof. Dr. rer. nat. Patrick Huber, Technischen Universität Hamburg*

Vorsitzender: *Prof. Dr.-Ing. Robert Meißner, Technischen Universität Hamburg*

Tag der mündlichen Prüfung: *18 June 2021*

Acknowledgments

I would like to thank everyone who has encouraged and helped me during my study in Germany. Without their help, the study and dissertation would not be finished.

First of all, I honestly thank Prof. Dr.-Ing. Jörg Weißmüller and Dr. Nadiia Mameka for the opportunity to join our team. I want to especially express my thankfulness to Dr. Nadiia Mameka who guides my daily research. Under their supervision, I gained a lot of research experience. Besides, Nadiia has also taught me a lot of life skills and work skills that make me group up. I am so grateful for her kind patience.

I also want to thank Dr. Jürgen Markmann. He has inspired me a lot during our group meetings. His kind help with the lab greatly facilitated my work.

Sincerely gratitude to our colleagues at Helmholtz-Zentrum Geesthacht and Technische Universität Hamburg: Xinyan Wu, Lukas Lührs, Benedikt Roschning, Shan Shi, Yong Li, Nam Ngô, Stefan Berger, and Yijuan Wu. Thank you for sharing your knowledge and your discussions these years. I am also grateful to Manuel Brinker who helped me with AFM measurement, as well as Jens Timmermann who helped me with SEM work. Besides, I want to appreciate Dr. Lingzhi Liu (Institute of Metal Research, Shenyang, China) for his discussion.

Thanks to Mrs. Stephanie Koch and Mrs. Haide Alfort-Springer for their kind help with official matters. I am obliged to Mr. Peter Kummerrow and Mr. Uwe Benn for their assistance with the visa extension.

I am also grateful for the finical support from China Scholarship Council (CSC), Helmholtz-Zentrum Geesthacht, and German Research Foundation (DFG) within the Collaborative Research Initiative SFB 986 Tailor-Made Multi-Scale Materials Systems-M^3.

I also appreciate the beautiful time with Miss Pan. I will never forget your bright eyes at the first glance at Rothe Erde. Thank you very much for your appearance in my life and I wish you all the best in your future.

At last, I would like to thank my family for their love, patience, and encouragement throughout my study.

Abstract

This thesis explores the viscoelastic modulus and actuation behavior of an electroactuator based on nanoporous gold coated with polypyrrole film (NPG/PPy). The experiments were performed using *in situ* dynamic mechanical analysis under electrochemical control. Novel mechanical responses of NPG/PPy hybrids have been revealed.

First, during the potential sweep, a reversible change in effective elastic modulus of the NPG/PPy hybrid is observed, characterized by alternating stiffening-softening features. This non-monotonous modulus response of NPG/PPy hybrids is different from the linear modulus behavior as a function of electrode potential of non-coated NPG. Moreover, the amplitude of the modulus variations increases with PPy thickness, showing a 7-fold increase for the thickest PPy film (~ 40 nm) coated NPG as compared to non-coated NPG. It has been suggested that the modulus behavior strongly correlates with the processes in PPy matrix during doping and dedoping of the polymer. The competition between the enhanced intermolecular bonding due to the charged polymer chains-anion interactions and softening of PPy caused by the incorporated solvent has been suggested to lead to the non-monotonous modulus behavior.

Second, the actuation strains of NPG/PPy electroactuator under both potential jumps and potential sweeps have been found to be invariant under increasing applied load. The actuation strain of NPG/PPy hybrids comprises of two parts: The free stroke induced by the swelling of PPy which is independent of load and the strain caused by the stiffness variations which is load-dependent. The findings of the modulus behavior mentioned above help to distinguish the strain contributions of these two factors to the total strain. These experiments allow evaluating a contribution of the electrochemically modulated elastic modulus of NPG/PPy to the actuation strain. Depending on the predeformation of the material as well as on the oxidation or reduction state of PPy, this contribution adds an expansion or contraction to the actuation strain. Yet, in the range of the applied loads tested, the actual performance is not affected by the load, demonstrating an enhanced load-bearing efficiency of NPG/PPy electroactuators in contrast to non-coated NPG.

Zusammenfassung

Diese Arbeit untersucht den viskoelastischen Modul und das Funktionsverhalten eines Elektroaktuators auf der Basis von nanoporösem Gold, das mit einem Polypyrrolfilm (NPG/PPy) beschichtet wurde. Die Versuche wurden mittels dynamisch-mechanischer in-situ Analyse unter elektrochemischer Kontrolle durchgeführt. Neuartige mechanische Reaktionen auf Änderungen des elektrochemischen Potentials von NPG/PPy-Hybriden wurden entdeckt.

Erstens wurde eine reversible Änderung des effektiven Elastizitätsmoduls des NPG/PPy-Hybriden während eines Potentialdurchlaufs beobachtet, die sich durch abwechselndes Versteifungs- und Erweichungsverhalten auszeichnet. Diese nicht-monotone Modulantwort als Funktion des Elektrodenpotentials von NPG/PPy-Hybriden unterscheidet sich von dem linearen Modulverhalten von nicht beschichtetem NPG. Außerdem nimmt die Amplitude der Modulvariationen mit der Dicke der PPy-Schicht zu und zeigt eine siebenfache Erhöhung für das mit dem dicksten PPy-Film (~ 40 nm) beschichteten NPG im Vergleich zu nicht beschichtetem NPG ergänze Zahlen für die Dicke. Es wurde Nahe gelegt, dass das Modulverhalten stark mit den Vorgängen in der PPy-Matrix während der Dotierung und Entdotierung des Polymers korreliert. Konkret wurde die Konkurrenz zwischen der verbesserten intermolekularen Bindung aufgrund der Wechselwirkungen zwischen geladenen Polymerketten und eingelagerten Anionen als versteifendem Mechanismus und die Plastifizierung von PPy durch das vermehrt eingelagerte Lösungsmittel als erweichendem Mechanismus vorgeschlagen, um das nicht-monotone Modulverhalten zu erklären.

Zweitens wurde festgestellt, dass die aktorischen Dehnungen des Elektroaktuators NPG/PPy sowohl bei Potentialsprüngen als auch bei kontinuierlichen Potenzialverläufen unter zunehmender Last invariant sind. Die aktorische Dehnung von NPG/PPy-Hybriden besteht aus zwei Teilen: Der freie durch die Schwellung von PPy induzierte Hub, der unabhängig von der Belastung ist, und Dehnungen, die durch die Veränderung der Steifigkeit des Hybriden unter Last verursacht werden. Die Erkenntnisse über das oben erwähnte Verhalten des Moduls helfen bei der Unterscheidung der Dehnungsbeiträge dieser beiden Faktoren auf die Gesamtdehnung. Die hier durchgeführten Experimente ermöglichen die Bestimmung des Beitrags des elektrochemisch modulierten Elastizitätsmoduls von NPG/PPy zur Gesamtdehnung. Abhängig von der Vorverformung des Materials sowie vom Oxidations- oder Reduktionszustand des PPy, fügt dieser Beitrag eine Expansion oder Kontraktion zur Gesamtdehnung hinzu. Doch im Bereich der getesteten aufgebrachten Lasten ist die tatsächliche aktorische Dehnung durch die Belastung nicht beeinträchtigt, was eine verbesserte Effizienz von NPG/PPy-Elektroaktuatoren im Vergleich zu nicht beschichtetem NPG aufzeigt.

Contents

List of Figures

Chapter 1

Introduction

1.1 Motivation and background

Actuator materials change their dimensions upon converting external electrical, electrochemical, and thermal energy to mechanical work. The advantages of low operating voltage, good electrochemical cycling stability, and large actuation strain make conducting polymers (CPs) one the most studied electroactuator material [1–8]. Yet, the relatively large creep, small load-bearing capacity, and low stiffness restrict the functionality and application domains of CPs [8–16]. Elaborately tailoring the microstructure and components will improve the performance of CPs. Generation of crosslinks in matrix improves the creep resistance, strength, and elastic modulus of CPs [12, 17, 18]. The modulus could also be promoted by decreasing the characteristic size of CPs fibers [13]. Besides, the mechanical strength could be enhanced by constructing CPs with another component with high strength, such as carbon nanotube, metal helix, and stiff polymer [1, 15, 16, 19, 20]. Recently, mm-sized nanoporous gold (NPG), a conductive skeleton with considerable strength and stiffness [21–28], has served as another reinforcing framework of polypyrrole (PPy) electroactuator [29, 30]. Taking merits of both NPG and PPy, NPG/PPy hybrids have shown promising potential as electroactuators with enhanced strength, stiffness, and actuation strain during electrochemical redox processes in contrast to the individual component.

In addition to the dimension change, the modulus behavior of the electroactuator materials has also been found to vary during the courses of electrochemical oxidation and reduction processes. According to Hooke's law, a strain is obtained under a certain load. Therefore, the variation of elastic Young's modulus during electrochemical redox processes allows one to understand the actuation of an electroactuator by evaluating the strain contribution of elastic Young's modulus variation and consequently, figuring out the strain contributed by electrochemical redox processes. Based on the modulus behavior of PPy and NPG [9, 14, 21, 31–38], the elastic Young's modulus variation of NPG/PPy hybrid electroactuators under electrochemical conditions are expected. However, the corresponding studies are not available. This thesis will figure out the Young's modulus behavior of NPG/PPy electroactuators during electrochemical redox processes and the underlying mechanism of the modulus change. Moreover, the ability of NPG/PPy electroactuators to work against load and the contribution of modulus variation under various loads are also studied in this thesis.

1.1.1 Dealloying-derived nanoporous metals

Nanoporous (np) metals have drawn increasing attention as functional materials and have shown applications in a variety of fields, including sensors [39, 40], catalysts [41–43], bioanalytical systems [44, 45], energy storage [46–48], and actuators [40, 49–56]. These applications in turn require further studies for a better understanding of np metals, such as synthesis, fundamental mechanism, and possible ways to further improve their performance.

Np metals can be fabricated by means of many techniques.

The template-based method is a powerful way to make np metals. This method starts with the preparation of a template, for instance, porous anodic alumina (PAA) or copolymer [57, 58], followed by a deposition of the target metal or alloys (e.g., Ni and PtCu [57, 58]). After removing the template introduced at the first step, the np metals will be formed. One of the limitations of this method is introducing various templates which will be removed later. Moreover, the final morphology and microstructure of np metals strongly depend on the templates.

Another approach to developing np metals is the assembly method which makes use of the reactions between metal ions and electrolyte. During the process, the metal salts will be reduced and np metal sponges will be formed [59]. Compared to the template-based method, the porous structure will form in a random way during the assembly process, leading to an unordered structure.

A reduction-induced decomposition (RID) has been proposed to make homogeneous or even hierarchical porous structure [60]. The anion component will be dissolved and the cation-turned metal atoms will stay as the porous metal structure. RID-based fabrication allows more options for the selection of precursor alloys.

Galvanic replacement reaction (GRR) has been applied to fabricate np Al [61]. The replacement reaction between the more active component (Mg in Al_2Mg_3 and even pure Mg) and the surrounding salt precursor (ionic liquid containing $Al_2Cl_7^-$) will lead to the formation of np Al skeleton, and meanwhile a homogeneous deposition of Al that will thicken the existing skeleton. This GRR strategy provides a facial route to fabricate np metal with relatively high chemical activity and avoid the oxidation which would occur during dealloying in an aqueous electrolyte.

The other way to make np metals with high chemical activity is liquid-metal dealloying. Through the solidification of the melt liquid and the alloy component that will be sacrificed and the later chemical etching during which the melt is removed, np Ti, Nb, Fe, and Si could be obtained [62, 62]. Yet, this method is conducted at high temperature and the porous structures will be coarsened. A vapor-phase dealloying (VPD) method has been developed to produce np metals with high chemical activity [63]. This method selectively evaporates a component which has a low vapor pressure from an alloy. By tailoring the VPD time, temperature, and pressure, np metals with a fine porous structure will be obtained.

Even the majority of methods mentioned above, chemical and electrochemical dealloying have been the most common methods to fabricate np metals in the last two decades. The dealloyed np metals are fabricated by selectively dissolving the less noble elements from a precursor alloy [64, 65] (section 2.1). A number of np materials have been successfully fabricated by chemical dealloying or electrochemical dealloying, such as np Au, Ag, Pd, Pt, and Cu [26, 50, 66–69].

Electrochemical dealloying allows one to yield crack-free np metals with a dimension of mm-scale [21, 26, 50, 52, 70–72], which is the prerequisite for studying the

mechanical properties through conventional macroscopic mechanical tests. Moreover, the dealloying-derived np metals are essentially a 3D bicontinuous network of nanoscaled ligaments with a uniform size that can be tuned down to well below 10 nm, giving rise to high strength and stiffness [21–28]. These advantages make np metal, in particular np Au, a model material in studying the mechanical functionality. Besides, small ligaments also lead to a large surface area to volume ratio and a large fraction of surface atoms [73]. The interactions between surface atoms in a np metal and environments are significant and will dominate the overall material behavior. In other words, chemically or electrochemically modulating the surface conditions allows to modify the physical and chemical properties and to realize the material's functionality, for instance, actuation.

1.1.2 Electrochemically driven nanoporous metal actuators

An electroactuator will convert electric energy to mechanical deformation of the actuator material. A number of electroactuator materials have been explored, such as carbon nanotubes [20, 74], conducting polymers [1–8], piezoelectric ceramics [39, 75], and np metals [40, 49–56]. The good mechanical strength and stiffness, high conductivity, low operating voltage, and the bulk volume make np metals more promising electroactuators under compressive loading.

The actuation properties have been exploited under various conditions (e.g., in an electrochemical environment or alternative oxidizing-reducing atmosphere) on np Au (NPG), Ag, Pd, Pt, and Au-Pt alloy [31, 49–52, 54–56, 73, 76–79]. In the case of exposing NPG in oxidizing and reducing gases [54], the difference in surface stress of clean and oxygen-covered Au ligaments surfaces results in macroscopic strain response. This adsorbate-induced surface stress change converts chemical energy directly to mechanical response. When wetted by electrolyte, surface charge density and adsorbate coverage on the metal ligaments will be reversibly varied versus the applied potential. The space charge confined to the outermost layer of the atoms will lead to a significant change of surface atoms bonding and consequently, resulting in lateral attractive (or repulsive) interaction between surface atoms. The change of surface stress will be balanced by the stress in bulk, and therefore, the strain needed to produce this stress is the observed macroscopic actuation [31, 49–52, 55, 78, 79].

In addition to the surface chemistry induced actuation, hydrogen (H) moving in (and out of) Pd lattice will give rise to large macroscopic dimension change [56, 76, 77]. A remarkable strain of ~ 4% has been found for np Pd with the size of ligaments below 10 nm [56]. Whereas, a strain of ~ 1.3% was found for np Au-Pt with ligaments size ~ 5 nm [52]. Moreover, smaller strains of ~ 0.06% and 0.24% have been revealed for bare NPG with ligaments size of ~ 40 nm [21] and ~ 20 nm [51], respectively.

To this end, one would be led to a question: Is there any solution to improve the actuation performance of NPG?

Stacked NPG layers have been reported to own a giant strain of ~ 6% [80]. During a charging process, the layered np structures expand and gain a typical ~ 0.1% strain as measured in conventional NPG. However, the layers also connect together at discrete pinning sites. The layer part between two pinning sites will deflects and contribute to a giant expansion. Even though such a large strain, the brittle nature makes it impossible to achieve a big rolling deformation.

Very recently, it has been reported that the actuation amplitude of NPG is sig-

nificantly improved with a covering of MnO_2 layers [53] and the amplitude depends on the thickness of MnO_2 layers. Moreover, the expansion induced by intercalation of Na^+ into MnO_2 at the reduction process is also found, indicating the sign-inverted actuation-potential response in contrast to nanoporous gold. Yet, instead of the surface of Au ligaments, MnO_2 layers are directly deposited on the surface of the NPG samples so that the exposed MnO_2 in the electrolyte is still limited.

The improvement of NPG actuation performance has also been realized by constructing a composite by depositing a conducting polymer film on NPG skeleton.

A NPG/PANI(polyaniline) hybrid actuator has been studied [81]. It shows a strain of ~ 0.15% at a high scan rate of 10 mV/s, whereas the dimensional change of a np metal/electrolyte hybrid actuator is negligibly small at the same scan rate. In the NPG/PANI actuator, the gold ligaments are enveloped by polymer films so that the severe coarsening of gold ligaments during long term electrochemical processes in electrolyte [67, 82, 83] will be avoided. It is meaningful since the actuation behavior of np metal is closely related to the surface stress which will be greatly reduced in coarsened ligaments [84]. Even so, the NPG/PANI strip is not perfectly flat and the curved strip also 'vibrates' and the actuation behavior will be hampered.

Recently, mm-sized NPG/PPy hybrid electroactuators have been studied [29, 30]. The actuation amplitude of NPG has been greatly improved by PPy films. Notably, NPG/PPy with a PPy layer of 80 nm shows a 12-fold increase of strain compared to bare NPG [29]. Although the actuation properties are studied in an aqueous electrolyte environment, PPy films keep Au ligament from being coarsened. Moreover, the nature of high strength and stiffness of NPG provides a good opportunity for the hybrid material as a robust actuator to bear the load. Yet, the actuation mechanisms of a np metal and PPy film are different, understanding the actuation of PPy is the prerequisite to learn the actuation behavior of NPG/PPy hybrid electroactuators.

1.1.3 Conducting polymers

Since the discovery of the high conductivity in a halogen doped polyacetylene in the pioneering work by Shirakawa, Heeger, and MacDiarmid in 1977 [85], conducting polymers (CPs) with conjugated carbon-carbon double bond structure have drawn extensive attention from academic and industrial fields. Over the past several decades, CPs have been found applications in various fields, to name a few, anti-corrosion coatings, sensors, supercapacitors, catalysts, drug delivery, and actuators [2, 14, 86–89].

CPs are mainly synthesized via chemical or electrochemical polymerization. In chemical polymerization, the polymer chains are formed by oxidizing monomers in an electrolyte containing chemical oxidants. In electrochemical polymerization, the chain growth is initiated by an applied potential [29, 87, 90]. Generally, electrochemical polymerization is preferred since it allows the precise control of polymerization charge and the film thickness in contrast to the chemical polymerization. During the electropolymerization process, CP films are deposited on a conductive electrode surface via anodic oxidation of the corresponding monomers in the electropolymerization electrolyte. The electropolymerization is usually performed by various electrochemical techniques, such as potentiostatic method (application of a constant potential), galvanostatic method (application of a constant current), and potentiodynamic method (cyclic voltammetry: Continuous variation of the potential) [2, 29, 91]. In the galvanostatic method, the potential will increases and the CPs might be over-oxidized at a high potential. This will

be avoided at the constant potential applied in the potentiostatic method. Moreover, the CPs obtained in the potentiostatic method are in a doped state and own a high conductivity, while those produced in the potentiodynamic method are usually under an undoped state and are less conductive.

Recently, the pulse potentiostatic method (section 3.2.1.2) and pulse galvanostatic method have been developed [92–94]. During a typical pulse cycle, a potential (current) is applied for a relatively short time, during which monomers are oxidized and the generated CPs are deposited on the electrode surface; the potential (current) is then switched off for a relatively long time, during which the reactants can be sufficiently replenished on the electrode surface from the bulk electrolyte by diffusion. The relatively long replenishing time is specifically important for one to synthesize homogeneous films on a porous electrode [30, 93]. It has been found that the PPy films obtained by the pulse galvanostatic method have low defect density, high doping level, and good electrochemical reversibility [94]. Although the electropolymerization time is relatively short in a pulse cycle, the corresponding oxidation potential at the pulse peak current might be still too high and might over-oxidize the PPy film. The PPy films fabricated by the pulse potentiostatic method have better electrical conductivity and are at an excellent molecular anisotropy level as compared to those synthesized under constant potential conditions [95]. Besides, due to an increase in the number of new nucleation sites under the electrical pulse stimulation, PPy films with a smoother surface can also be obtained [92, 95]. Moreover, PPy films produced under the pulse potentiostatic method exhibit higher capacitance and electrochemical stability [92, 93].

Among the huge number of CPs, polyaniline (PANI), polythiophene (PT), and polypyrrole (PPy) are most commonly studied (PEDOT)[96, 97]. They all have high specific capacitance, electroactivity, and conductivity (doped state), and easy processability. However, a protic solvent or protic ionic is required to provide a proton to fully charge PANI [98], this will limit the application as actuators. Besides, it has been reported that during charging-discharging processes the mechanical property of PANI is impaired due to the irreversible structure change and mechanical degradation [99]. A PT based molecular actuator exhibits a high actuation of ~ 20% [100], however, the stability of PT has been reported to be poor in the air [101]. PPy has been extensively studied because of its good environmental stability, facile fabrication, relatively higher conductivity, outstanding redox properties, and high actuation [3, 102].

1.1.4 Electrochemically driven conducting polymer actuators

As has been addressed in the above section, PPy is considered the most attractive conducting polymer as an electroactuator. PPy converts electric stimulation to mechanical deformation by the opening (and folding) of the polymer chains as well as the diffusion of ions and solvent molecules entering (and exiting) the polymer matrix (section 2.5).

The actuation behavior of PPy has been extensively studied.

The actuation performance is intrinsically determined by the PPy film as well as the interaction between PPy and the testing environment. A diversity PPy will be formed at various synthesis conditions (e.g., electropolymerization potential, temperature, as well as the type of solvent and dopant). For instance, when a benzenesulfonate anions doped PPy strip was actuated in an acetonitrile solvent containing 0.01 M sodium benzenesulfonate, a strain of ~ 1% was obtained [103]. A work comprehensively studied the actuation of PPy doped with various anions (tetrafluoroborate, hexafluorophos-

phate, trifluoromethanesulfonate, and perchlorate anions in methyl benzoate solvent) [104] and found a strain of ~ 12% for all PPy films examined in the same aqueous sodium hexafluorophosphate solution. Whereas, the PPy film doped with perchlorate anions (in propylene carbonate solvent) showed a smaller strain of ~ 8% [104]. Besides, a PPy prepared from a methyl benzoate solution of 1,2-dimethyl-3-propylimidazolium tris(trifluoromethylsulfonyl)methide exhibited a high strain of ~ 37% in a propylene carbonate/water solution of lithium bis(nonafluorobutylsulfonyl)imide [3].

The actuation has also been studied based on PPy composites actuators. For example, PPy can be deposited on silk [105]. It has been found that if the ratio of pyrrole/$FeCl_3$ in the chemical polymerization solution was 1:1, a porous PPy film was synthesized and a strain of ~ 0.33% was obtained. However, when the ratio was 3:1, a smaller strain of ~ 0.05% was obtained. Besides, PPy can be coupled with carbon nanotube (CNT) and deoxyribonucleic acid (DNA) molecules, forming a DNA/CNT/PPy composite [106]. A strain of ~ 5% was found even at a high scan rate (10 mV/s). Moreover, this composite explores the possibility of the application of PPy in biological systems.

Since the diversity of the synthesis and the testing conditions, it is not easy to compare the actuation performance of PPy. However, scan rate, potential window, and PPy thickness affect the actuation behavior in an easier way. As reported in Refs. [14, 30, 107, 108], larger deformations have been detected on PPy electroactuator with a bigger thickness, in a larger potential window, and at a smaller scan rate. This is related to the number of incorporated ions. A thicker PPy film has more space to accommodate more ions and therefore, a larger strain is expected. A larger potential window is related to a more transferred charge, which will be balanced by the ions entering (or exiting). It should be noted that if the potential is too big, there is a risk of the degradation of PPy [109]. When scanning at a smaller scan rate, at which more ions are incorporated (or expelled) in a bigger time interval and larger actuation strain can be obtained.

In practical applications, a good electroactuator should still work well under load. However, many works have found that the actuation amplitude decreases with the load [14, 32, 33, 37, 103, 110–114]. In order to improve the ability of PPy to work against the load, a stiff material can be coupled with PPy to form a composite. Recently, PPy films have been reinforced by hybridizing a NPG substrate [29, 30]. The ligaments network in NPG work as both reinforcing framework for PPy coating and conductive substrate to ensure a high conductivity in the hybrids even when PPy is reduced to a neutral state. It has been found that both the strength and stiffness of NPG/PPy composite are enhanced in contrast to the individual component.

1.1.5 Electrochemically modulated stiffness

In addition to the macroscopic dimensional change, the electroactuator's modulus has also been found to change at different oxidation states, and the changes in modulus play an important role in the actuation performance [9, 14, 21, 31–38].

For instance, a reversible effective modulus variation (~ 10%) of NPG has been found upon cyclically monitoring the surface condition via tuning the applied potential. When Au ligaments surfaces are covered by oxygen species or under a condition of excess electrons, the stiffness of NPG will increase. Whereas when oxygen species are removed or the electrons are depleted, the stiffness of NPG decreases [21]. When

working under a load, the contributions of modulus variation and surface stress to the total strain of a NPG actuator have been distinguished [31]. Moreover, for the capacitive process, the strain is invariant with the load, whereas the actuator moves backward under a substantial load in the potential regime of oxygen electrosorption.

As far as the PPy actuator is concerned, the modulus responses to electrochemical charging-discharging processes are more complicated, and an agreement on the relationship between modulus and the applied potential is not reached so far. For example, Young's modulus of perchlorate anions doped PPy increases under oxidation in $LiClO_4$ aqueous electrolyte [32]. However, the Young's modulus of hexafluorophosphate anions doped PPy films decreases when electro-oxidized in $NaPF_6$ aqueous electrolyte [37] and in anhydrous propylene carbonate solvent containing tetrabutylammonium hexafluorophosphate [33]. Moreover, the absolute Young's modulus values vary between 0.2 and 1 GPa [32, 33, 37]. Therefore, it is only possible to analyze the effect of modulus change on the total actuation of a specific PPy during electrochemical redox under loads.

Taking the merits of the high strength and stiffness of NPG as well as the great actuation property of PPy, NPG/PPy hybrid electroactuators are promising actuators. As accounted above, the modulus changes are observed on both NPG and PPy, therefore, elastic Young's modulus variation of NPG/PPy hybrid electroactuators under electrochemical conditions is expected. Yet, the corresponding studies are not available. This thesis will inspect the Young's modulus behavior of NPG/PPy electroactuators during electrochemical redox processes and the underlying mechanism of the modulus change.

1.2 Outline of the thesis

The present thesis studies the Young's modulus behavior and actuation under load of NPG/PPy hybrid electroactuators using *in situ* dynamic mechanical analysis under electrochemical control. NPG specimens are fabricated by electrochemical dealloying method and the PPy coatings are electropolymerized on NPG. The dealloying and electropolymerization mechanisms will be introduced in Chapter 2. Chapter 2 also reviews the conducting mechanism of PPy, the redox reactions in PPy, and the actuation mechanisms of NPG and NPG/PPy. Moreover, Larché-Cahn theory, which is accounted for the relationship between composition and mechanical behavior, is briefly reviewed in Chapter 2.

Chapter 3 introduces the experimental details, including the electrochemical setups, electrochemical techniques, NPG/PPy preparation, microstructure characterization methods, and *in situ* electro-chemo-mechanical testing approaches.

Chapter 4 presents the results of this thesis. First of all, the microstructure and electrochemical properties of NPG are discussed, and the surface area of NPG specimens is determined, which is crucial for assessing PPy film thickness. Also, the linear scan and staircase voltammogram as methods to modulate the potential on NPG and NPG/PPy hybrids are compared. The staircase voltammetry has been found to underestimate the charge when a very small amount ($\sim 10^{-4}$ mm^3) of PPy is involved. However, it shows comparable performance with linear scan voltammetry when PPy increases to $\sim 10^{-2}$ mm^3. Thereupon, the microstructure and electrochemical properties of NPG/PPy hybrids are presented. PPy film thickness has been found to be proportional to the electropolymerization charge density and the capacitance of NPG/PPy hybrids shows a linear dependence on PPy thickness. Analysis of the mechanical

properties of NPG/PPy begins with load-unload results, which provide strength and Young's modulus of NPG/PPy hybrids. Then, the *in situ* DMA measurements reveal the most striking non-linear effective Young's modulus versus electrode potential. Effects of PPy thickness, oxidation states, and H_2O, have been explored to study the underlying mechanism of this phenomenon. In the final section, the actuation under load has been investigated under cyclic voltammetry. The total actuation strain is found unvaried under all applied loads. The contribution of Young's modulus variation to the total strain has been analyzed.

Chapter 5 discusses the microstructure, electrochemical behavior, and mechanical behavior of NPG and NPG/PPy with specific emphasis on the electrochemically modulated non-monotonous Young's modulus behavior of NPG/PPy hybrids and the possible mechanism behind the phenomena. The contribution of Young's modulus variation under various loads to total actuation strain is also discussed.

Chapter 6 summarizes the main findings in the present thesis and proposes an outlook on future work.

Chapter 2

Theoretical background

2.1 Nanoporous structure formation during dealloying

Different dealloying techniques have been used to produce nanoporous (np) metals, such as liquid metal dealloying [116], vapor phase dealloying [117], free corrosion [66], and electrochemical dealloying [83, 118–120]. In this work, we focus on the electrochemical dealloying of Au-Ag master alloy. Below, the microstructure evolution related to this technique is briefly discussed.

During the dealloying process, less noble atoms (e.g., Ag in Au-Ag alloy) are selectively dissolved. A minimum fraction (the parting limit or dealloying threshold) of the less noble species is required to produce large enough space for the penetration of the electrolyte as well as for the dissolved atoms. If the amount of the less noble component is less than the parting limit, the enrichment of more noble atoms at the metal-electrolyte interface will hinder the further corrosion process and pits are only formed at the outermost layers [121]. In the case of Au-Ag alloys, the parting limit is usually between 50 and 60 at.% [122].

Another key parameter in dealloying is the critical potential, E_C, which defines the onset of the percolation dissolution characterized by a significant rise in current above E_C [65, 121, 123]. Below E_C, the corrosion-induced rough surface will be passivated by the more noble metal atoms, resulting in a low current [124]. Above E_C, the less noble (Ag) atoms on the topmost layer are dissolved and removed easily, leading to the creation of terrace vacancies. The Ag atoms that are laterally coordinated to the vacancies have fewer bonds and therefore they are more easily to be dissolved compared to those in the bulk alloy and the dealloying front spreads laterally (Figure 2.1a) [64, 125]. The undissolved noble atoms (Au), instead of remaining as thermodynamically unfavorable adatoms, diffuse along with the metal-electrolyte interface to agglomerate into clusters. As the dealloying proceeds, the Au-rich mounds develop and grow in diameter as depicted in Figure 2.1b. As the dissolution continues, the released Au atoms are not sufficient to passivate the surface, and the undercutting and bifurcation of the ligaments take place (Figures 2.1c and d). At this stage, the alloy has been primarily dissolved. As shown in Figure 2.1e, the primary dealloying produces nm-scaled ligaments (2 ~ 7 nm [41, 83, 126, 127]) with a high amount of the residual silver (~ 50 - 60 at.%[83, 128]). Further exposure at dealloying conditions leads to the curvature-driven coarsening, as illustrated in Figure 2.1f.

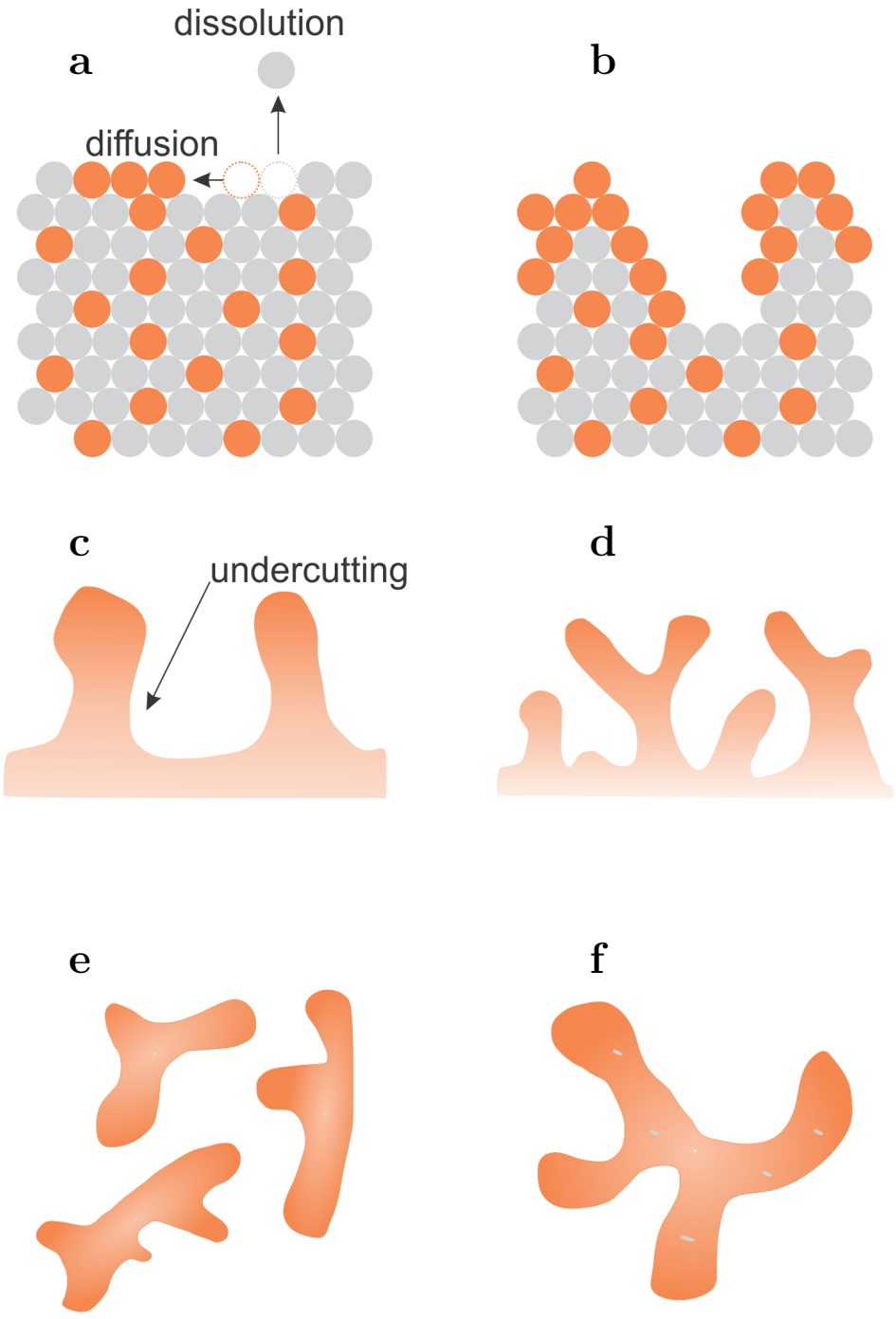

Figure 2.1. (a) Dissolution of the less noble Ag atoms (gray) and the agglomeration of the more noble Au atoms (orange). (b) Formation of the mounds passivated by Au atoms. (c, d) Undercutting and the bifurcation of the ligaments because of the insufficient Au to passivate the mounds. (e) Formation of bicontinuous porous structure with Au-rich outer surfaces and Ag-rich interiors. (f) Coarsening in electrolyte leads to the growth of the ligaments and the exposing of the residual Ag to the electrolyte for further dissolution. Redrawn according to Ref. [115].

After the primary dealloying, the ligament network still contains a significant amount of Ag which could be diminished upon a further dissolution, namely, secondary dealloying. During the secondary dealloying process, the curvature-induced surface diffusion will result in the diffusion of surface Au atoms. The silver clusters in the ligaments formed during the primary dealloying are exposed to electrolyte and are further dissolved, leading to a significant reduction of the silver fraction in the final dealloyed specimen with residual Ag < 2 at.% [42, 128]. It should also be noted that the residual Ag after the secondary dealloying also exists in the form of a cluster inside the ligaments, whereas an annealing treatment can produce a uniform distribution of Ag throughout the ligaments [128, 129].

Meanwhile, the Au atoms at the surfaces of several-nm-scaled ligaments are thermodynamically metastable and are sufficiently mobile with a diffusion coefficient, D_s ($\sim 2 \times 10^{-19}$ cm^2/s [82, 126] ar room temperature), at the metal-electrolyte interface. Over the dealloying course, the rearrangement of Au atoms driven by surface diffusion will lead to the growing of ligaments from several to tens of nanometer [67, 82, 83]. Moreover, thermal annealing is another powerful process to increase the size of the ligaments. At an elevated temperature, the coarsening activation energy of NPG in the air is ~ 1/3 - 1/2 of that in vacuum [130, 131], and the adsorption of oxygen molecules promotes the diffusion of Au atoms [131]. Under elaborated tailoring of annealing temperature and time, NPG ligaments with mean size from several tens to several hundreds of nanometer can be obtained [26, 29, 130].

2.2 Polymerization of conducting polymer polypyrrole

2.2.1 Electropolymerization mechanism of polypyrrole

The mechanisms involved in the electropolymerization were discussed in Refs. [132, 133]. However, a conclusive mechanism has not been established so far. The most commonly referred mechanism [134] will be introduced below.

The first step in the electropolymerization is the oxidation of pyrrole monomers at the working electrode surface and the formation of the cation radicals (1 in Figure 2.2a). Instead of the nitrogen atom, the unpaired electrons localize on the carbon atoms in the ring. Because the positions (α or β position) of the carbon atoms on the ring are different, cation radicals exist in several structures as shown in Figure 2.2a1. Normally, a higher electron density is found at the α-position, therefore, the resonance form (3) is more likely to be generated than forms (2) and (4). Afterwards, the dimerization takes place as shown in Figure 2.2b. The coupling of the two radicals leads to the formation of a bond between their α-positions, and a dihydromer dication (5) forms with two hydrogen atoms bonding on the α-position carbons. In this process, the repulsion between the cation radicals is overcome by other species, such as solvent, the counteranion, and even monomers [135].

In the next step, the hydrogen atoms are removed (deprotonation), resulting in the formation of a neutral dimer (6), as shown in Figure 2.2c. The dimer has two rings and the electrons delocalize in this bigger system, and the dimer can be oxidized even easier than the monomer. The dimer is further oxidized into dimer cation radical (7), as depicted in Figure 2.2d. The dimer radical in form of (7) has the most reactive region

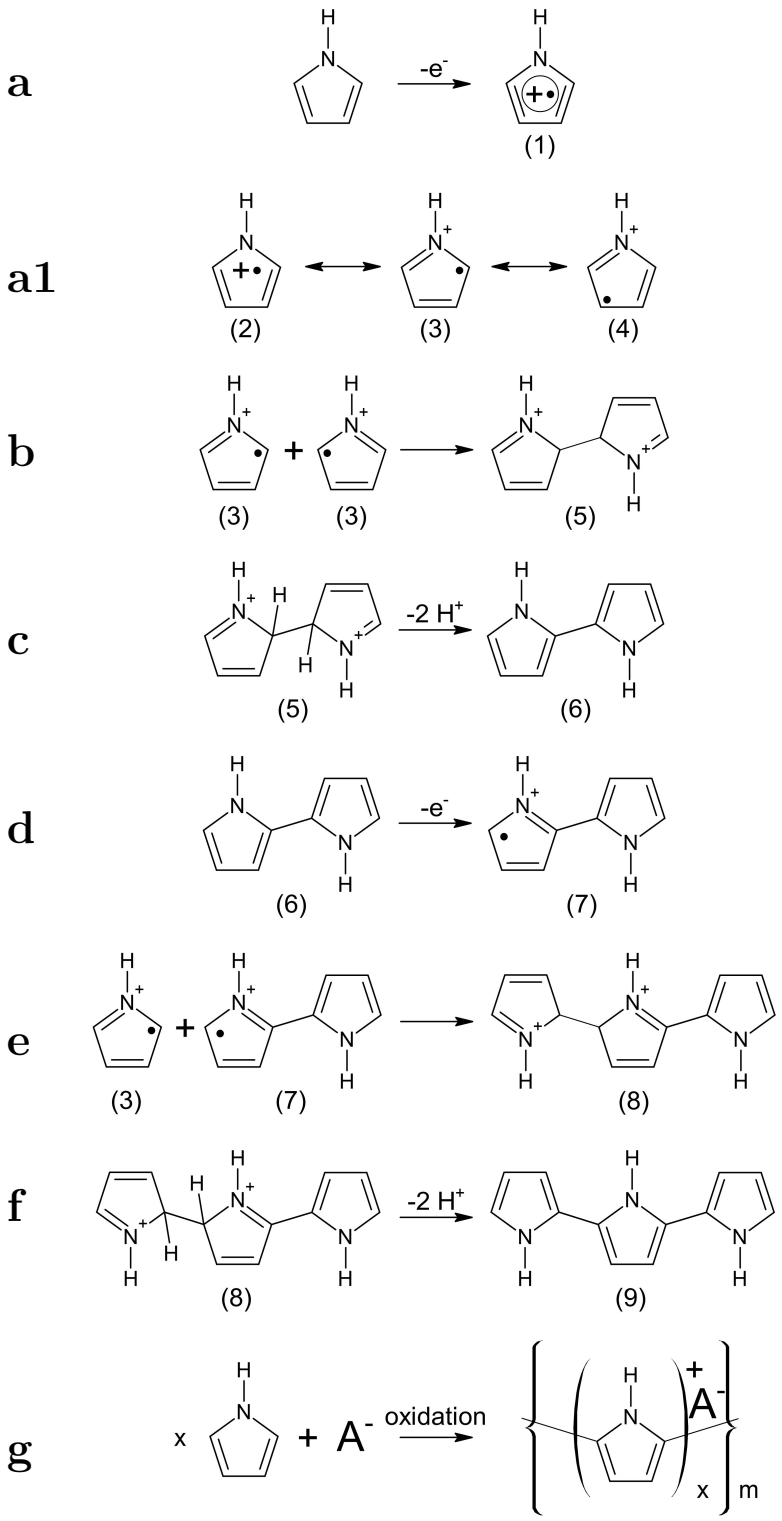

Figure 2.2. (a) Oxidation of a pyrrole monomer forms pyrrole cation radicals (1). (a1) Resonance forms of the pyrrole cation radicals (2-4). (b) The coupling between two cation radicals (3) forms a dihydromer dication (5). (c) Deprotonation of the dihydromer dication (5) forms a dimer (6). (d) Oxidation of the dimer (6) forms cation radicals (7). (e) The coupling between a cation radical (3) and a cation radical (7) forms a trimer dication (8). (f) Deprotonation of the trimer dication (8) forms a trimer (9). (g) Simplified polymerization reaction with the counteranion (A^-) incorporated to neutralize the positive charge on the polymer chain. Every 3 or 4 pyrrole units (x =3 or 4) carry one positive charge, indicating 0.25 ~ 0.33 cation centers per pyrrole unit, namely, the doping level of 0.25 ~ 0.33. The subscript m denotes the polymer chain length. Redrawn according to Ref. [132].

at α-position and is dominant in contrast to other forms. Subsequently, as shown in Figure 2.2e, the monomer radical (3) reacts with the dimer radical (7) and forms a trimer dication (8), again, with two hydrogen atoms on the α-position carbons. After the deprotonation (Figure 2.2f), a neutral trimer is formed. As the reaction proceeds, the processes of oxidation, coupling, and deprotonation repeat, and the polymer chain is extended. When the polymer oligomers exceed a critical length, the solubility limit of the oligomers is reached and the polymer precipitates on the electrode surface [136, 137].

Ideally, the polymer chain grows linearly in form of α-coupling. A model representing the ideal arrangement of the chains of an undoped PPy has been proposed [138], as shown in Figure 2.3. In this model, chains lay in a two-dimension (a, b) plane with a = 8.2 Å, b = 7.35 Å, and an angle between a and b around 65°. The layers stack in the third dimension with the interlayer spacing c =3.41 Å. However, when the polymer chain is getting longer, carbons at β-position have an opportunity to own higher electron density and therefore leading to the β-coupling in the polymer chains [139]. Moreover, the electropolymerization simultaneously takes place at different sites on the conductive substrate and the chains with various lengths will inter-twine with each other, resulting in the formation of chain networks [140].

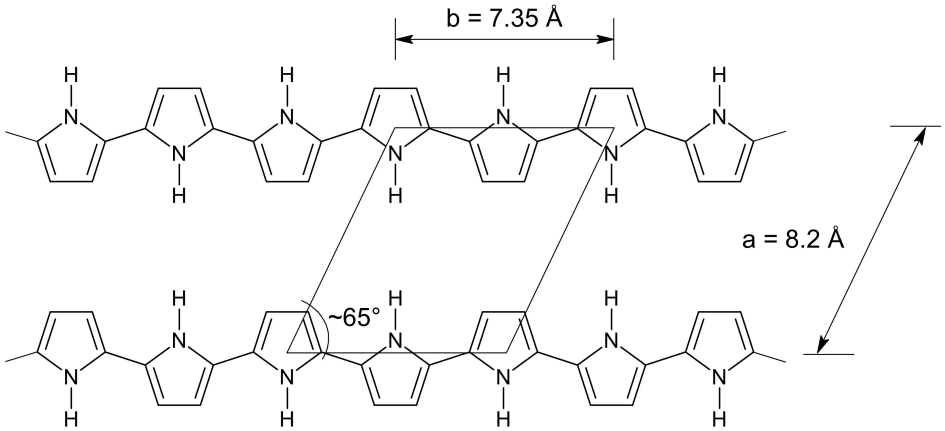

Figure 2.3. Ideal chains arrangement in (a, b) plane of an undoped PPy. Chains lay in (a, b) plane with a = 8.2 Å, b = 7.35 Å, and an angle between a and b around 65°. Redrawn according to Ref. [138].

It should be noted that during the electropolymerization every 3 or 4 pyrrole units carry one positive charge which is counter-balanced by an anion (ClO_4^- in this work). In this way, doped PPy is synthesized with 0.25 ~ 0.33 cation centers per pyrrole unit, namely, the doping level of 0.25 ~ 0.33. The overall polymerization steps are summarized in Figure 2.2g.

2.2.2 Factors affecting electropolymerization

According to the polymerization mechanism mentioned above, various factors can affect the PPy formation process, to name a few, the electrode, electrolyte, and solvent. The impact of these factors on the synthesis of PPy is described below.

2.2.2.1 Effect of electrode material

PPy films have been synthesized using inactive electrodes, for example, Pt, Au, or glassy carbon [2, 141, 142]. The active metals, such as Ti and stainless steel, however, will be oxidized at the potential of the pyrrole oxidation. The formation of the oxide films can interfere with the electropolymerization behavior. The charge transfer can be affected by the oxide films and the polymerization current density will be inhibited [143]. In organic solvent, the trace water and oxygen in the solvent can lead to the formation of oxide films.

Another factor that should be considered is the adhesion of the polymer film to the electrode surface. If a free-standing PPy film is desired, PPy films should be peeled off easily. However, in the fields of anti-corrosion protection and actuator materials, the detachment of the films from the electrode surface should be inhibited. In contrast to the simple PPy-metal bi-layer structure, the bi-layer constructed by a 'U'-shape PPy layer covering on both the top and two side edges of the metal substrate exhibits a better ability to against delamination [144]. In this respect, NPG will be a more proper substrate candidate since PPy film fully envelops the ligaments network and the delamination will be diminished. Recently, nanoporous metals have been used as electrodes (or templates) for PPy deposition. As a result, the specific capacitance and actuation properties of the NPG have been greatly improved [29, 30, 87, 145, 146].

2.2.2.2 Effect of solvent

The solvent for electropolymerization should be carefully chosen since diverse PPy with various structures and properties can be formed in different solvents. The solvent should meet the requirements of a high dielectric constant which ensures the ionic conductivity and electrochemical resistance against the decomposition at the monomer oxidation potential. Besides, nucleophilic reactions (the reactions of the electron-rich nucleophile (H_2O or OH^-) with electron-deficient acceptors (usually carbon)[147, 148]) should be minimized.

PPy can be prepared in aqueous electrolytes. PPy with high conductivity (500 S cm^{-1}) can be obtained in an aqueous solvent containing *p*-toluenesulfonate [113]. However, the cation radical intermediates (structures 2-4 and 7 in Figure 2.2) would react with the nucleophilic solvent (herein H_2O), resulting in the formation of carboxyl groups which inhibit the further growth of polymer chains [149]. In most cases, PPy is prepared in aprotic organic solvents. Acetonitrile (ACN) is most commonly used because the nucleophilic attack during the electropolymerization can be inhibited [150]. In addition, PPy prepared in ACN solvent is denser than that prepared in H_2O solution [151]. It should be noted that an addition of a small amount (1%) of water to ACN improves the properties of PPy, especially the conductivity and mechanical (tensile strength and Young's modulus) properties [152]. This improvement might be due to water, a fairly strong base in ACN, will capture the released protons (Figures 2.2c and f) during the electropolymerization process, preventing the acid-catalyzed formation of trimer and avoiding the subsequent electrode passivation [153]. In some cases, 2 vol.% water was added to ACN [154].

2.2.2.3 Effect of electrolyte

When choosing an electrolyte, the solubility of the salt and the nucleophilicity of the anion should be specially considered. Besides, the oxidation potential of an anion should be higher than that of a monomer. During polymerization, the anions are incorporated into the film as dopants. The dopants can be inorganic or organic salts with various sizes [147]. A small dopant facilitates the incorporation process and improves the polymerization efficiency. It is reported that polypyrrole (fabricated in an aqueous solution) doped with large amphiphilic sulfonate dopant exhibits better conductivity, stability, and mechanical properties than the PPy doped with small sulfate anions [155]. However, during redox reactions, large dopants are immobilized in the polymer matrix and polymer performance will be affected [156].

The concentration of the electrolyte is also important for the formation of PPy. Proper increase of the electrolyte concentration can improve the properties of PPy films. For instance, the conductivity and strength of the nitrate-doped PPy increased by 50% when electrolyte concentration increased from 0.2 to 1 M. Yet, a further increase of the concentration does not help to improve the PPy performance [157]. A similar phenomenon was also observed in *i*-butylammonium *p*-toluenesulfonate-doped PPy film when the anion concentration increased to 0.3 M [158].

In addition to the electrode materials, solvent and electrolyte, other factors can also affect the synthesis of PPy, such as pH and temperature [159, 160]. Also, the diverse combinations of a polymerization technique (potentiostatic or galvanostatic), temperature (room temperature or lower), solvent (aqueous or organic), the concentration of electrolyte, and the amount of water that added to the solvent make the PPy synthesis more complicated.

2.3 Conducting mechanism of polypyrrole

As shown in Figure 2.2, pyrrole units form ideal PPy chains by α-coupling, resulting in a conjugated structure with alternating single and double bonds along the polymer backbone. The single bond includes a localized σ-bond. The electrons in this bond are localized between two atoms. In addition to the σ-bond, the double bond also contains a π-bond. The electrons in the π bond are not fixed and can move along the carbon backbone [161]. Therefore, the conjugated structure allows the electric flow. However, the conjugated bonds do not make PPy highly conductive. A neutral (undoped) CP, in fact, belongs to a semiconductor or even an insulator, whereas upon doping the electronic state of the CP can change to metallic.

During redox processes, in which dopants are involved, charges are transferred and charge carriers are introduced along the backbone [162]. However, it should be noted that the doping mechanism in a CP is different from that of a semiconductor. During doping, electrons are extracted from the highest occupied molecular orbital (HOMO) of the valence band (oxidation) and moved to the lowest unoccupied molecular orbital (LUMO) of the conduction band (reduction). During this oxidation-reduction process, charge carriers are created and they exist in the form of polarons (radical ions, Figure 2.4f) and bipolarons (dications or dianions, Figure 2.4g). The movement of the charge carriers along polymer chains produces conductivity. From the aspect of solid-state physics, the oxidation and reduction respectively correspond to *p*-type and *n*-type doping. With the reference to the *p*-type doping, electrons directly move from

HOMO to the dopant, creating a hole on the polymer chain. On the contrary, in *n*-type doping, electrons move from the dopant to LUMO, which results in the increased electron density.

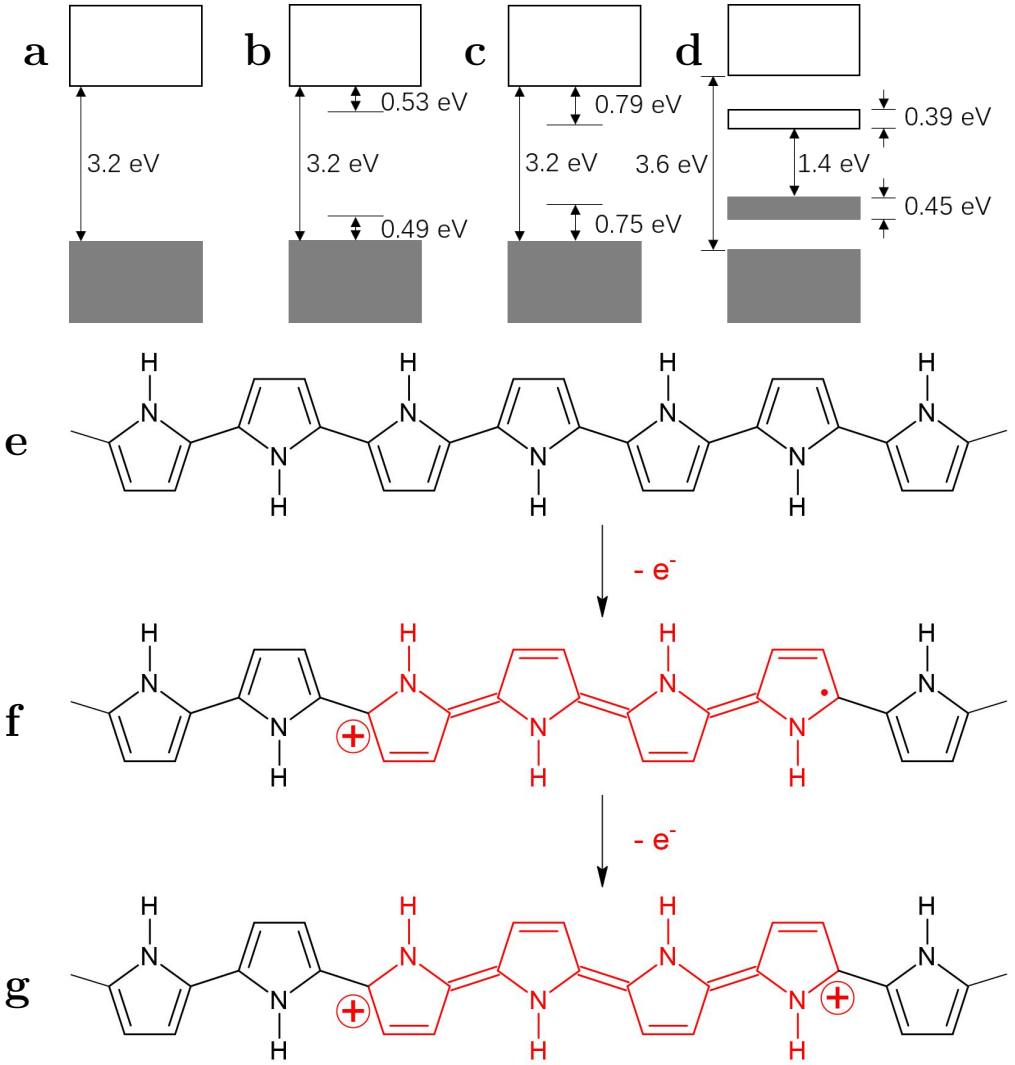

Figure 2.4. Band structures of PPy in the undoped state (a), a low doping level, the formation of polaron (b), a moderate doping level, the formation of bipolarons (c), and a high doping level (~ 33%), overlapping of bipolarons and formation of new small bands (d). Band colors in (a) - (d): gray corresponds to the valance band and white corresponds to the conduction band. Chemical structures with red color illustrate (quinoid) polaron (f) and bipolarons (g) upon the oxidation of the undoped (benzenoid) PPy (e). Redrawn according to Refs. [162, 163].

PPy is a typical *p*-type semiconductor [161]. In an undoped state (Figures 2.4a and e), PPy is an insulator with a large band gap (3.2 eV [163]). When PPy is oxidized, an electron is removed from the PPy backbone and a radical (polaron) is produced [163]. This results in two localized electronic levels (~ 0.5 eV from the band edges, Figure 2.4b) in the band gap with the lower energy state being occupied by one unpaired electron. Upon further oxidation, bipolarons are formed by removing the second electron from PPy chain. In this case, the polarons are replaced by bipolarons and electronic levels are ~ 0.75 eV (Figure 2.4c) away from the band edges. As the oxidation proceeds, the bipolarons overlap, resulting in two new narrow bands with a much smaller gap of

1.4 eV (Figure 2.4d).

2.4 Redox reactions in polypyrrole

As described in section 2.3, doping induces the formation of charge carriers (polarons and bipolarons) as well as backbone transformation (from undoped benzenoid structure to quinoid structure) in CPs. By undoping the polymer, the original structures are recovered. The reversible doping-undoping corresponds to charging-discharging processes. For PPy as the *p*-type polymer, upon electrochemical oxidation, the electrons in π-bond are extracted and move along the backbone. Meanwhile, in order to maintain the electric neutrality, the counteranions are incorporated into PPy from the bulk electrolyte [162]. Upon electrochemical reduction, the counteranions are expelled out of PPy. The doping-undoping of PPy is schematically shown in Figure 2.5, where A^- is the counteranion.

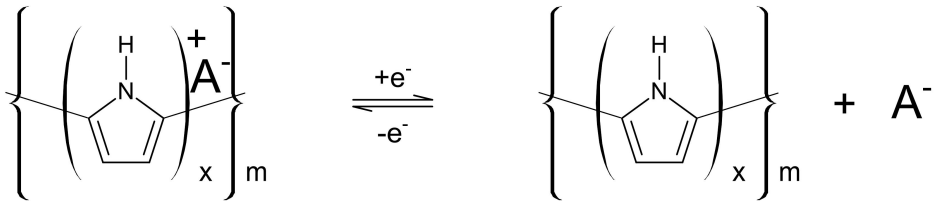

Figure 2.5. Doping-undoping of during electrochemical oxidation-reduction of PPy in the electrolyte containing A^- species (A^- is ClO_4^- in this work). Subscripts x and m are defined in Figure 2.2.

Cyclic voltammetry (CV) is the most powerful technique to characterize the redox reactions in PPy [87, 164–166]. Generally, two types of voltammograms are recorded: A quasi-rectangular CV curve without redox peaks and a CV curve with redox peaks [142, 167]. Typically, the rectangular profile of CV is the characteristic of the double layer charging (Figures 2.6a and b), in which ions from an electrolyte are reversibly adsorbed on the surface of an electrode, such as carbon-based materials and nanoporous metals [29, 43, 168–173]. However, rectangular or quasi-rectangular CV profiles are also observed in pseudo-supercapacitors, such as PPy [142, 172, 174–176]. The pseudo-supercapacitors store charges based on the Faradic mechanism. However, not in the same way as batteries, in which electrons transfer and metal centers are oxidized or reduced. Therefore, although the redox peaks are observed in Ref. [167], the conducting polymer behaves in a pseudo-capacitive way, as shown in Figures 2.6c and d. In addition, a linear dependency of current, j, on the scan rate, v, ($j \sim v$) also indicates the capacitor-type mechanism (double layer capacitive and surface-controlled Faradic redox pseudo-capacitive processes) [172, 174, 175, 177, 178], whereas the linear dependency of j on the square root of scan rate, $v^{1/2}$, ($j \sim v^{1/2}$) suggests the battery-type mechanism (diffusion-controlled Faradic redox process) [172, 174, 175, 178].

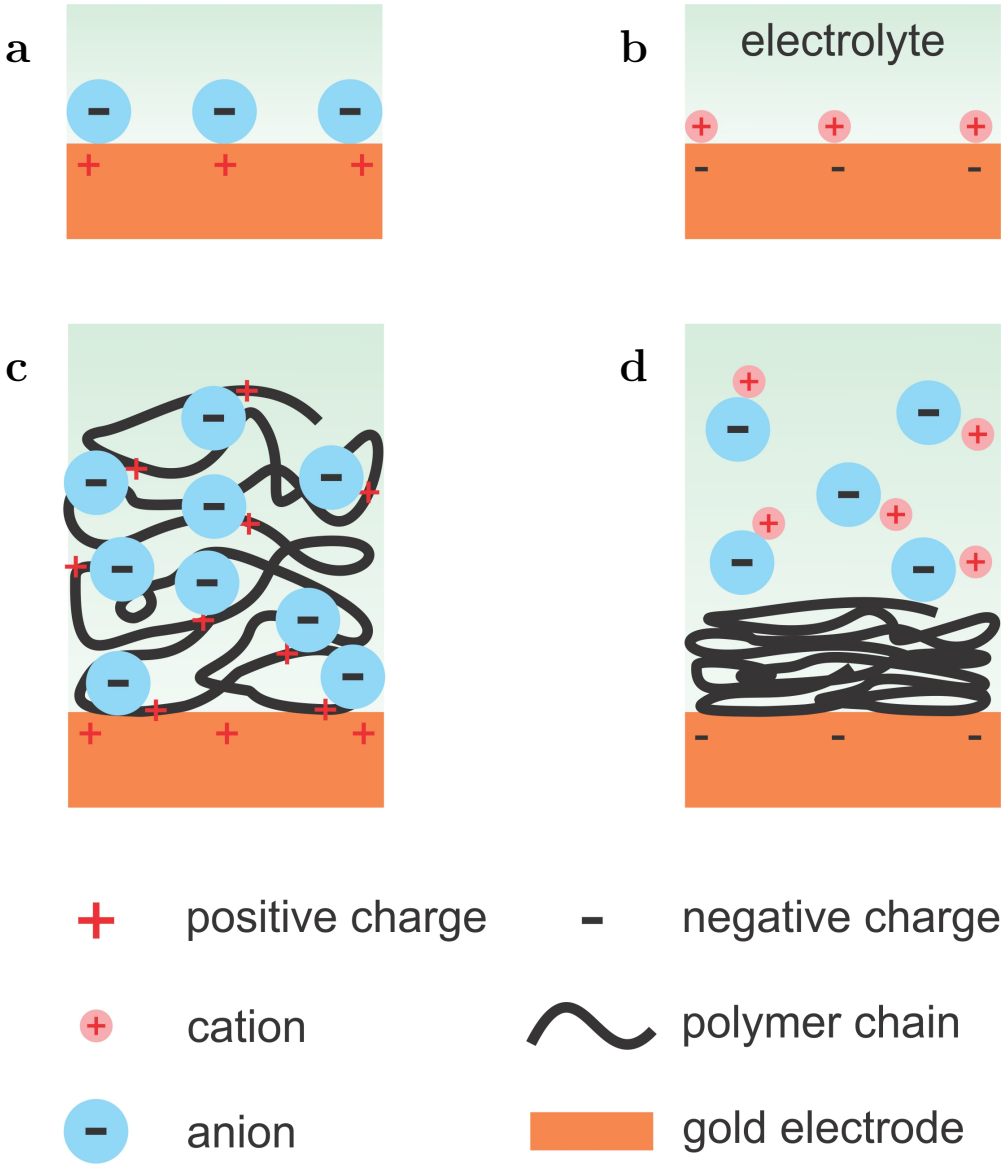

Figure 2.6. Simplified model showing capacitive charging (a) and discharging (b) at the Au/electrolyte interface, and pseudo-capacitive charging (c) and discharging (d) in Au/PPy electrodes, respectively. In (a) and (b), ions with opposite charges are electrostatically attracted to the Au surface. Anions (ClO_4^- in this work) are incorporated into PPy matrix upon oxidation, leading to PPy swelling (c), whereas anions are expelled out of PPy matrix upon reduction, resulting in PPy shrinkage (d). Ions exist in a form of hydrated ions [7, 179, 180]. Symbols conventions are denoted at the bottom of the figure. Redrawn according to Ref. [181].

2.5 Actuation mechanisms of NPG and PPy

2.5.1 Actuation mechanism of NPG

As described in section 2.4, by applying a potential to a metal immersed in an electrolyte, the ions with opposite charges will be electrostatically attracted to the metal surface, forming a double layer. The interfacial charge density on the metal will vary by sweeping the potential. The modified electronic density will change the bonding at the surface and, as a result, the local surface stress, f, by $\delta f = \zeta \delta q$ with $\zeta = \mathrm{d}f/\mathrm{d}q|_e$ the electrocapillary coupling parameter, e the tangential elastic area strain (relative change in the area), and q the surface-specific charge density. The change in the local stress will be compensated by the bulk stress, resulting in the overall macroscopic length change (actuation, ε) of the metal with a high specific surface area [49, 50, 52]. The strain obeys:

$$\delta\varepsilon = -\frac{2\alpha\theta}{9K}\delta f \tag{2.1}$$

where K is the bulk modulus of the nanoporous metal, α is the specific surface area, θ is the dimensionless parameter that relies on the microstructure and the Poisson's ratio, v.

Since charging of a nanoporous metal in electrolyte leads to its expansion or contraction, a strain-charge coefficient A^* can be used to study the relationship between charge and strain [39]:

$$A^* = \frac{\mathrm{d}\varepsilon}{\mathrm{d}q_\mathrm{V}} \tag{2.2}$$

where q_V is the volumetric charge density.

2.5.2 Actuation mechanism of PPy

The reversible oxidation and reduction of conducting polymers are associated with the dimensional changes of the polymer. As described in sections 2.3 and 2.4, upon oxidation, the electrons are withdrawn from the polymer chains, generating positive charges. The electric neutrality is maintained by incorporating counteranions (ClO_4^- in this work) into PPy matrix from surrounding electrolyte. The anions and polymer chains form ionic crosslinks, and the polymer chains will be stretched, resulting in the total volume increase (Figure 2.6c). Upon reduction, the anions are expelled, and the polymer chains are coiled, leading to the total volume shrinkage (Figure 2.6d) [2, 29, 182]. The anion-driven actuation (expansion-contraction) of the PPy matrix can be explained by an electrochemically stimulated conformational relation (ESCR) model [154, 181, 183, 184]. Upon oxidation, the polymer chains store positive charges and the electrostatic repulsion forces will push the chains to move away from each other, generating a *free volume* to accommodate the counteranions from the electrolyte. This process is called conformational relaxation. Upon further oxidation, anions are incorporated into the free volume. When the polymer is reduced, counteranions are expelled to the solution, leaving behind polymer chains with the free volume. This is a partial reduction with a little contraction. The chains are compacted and the free volume is closed at a further reduction state. It should be noted that during redox reactions in PPy matrix the counteranions are covered by a solvation shell [7, 179, 180].

In addition to the solvation shell, more solvent molecules are involved in the form of free water [7, 185–187]. During oxidation and reduction processes, the flux of counteranions will bring a concentration difference of counteranions between PPy matrix and the surrounding electrolyte, giving rise to osmotic pressure difference [185]. Especially in a low-concentrated electrolyte, the osmotic effect induces solvent molecules to move into or out of the polymer in a number (~ 10) more than that (~ 4) of those bound strongly in the solvation shell of the counteranions, contributing a considerable part to the total actuation [187].

Besides, it has been reported for a *p*-type PPy that the electron loss on polymer chain opens up the angle and at the same time elongates the bond length [188]. This effect has also been found in a carbon nanotube (CNT) electrochemical actuator, in which ions from electrolyte at the CNT-electrolyte interface (forming a double layer) compensate the potential induced electronic charge, and a strain up to 1% was observed within a 1 V operation range [74].

In addition to the microscopic rearrangement of polymer chains in PPy matrix, the changes in macroscopic Young's modulus in response to the variations of oxidation status have also been reported [14, 32, 33, 37, 103, 110–113]. Since the majority of the synthesis parameters (section 2.2.2) and the electrochemical testing environment, an agreement on the relationships between Young's modulus and the oxidation status has not been reached so far. Irrespective of that, the actuation strain is associated with Young's modulus.

The total actuation strain change, $\delta\varepsilon$, is composed of two parts [189]: 1) strain change induced by electrochemical redox, which is usually called 'free stroke', $\delta\varepsilon_0$; 2) the strain change caused by the changes in Young's modulus, which is related to the applied load. For a polymer actuator under tensile load, if an increase in the modulus is observed when PPy switches from the reduced to the oxidized state, a reduction in the strain is seen. The actuation strain is then described as follows:

When PPy solely works under a given load, σ, without an electrochemical stimulation, according to Hooke's law:

$$\varepsilon = \frac{\sigma}{Y} \tag{2.3}$$

where Y is the elastic modulus of the electroactuator.

When PPy solely works in the electrochemical environment under no load:

$$\delta\varepsilon = \delta\varepsilon_0 \tag{2.4}$$

Electrochemical redox processes will induce a variation of Young's modulus, and when PPy works under both load and electrochemical control:

$$\delta\varepsilon = \delta\varepsilon_0 + \delta\frac{\sigma}{Y} = \delta\varepsilon_0 + \sigma\delta\frac{1}{Y} \tag{2.5}$$

Since

$$\delta\frac{1}{Y} = -\frac{1}{Y^2}\delta Y \tag{2.6}$$

substituting Eq. 2.6 into Eq. 2.5, one gets:

$$\delta\varepsilon = \delta\varepsilon_0 - \frac{\sigma}{Y^2}\delta Y \tag{2.7}$$

Thus, the actuation strain of NPG/PPy hybrids upon electrochemical redox under a load, σ, is:

$$\delta\varepsilon = \delta\varepsilon_0 - \frac{\sigma}{Y'^2}\delta Y' \tag{2.8}$$

where Y' is the effective elastic modulus from a dynamic mechanical analyzer (DMA).

2.6 Larché-Cahn open-system elasticity

The theory of open-system elasticity by F. Larché and J.W. Cahn was proposed to describe chemo-mechanical coupling. Central to the theory is a concept of the open-system elastic constants. It allows one to predict the mechanical property of a crystalline material under stress when its composition alters [190]. In Larché-Cahn theory, a concept of *solid network* is proposed. The solid network announces the immobile sites in a solid and can be reversibly strained by the diffusion of mobile ions or stress. Gibb's "solid which absorbs fluid" is a good example. The solid does not diffuse but the network can be reversibly strained by the absorption of fluid. Moreover, Ref. [190] also points out that polymers absorbing solvent or counterions can be described by networks.

Below, the essential aspects of the theory are briefly described. In the thesis, it has been for the first time attempted to apply this approach to explain the experimentally detected reversible change of modulus of NPG/PPy hybrids in correspondence to the electrochemical oxidation and reduction of the polymer.

In a closed-system, under an equilibrium condition, all relative motions (e.g., diffusion) of the atoms in a purely elastic multi-component solid are proscribed. In other words, the local component is invariable and immobile under stress and deformation. At a given composition, the strain, ε, is caused by mechanical stress, σ, and Hooke's law gives the closed-system compliance coefficient, S, by:

$$\varepsilon = S\sigma \tag{2.9}$$

On the contrary, in an open-system, the restrictions are much less and the local component is variable and mobile under stress and deformation. The small component fluctuation will induce an additional strain, and therefore, the total strain, ε^*, of an open-system is the sum of the strain induced by component fluctuation and the strain induced by stress. The open-system compliance, S^*, is defined by:

$$\varepsilon^* = S^*\sigma \tag{2.10}$$

For a binary interstitial solid solution with a given composition, when stress is zero the material is under reference state, and the strain, solute fraction, and solute chemical potential are 0, x_0, and μ_0, respectively. When applying a uniaxial stress, σ, the strain, solute fraction, and solute chemical potential are in different conditions under closed-system and open-system (please refer to Figure 2.3 in Ref. [191]). And one can obtain the compliance coefficient difference between closed-system and open-system:

$$S^* - S = \chi\eta^2 \tag{2.11}$$

where η is the concentration-strain coefficient and χ is the solute susceptibility.

The theoretical relative compliance is then obtained:

$$\Delta s = \chi \eta^2 Y_0' \tag{2.12}$$

where Y_0' is the effective elastic modulus.

Recently, this theory has been experimentally verified by Shi and Weissmüller via studying the coupling between elasticity and hydrogen in bulk nanoporous (np) Pd-H and Pd-Au-H under dynamic stress [76]. Specifically, adjusting the charge density on the surface of np metals will induce a variation in the surface stress, which will be compensated by bulk stress and strain, resulting in the macroscopic actuation of np metals. In addition to solely modifying the surface charge density, one can also inject ions into the bulk lattice of the metal scaffold so that a higher strain amplitude can be achieved. Np Pd is an electroactuator that works according to the aforementioned mechanisms [56, 76]. When electrochemically charged in 1 M H_2SO_4 solution, a certain amount of hydrogen will be adsorbed on np Pd surface via hydrogen underpotential deposition (UPD) and the interior of the bulk via hydrogen insertion into the lattice. Under a uniaxial compressive load applied by DMA, the ligaments will be predominantly bent. The bending will introduce a stress gradient along the cross-section of a ligament. That is to say, one side of the ligament is on compression, whereas the other side is in tension. The stress gradient will drive a solute redistribution, i.e., from the compression region to the tension region. The theoretical open-system compliance variation, Δs_{th}, was predicted according to Eq. 2.12, and the experimental compliance variation, Δs_{exp}, was obtained from $Y'/Y_0' - 1$ with Y' the Young's modulus obtained from *in situ* DMA measurement. A very good agreement between the experimental and theoretical compliance variation was found, verifying the hydrogen redistribution between the compressed and stretched regions in a bent ligament.

Chapter 3

Materials and Experimental Procedures

3.1 Electrochemical equipment

3.1.1 Potential control system

In this thesis, sample synthesis and mechanical analysis were performed under electrochemical conditions. The potential stimulations were applied by a potentiostat (Metrohm AUTOLAB, PGSTAT302N) and were monitored by the factory-built software NOVA (version 1.11).

3.1.2 Electrochemical cells

Sample preparation, electrochemical characterization, and *in situ* mechanical characterization were carried out in two types of electrochemical cells: Three-compartment cell and one-compartment cell.

Figure 3.1a shows a three-compartment cell with a relatively large volume (500 ml). This cell was used for dealloying, electrochemical reduction (cyclic voltammetry), and *in situ* dilatometry experiments. Figure 3.1c displays a three-compartment cell with a relatively smaller volume (2.5 ml). This cell, mounted in a dynamic mechanical analyzer (DMA), which has limited space, was used for *in situ* dynamic mechanical analysis experiments. In the three-compartment cells, a working electrode (WE) is put in the biggest compartment containing the main body of the working electrolyte. A reference electrode (RE) is placed in a compartment coupled with a Luggin capillary. The small distance between Luggin capillary tip and WE minimizes the resistance between WE and RE. Moreover, RE is separated from working electrolyte which contains dissolved metal ions by the thin Luggin capillary tube and therefore, RE is kept from being contaminated and RE potential keeps stable. A counter electrode (CE) is inserted in the third compartment with a frit inside the tube arm (as shown in Figures 3.1b and d). The one-compartment cell (with a volume of 250 ml), as shown in Figure 3.1e, was used for electropolymerization of pyrrole on nanoporous gold samples. All electrodes were placed in the same chamber containing the polymerization electrolyte. Figures 3.1b, d, and f show the corresponding schematics of the electrochemical cells in Figures 3.1a, c, and e, respectively. The schematics also include the potential control system. In

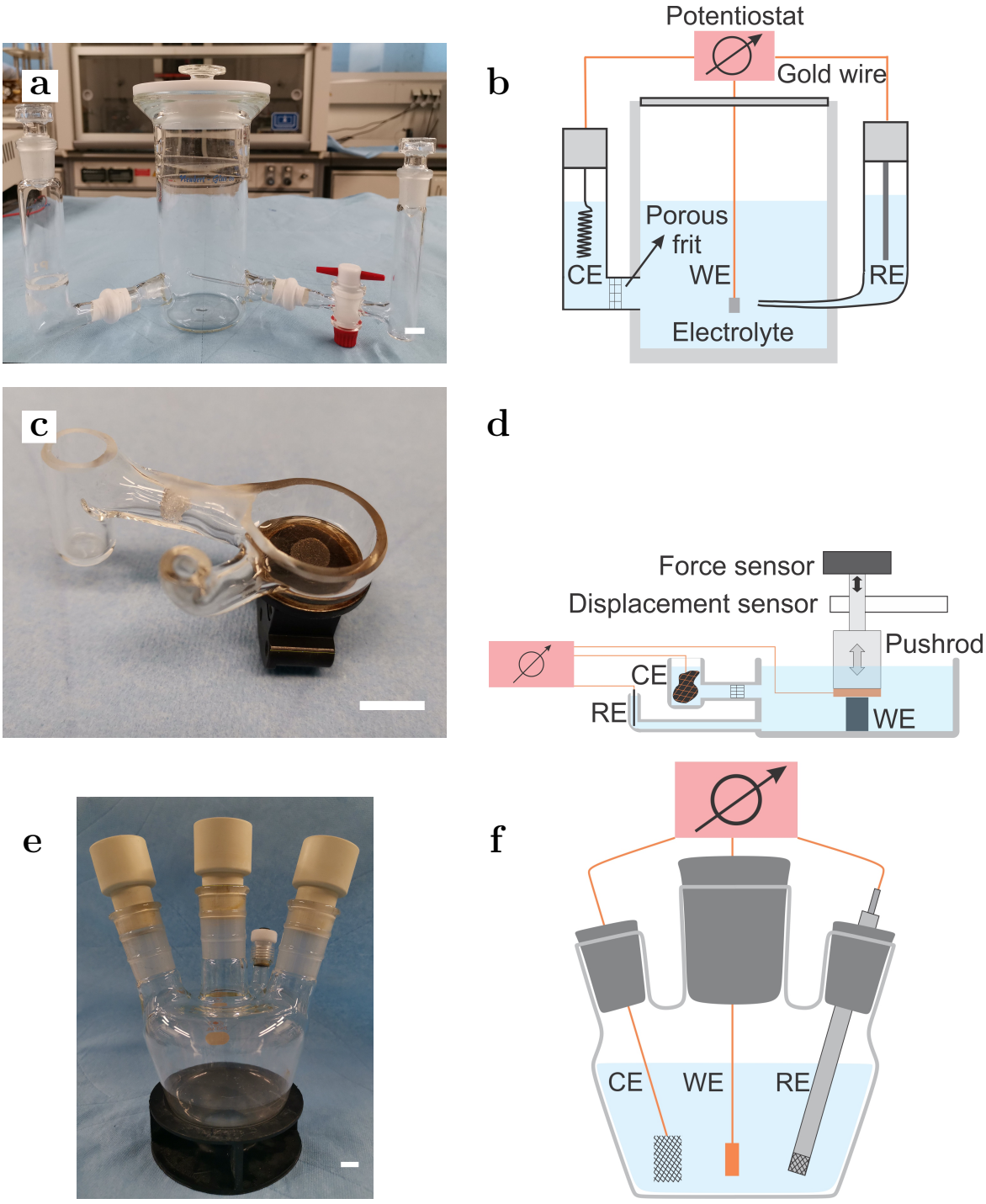

Figure 3.1. Electrochemical cells and the corresponding sketches. (a) Three-compartment cell for dealloying, (c) three-compartment cell for dynamic mechanical analysis (DMA) experiments, (e) one-compartment cell for electropolymerization of pyrrole; (b), (d), and (f) are the schematics of the corresponding cells in (a), (c), and (e) with electrochemical control; (d) shows the schematics of the cell in (c) coupled with dynamic mechanical analyzer (DMA) to perform mechanical testing *in situ* in an electrochemical environment. WE, CE, and RE respectively denote working, counter, and reference electrodes. The white scale bar at the lower right part in (a), (c), and (e) is 1 cm.

addition, the sketches of the force and displacement sensors in DMA are also shown in Figure 3.1d.

Before electrochemical experiments, the cells (in Figures 3.1a and e) were carefully cleaned in Piranha solution (volume ratio of 98% sulfuric acid (H_2SO_4, Sigma-Aldrich, ACS grade) and 30% hydrogen peroxide (H_2O_2, Sigma-Aldrich, ACS grade) is 5:1) and ultrapure water (18.2 MΩ) to prevent contamination by foreign ions or organic matters.

3.1.3 Electrolytes

Different electrolytes were used for specific purposes.

For dealloying, 1 molar L^{-1} aqueous perchloric acid (1 M $HClO_4$) solution was prepared by dissolving aqueous $HClO_4$ (AppliChem, with purity > 99.7%) with a concentration of 60% in ultrapure water. To further remove the residual Ag content in the as-dealloyed samples electrochemical reduction (cyclic voltammetry) experiments were carried out in 1 M $HClO_4$ that was made by mixing aqueous superpure $HClO_4$ (Merck KGaA, with a higher purity > 99.8%) with a concentration of 70% in ultrapure water. For the sake of *in situ* DMA, isotonic actuation, and dilatometry experiments, aqueous $HClO_4$ (superpure $HClO_4$) with a smaller concentration of 0.1 M was utilized to avoid reactivity loss in PPy [192]. After preparation, both 1 M and 0.1 M $HClO_4$ electrolytes were kept for 24 h for homogenization.

The electrolyte for the PPy film synthesis by polymerization was prepared as follows. First, commercial pyrrole (Sigma-Aldrich, 98%) liquid was purified by flowing through a silicon gel in an argon (Ar) atmosphere. The purified pyrrole was colorless and transparent and was kept in Ar. Thereafter, 0.3 M lithium perchlorate ($LiClO_4$, Sigma-Aldrich, 99.99%) and 0.3 M purified pyrrole were dissolved in a mixture of acetonitrile (ACN, Sigma-Aldrich, 99.8%) and ultrapure water with a volume ratio of 98%: 2%. Afterwards, the electrolyte was also placed for 24 h for homogenization.

3.1.4 Electrodes

In all electrochemical experiments, three electrodes were used: working (WE), counter (CE), and reference (RE) electrodes. In the dealloying and electrochemical reduction (cyclic voltammetry) experiments, the electrodes were separately put in the different compartments in the three-compartment cell as indicated in Figures 3.1b and 3.1d. However, in the electropolymerization experiments, all the three electrodes were inserted in the same compartment in the one-compartment cell as shown in Figure 3.1f.

In the dealloying experiments, $Au_{25}Ag_{75}$ cylinders served as WE. A coiled Ag wire was used as CE and was placed in the compartment with a frit inside (as marked in Figure 3.1b). A homemade Ag/AgCl [193] working as RE was inserted in a Luggin capillary and was kept from being contaminated by the metal ions in the working electrolyte to maintain a stable potential.

The homemade Ag/AgCl reference electrode was made by oxidizing an Ag wire (ChemPur, 0.5 mm diameter, 99.99%) in 1 M aqueous hydrochloric acid (HCl, Sigma-Aldrich, ACS grade) solution at 0.9 V versus Ag wire (vs. Ag) for 120 s. During this process, another coiled Ag wire worked as CE and RE. The potential of the homemade Ag/AgCl was measured to be +0.515 V vs. standard hydrogen electrode (SHE) in 1 M $HClO_4$ solution.

In the electrochemical reduction (cyclic voltammetry) experiments, samples (nanoporous gold or nanoporous gold-polypyrrole hybrids) worked as WE, a carbon cloth severed as CE, and the homemade Ag/AgCl was used as RE. The electrodes were placed in the cell as mentioned in section 3.1.2.

In the electropolymerization experiments, all the three electrodes were put in the sample chamber in the one-compartment cell with annealed nanoporous gold, large surface area commercial platinum (Pt) mesh, and commercial Ag/AgCl (filled with 3M KCl solution, 0.208 V vs. SHE, Radiometer Analytical) as WE, CE, and RE, respectively.

Unless otherwise stated, all potential values quoted in this work are on the SHE scale.

3.2 Electrochemical techniques

3.2.1 Chronoamperometry

Chronoamperometry is a technique in which an invariant potential is applied to the working electrode by a potentiostat. This technique was mainly used for making nanoporous gold (section 3.3.2), electropolymerization of pyrrole (section 3.3.3), and for electromechanical experiments (section 3.5), in which constant potential is applied. In a specific chronoamperometry experiment, a constant potential is imposed for a desired time or until the resulting current falls below a critical value.

3.2.1.1 Constant potential

A constant potential was applied to make nanoporous gold by dealloying. A typical potential-time plot of dealloying $Au_{25}Ag_{75}$ cylinders in 1 M $HClO_4$ is shown in Figure 3.2a, the potential was held for the whole duration of the procedure. The corresponding current and transferred charge versus time are depicted in Figure 3.2b and Figure 3.2c, respectively.

3.2.1.2 Potential pulse

The potential pulse method was used in PPy preparation experiments. A potential was applied for a short time and the corresponding current and the transferred charge were recorded. Figure 3.3 plots the potential, current, and charge of the first 4 pulse cycles with respect to time. Between every two pulses, the potential was switched off, and the system was under open circuit condition so that no current or charge flow.

3.2.1.3 Potential steps

The potential step method consists of a series of potentials applied for a defined time. Figure 3.4 represents a few potential steps and the corresponding current and transferred charge of nanoporous gold-polypyrrole in 0.1 M $HClO_4$ during *in situ* DMA experiments. Upon changing potential values, current and charge invert their signs.

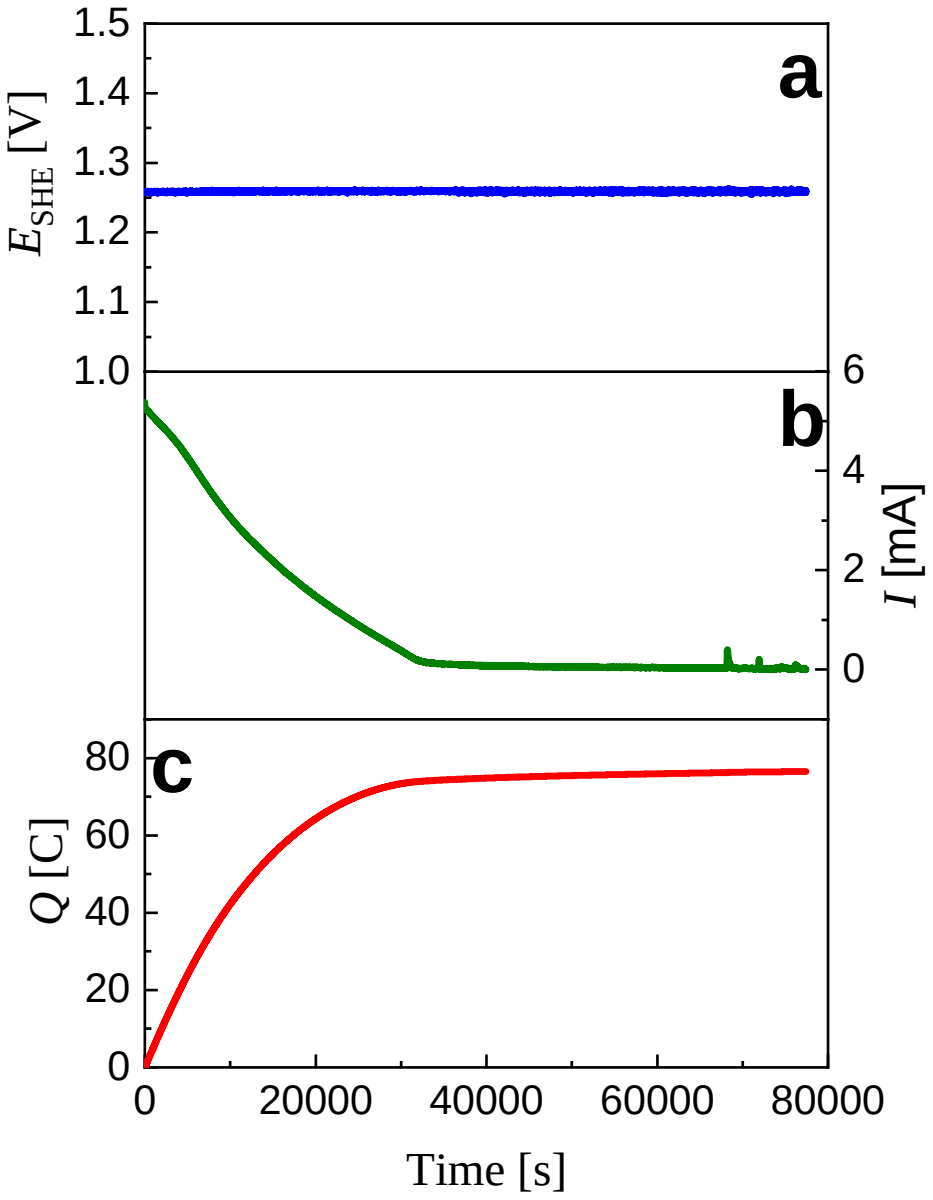

Figure 3.2. Dealloying of $Au_{25}Ag_{75}$ cylinders by chronoamperometry method in 1 M $HClO_4$. (a) Blue line and top-left coordinate: Constant potential with respect to time; (b) green line and right coordinate: The corresponding current during dealloying; (c) red line and bottom-left coordinate: The transferred charge during dealloying.

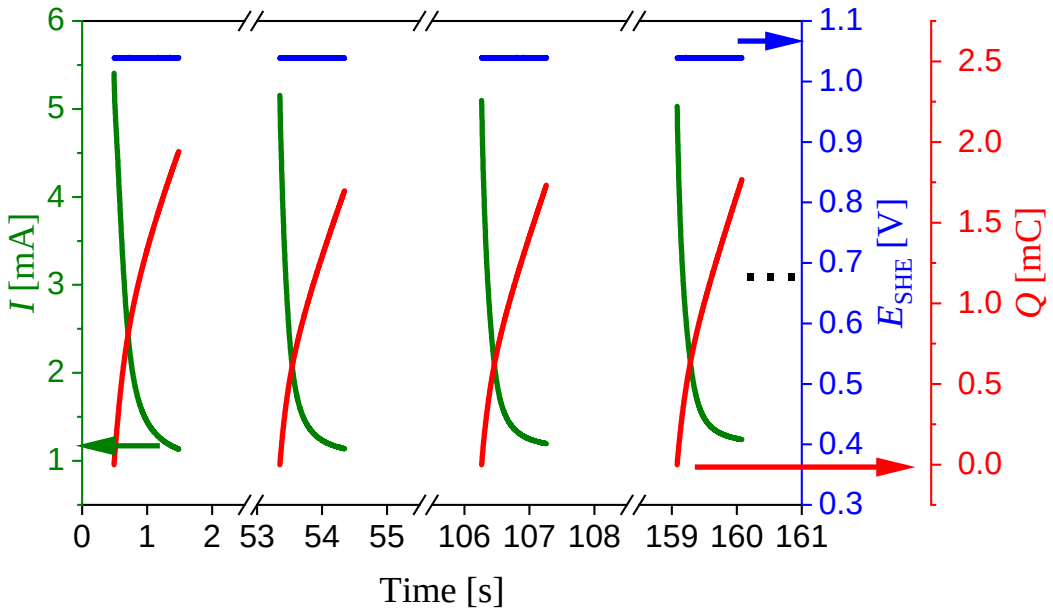

Figure 3.3. An example showing potential pulse procedure in the PPy preparation experiments. Blue lines and coordinate: Potential pulse; green lines and coordinate: The resulting current under potential pulse; red lines and coordinate: The corresponding transferred charge. Potential is switched off between two potential pulses and no current or charge was generated.

3.2.2 Cyclic voltammetry

Cyclic voltammetry (CV) is a technique for sample preparation and electrochemical analysis. In this work, CV was used for (1) electrochemical reduction of as-dealloyed NPG to further reduce the residual Ag content in the ligaments, (2) determination of the electrochemically active surface area of NPG, and (3) providing potential control on NPG and NPG/PPy during *in situ* mechanical tests.

In a typical CV cycle, as shown in Figure 3.5a, potential scanning starts at the starting potential, E_0, and sweeps to the upper potential limit, E_{max}, at a given scan rate, v. When the potential reaches E_{max}, it starts to scan back to the lower potential limit, E_{min}, and finally returns to E_0. As a result, the current response is recorded as a function of the potential. The current is plotted versus potential and a cyclic voltammogram (CV curve) is obtained.

During this process, the potential sweeps in a linear manner (linear scan mode) at a constant rate. However, in practice, potentiostat cannot apply a linear potential ramp below 10 mV/s. Whereas, this can be overcome by a staircase mode.

In the linear scan mode, potential varies linearly at a scan rate of $\Delta E/\Delta t$ (the slope of the dotted line in Figure 3.5b) [194]. The current is the response to the potential variation and the involved charge can be obtained by integrating the current-time curve. The transferred charge equals to the area (the sum of the gray rectangle and the slash lines filled areas in Figure 3.5c) beneath the green line. In the staircase mode, potential varies stepwise with an amplitude of ΔE within a time interval of Δt, as shown in Figure 3.5b [195]. Current is generated at every potential step and is sampled at the end of the potential step (as marked by symbol '*' in Figure 3.5c) by the potentiostat [194, 196], measuring the Faradic current only. Therefore, the corresponding charge (which equals to the area of gray rectangles in Figure 3.5c) from staircase mode is underestimated.

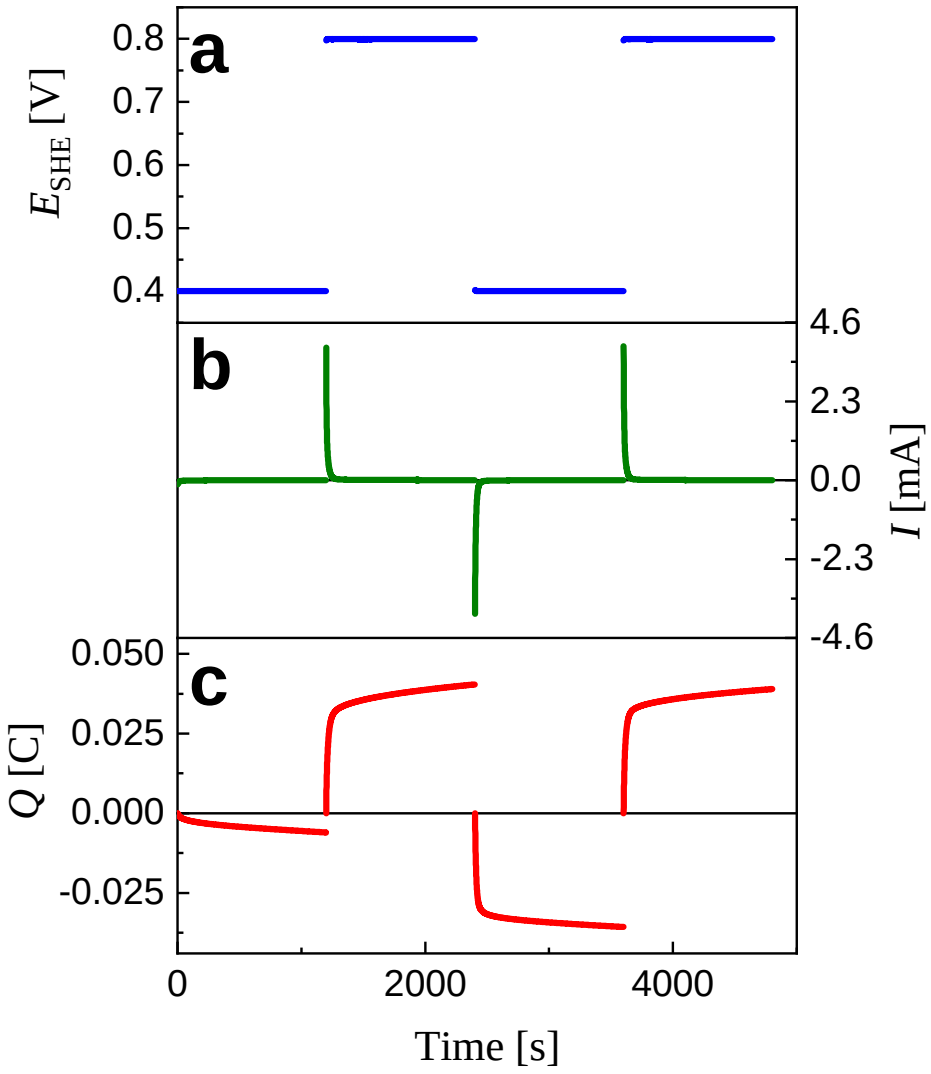

Figure 3.4. A typical potential step procedure showing (a) an applied electrode potential, E_{SHE}, and the corresponding (b) current, and (c) transferred charge versus time of nanoporous gold-polypyrrole in 0.1 M $HClO_4$ during *in situ* DMA analysis.

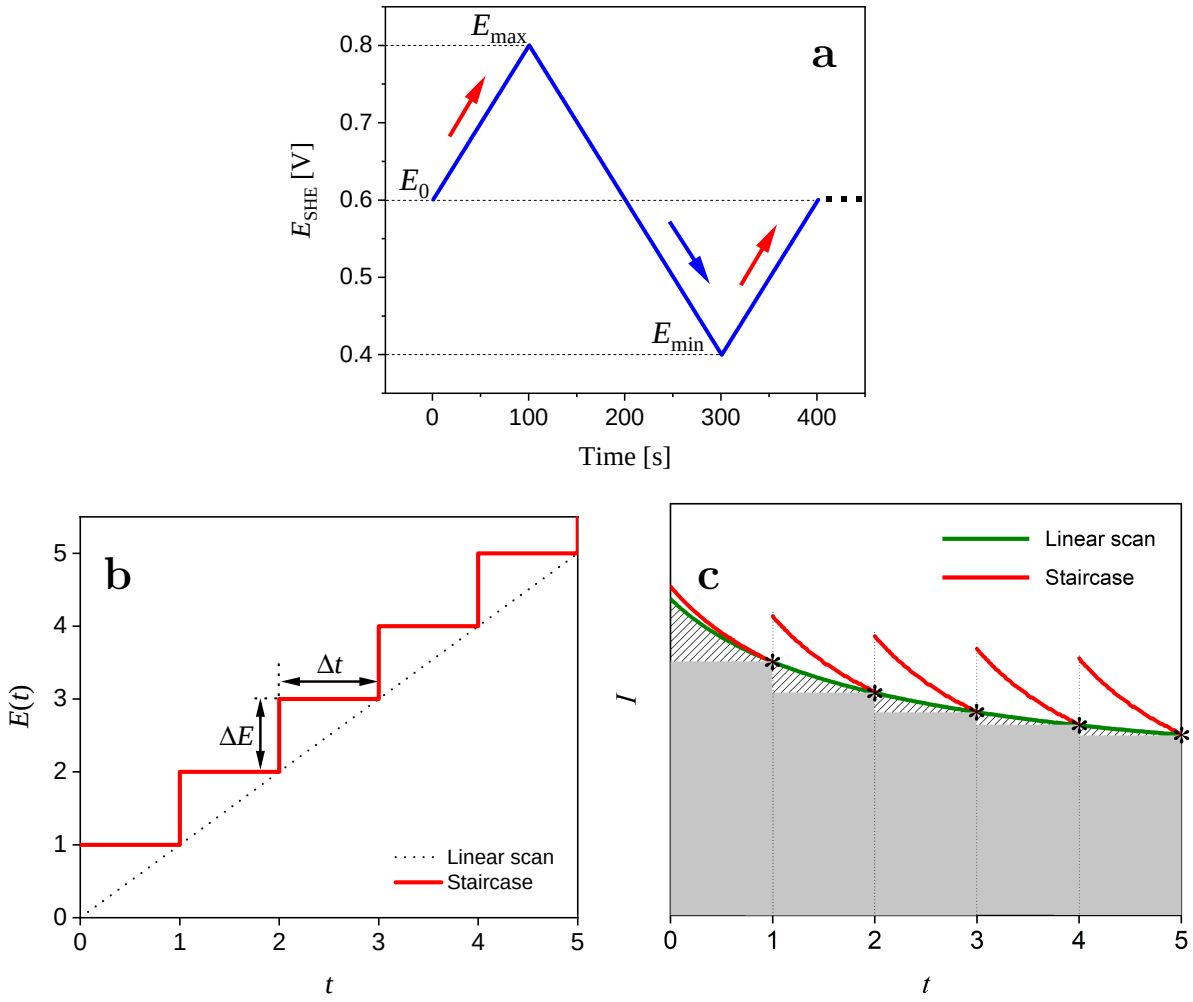

Figure 3.5. Potential waveforms in a typical cyclic voltammetry experiment. (a) Electrode potential, E_{SHE}, versus time for NPG/PPy in 0.1 M $HClO_4$ at a scan rate of 2 mV/s. The red arrow indicates the positive (anodic) scanning and the blue arrow means negative (cathodic) sweeping. Potential sweeps between the upper limit, E_{max}, and lower limit, E_{min}. (b) Schematics representing the input potential signals of the staircase (red solid line) and linear scan (black dotted line) versus time. Linear scan potential ramps with a slope of $\Delta E/\Delta t$, staircase potential inputs signal with potential step amplitude of ΔE. (c) Schematics showing the current responses of the linear scan (green line) and staircase (red) of the corresponding potential variation modes in (b). The symbol '*' in (c) indicates the end of a potential step, at which the current was sampled. The symbol '*' also defines the way to calculate the transferred charge (equal to the area of the gray rectangular) during one potential step in the staircase. The region (both the slash lines filled area and the gray rectangle area) underneath the linear scan current represents the transferred charge during the linear scan.

In this thesis, in order to reduce the effect of porous structure on the ions diffusion, planar Au/PPy hybrids with different PPy thicknesses were used to investigate the differences between linear scan and staircase voltammetry section 3.3.4. The potential step, ΔE, in staircase voltammetry was 0.002 V by default, and the corresponding interval time, $\Delta t = 1$ s, of the scan rate of 2 mV/s is much bigger than the charging time in PPy (33 ms for 158 nm-thick PPy [197]).

3.3 Sample preparation

In this thesis, mechanical experiments were carried out on mm-sized nanoporous gold (NPG) or nanoporous gold-polypyrrole (NPG/PPy) samples. The samples were prepared by following the procedures below.

3.3.1 Preparation of master alloy

Sample preparation starts from making $Au_{25}Ag_{75}$ (at.%) cylinders, the precursor of NPG. $Au_{25}Ag_{75}$ ingots were made by melting Au (ChemPur, 99.995%) and Ag (ChemPur, 99.99%) in an arc-melting furnace (Compact arc melter MAM-1, Edmund Bühler) under the protection of argon (Ar) atmosphere. Then the ingots were sealed into a quartz glass tube under vacuum and annealed at 800 °C for 120 h. The homogenized ingots were rolled into wires with a diameter of ~ 1.2 mm. Afterwards, the wires were cut into ~ 1.7 mm long cylinders by a wire-saw (Well diamond saw, Model 3032). The rolling and wire-cutting induced residual stress in the cylinders were diminished by annealing at 600 °C for 2 h in Ar, and finally, $Au_{25}Ag_{75}$ master alloys were prepared.

3.3.2 Preparation of NPG

Nanoporous gold was produced by electrochemically dealloying $Au_{25}Ag_{75}$ cylinders at room temperature (RT) in 1 M $HClO_4$ with $Au_{25}Ag_{75}$ cylinders, coiled Ag wire, and homemade Ag/AgCl electrode working as WE, CE, and RE, respectively. The dealloying process was carried out under a constant potential of 0.75 V vs. homemade Ag/AgCl. During dealloying, the current gradually decays and the potential was stopped when the current falls below 10 μA as indicated in Figure 3.2. The total dealloying time depends on the number of samples and sample dimensions. Afterwards, the residual Ag in the as-dealloyed samples was further depleted by electrochemical reduction experiments, during which potential was swept between -0.5 V and 1.0 V (vs. homemade Ag/AgCl) for successive 15 cycles at a scan rate of 5 mV/s. After electrochemical reduction experiments, the residual Ag content in the samples was less than 2 at.%. The samples were then immersed in water for 24 h to remove the residual electrolyte and ions. The samples were then dried and stored in fume hoods.

The as-dealloyed NPG samples have an average ligament size, L_D, of ~ 20 nm. The samples were annealed in an infrared furnace (behr IRF 10, IDL GmbH & Co KG) at 300 °C in air for 30 min, which resulted in $L_D = 160 \pm 40$ nm. This was necessary to produce large enough pores that would afford a uniform deposition of PPy coating.

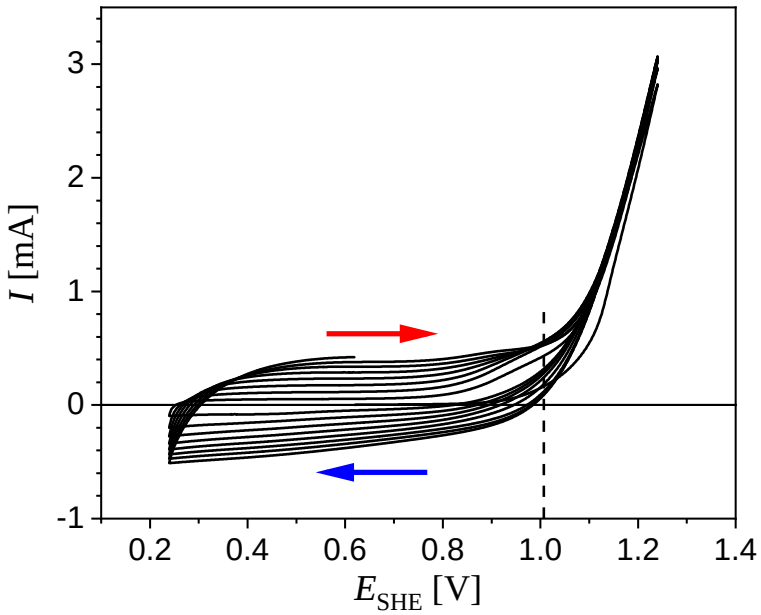

Figure 3.6. Cyclic voltammograms (CV) of NPG in ACN solution containing 0.3 M $LiClO_4$, 0.3 M pyrrole, and 2 vol.% H_2O at a scan rate of 5 mV/s. The dashed line denotes the electropolymerization potential (0.8 V vs. commercial Ag/AgCl), after which current, I, increases drastically. Red and blue arrows indicate the anodic and cathodic scan directions, respectively.

3.3.3 Preparation of NPG/PPy hybrids

NPG/PPy hybrids were prepared by electropolymerizing pyrrole on the annealed NPG at RT in a glove box filled with Ar. The electropolymerization was carried out with NPG, Pt mesh, and commercial Ag/AgCl electrode as WE, CE, and RE, respectively. The electrodes were put in a one-compartment cell containing 200 ml of the electropolymerization electrolyte as indicated in Figure 3.1f. Before electropolymerization, NPG was immersed in electrolyte for 30 min to ensure complete wetting of NPG with electrolyte (ACN containing 0.3 M $LiClO_4$, 0.3 M pyrrole, and 2 vol.% H_2O). Afterwards, depending on the desired PPy film thickness, a number of successive potential pulses (section 3.2.1.2) were applied and the electropolymerization was initiated.

The electropolymerization potential was determined by applying cyclic potential sweeps on NPG, which was placed in the cell filled with the polymerization electrolyte. The cyclic voltammograms recorded are shown in Figure 3.6. It can be seen that the current starts to increase at 1.1 V, where pyrrole oxidation takes place [198, 199]. Thus, in this work, the potential used for PPy preparation was chosen to be 0.8 V (vs. commercial Ag/AgCl), avoiding the PPy degradation at a higher potential [200].

In a typical potential pulse cycle, for the purpose of PPy deposition, a potential of 0.8 V was applied for 1 s. In order to replenish the consumed pyrrole monomers in the porous space of NPG, the potential was switched off for 50 s to allow the electrolyte transport into NPG pores. After electropolymerization, the as-prepared NPG/PPy samples were cleaned with ultrapure water for 24 h and then kept in a fume hood. In addition, during the electropolymerization process, the consumed charge was recorded by the potentiostat. This allows to estimating the amount of the deposited PPy. The

theoretical PPy mass could be estimated as follows [87, 201]:

$$m_{\text{th}} = \frac{Q}{(2+x)F}(M_{\text{Py}} + xM_{\text{ClO}_4^-}) \tag{3.1}$$

where Q is the consumed charge, $M_{\text{Py}} = 67$ g/mol is the molar mass of pyrrole (Py) monomer [6], $M_{\text{ClO}_4^-}$ is the molar mass of ClO_4^-, x is the doping level which generally takes a value of 0.3 [165, 202], and F is the Faraday constant.

Therefore, the theoretical thickness of the deposited PPy can be estimated as:

$$t_{\text{th}} = \frac{m_{\text{th}}}{A * \rho_{\text{PPy}}} \tag{3.2}$$

where ρ_{PPy} is the density of PPy layer (~ 1.5 g/cm^3 [134, 203, 204]) and A is the NPG surface area that was estimated as described in section 3.4.3.

3.3.4 Preparation of Au/PPy hybrids

In order to evaluate the difference between the linear scan and staircase voltammetry, planar Au/PPy hybrids with different PPy thicknesses were synthesized so that different current and charge responses were recorded. The Au/PPy hybrids were fabricated as follows.

The PPy film was electropolymerized on the planar Au surface of an electrochemical quartz crystal microbalance (EQCM) with a surface area of 0.36 cm^2. The electropolymerization process was the same as that described in section 3.3.3. By tuning the potential pulses, PPy films with 20 nm and 1200 nm were synthesized, which corresponds to PPy volume of 7.22×10^{-4} mm^3 and 4.33×10^{-2} mm^3, respectively.

3.4 Characterization

3.4.1 Microstructure and composition characterization

The microstructure and chemical composition of NPG and NPG/PPy were characterized by scanning electron microscopy (SEM, Zeiss, Supra55) coupled with an energy dispersive X-ray analyzer (EDX, Oxford X-Max 20 SDD). Before characterization, a sample was cut into two pieces in the middle to get fresh fracture surfaces of the central parts of the material. The pieces were glued on an aluminum stub using silver paint. SEM worked under in-lens mode with the accelerating voltage of 15 kV and the working distance of 4.7 mm. EDX worked under an accelerating voltage of 15 kV and a working distance of 8 mm. The ligament sizes and PPy film thicknesses were obtained by averaging more than 30 measurements of bare NPG and NPG/PPy hybrids by ImageJ.

3.4.2 Electrochemical characterization

The electrochemical properties of NPG and NPG/PPy were evaluated by subjecting the specimens to cyclic voltammetry. A study on the chemical stability of PPy demonstrates that a low acid concentration is more preferable to maintain the electroactivity of PPy [192]. Moreover, it has been revealed that the actuation amplitude decreases by 30% when electrolyte concentration increases from 0.1 to 1 M, whereas the amplitude

is little improved when the electrolyte is diluted to 0.01 M [185]. Therefore a 0.1 M $HClO_4$ was used in this work.

Based on the results in section 4.4 and the report in Ref. [109], PPy films were over-oxidized above 0.9 V. Therefore, the upper vertex potential of 0.8 V was applied in this work to obtain a reliable electrochemical behavior of PPy. On the other hand, to avoid the reactions (e.g., hydrogen and oxygen reduction) of aqueous electrolytes [29, 205], a potential of 0.4 V was selected as the lower vertex potential. The selected potential window between 0.4 and 0.8 V corresponds to the capacitive charging-discharging processes at the gold-electrolyte interface, and no Faradic reactions take place [43].

3.4.3 Surface area determination

In general, the surface area A is normalized to mass or volume, termed as mass specific surface area, α_m, or volume specific surface area, α_V, respectively. They are related as follows [206]:

$$\alpha_V = \frac{A}{V} = \frac{A}{m}\rho = \alpha_m \rho \tag{3.3}$$

where V is the volume of solid phase in a porous material, m is the sample mass, and ρ is the density of massive Au.

The relationship between characteristic structure size (idealized, cylindrical ligament size, L_D) and volume specific area (α_V) has been described in Ref. [207]:

$$\alpha_V = \frac{g}{L_D} \tag{3.4}$$

where the geometry constant g equals 4. Eq. 3.5 works well in predicting the structure size of NPG with clean surface [51, 207].

Substituting the α_V in Eq. 3.3 with Eq. 3.4, the surface area is obtained:

$$A = \frac{g}{L_D} V \tag{3.5}$$

The surface area can also be estimated via the capacitance ratio method [206]. Cyclic voltammograms at various sweep rates are recorded in a narrow potential window where only charging-discharging processes take place. The current in the middle of the potential window, I_m, is plotted as a function of sweep rate, $v = dE/dt$, obtaining a straight line whose slope gives the total capacitance C:

$$C = \frac{dQ}{dE} = I_m \frac{dt}{dE} = \frac{I_m}{\frac{dE}{dt}} = \frac{I_m}{v} \tag{3.6}$$

where Q is the total charge involved in the double layer charging-discharging at a metal-electrolyte interface.

The surface area is thus determined by dividing the total capacity of NPG by the specific double layer capacitance (capacitance per area) C^* of an unoxidized planar gold with a clean surface.

$$A = \frac{C}{C^*} \tag{3.7}$$

The specific capacitance of a polycrystalline Au electrode was reported to be related to both surface condition and electrolyte concentration [169, 208]. Here, C^* takes a value of 20 $\mu F/cm^2$ in 0.1 M $HClO_4$ [209].

3.5 Measurement of mechanical properties and mechanical testing setups

The dealloying conditions employed in this thesis enable one to obtain mm-sized NPG specimens without cracks [22, 83]. The NPG specimens can be compressed up to a high strain of 60% without a failure [71]. In this work, the mechanical behavior of NPG and NPG/PPy hybrids were also studied under compression. The cylindrical specimens for the testing were straight and uniform in cross section with a diameter of ~ 1 mm and a length of ~ 1.6 mm. The mechanical properties, including strength, elastic (or Young's) modulus as well as macroscopic length variations were studied as described below.

3.5.1 *In situ* dilatometry

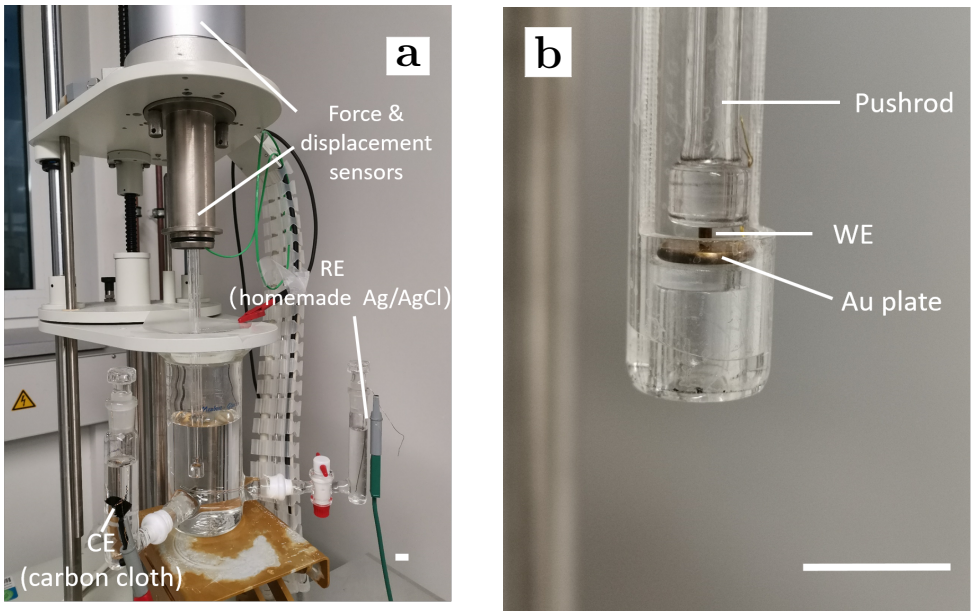

Figure 3.7. (a) Photograph of *in situ* dilatometer setup: A dilatometer coupled with a three-electrode chemical cell filled with 0.1 M $HClO_4$. (b) Pushrod and WE at a higher magnification. WE: working electrode (NPG or NPG/PPy hybrids); CE: counter electrode (carbon cloth); RE: reference electrode (homemade Ag/AgCl). Via a pushrod, a slight force of 0.2 N was applied and the displacement was monitored with the help of the force and displacement sensors marked in (a). Au plate made electrical contact with WE, CE, and RE. The white scale bars at the lower right of (a) and (b) indicate 1 cm.

Figure 3.7a shows the photos of a vertically constructed dilatometer (L75 Platinum Series, Linseis Messgeräte GmbH, Germany) coupled with a three-compartment electrochemical cell. The enlarged graph demonstrates the pushrod pressing a sample that stands on a gold plate (Figure 3.7b). A typical *in situ* dilatometry experiment was performed at RT in 0.1 M $HClO_4$ with NPG or NPG/PPy as WE, carbon cloth, and homemade Ag/AgCl as CE and RE, respectively. During the measurement, a small force of 200 mN (corresponding to ~ 0.27 MPa) was applied by the pushrod which is connected to a displacement sensor. By tuning the electrochemical conditions the resulting sample length variations were well recorded by the dilatometer.

3.5.2 Mechanical testing machine

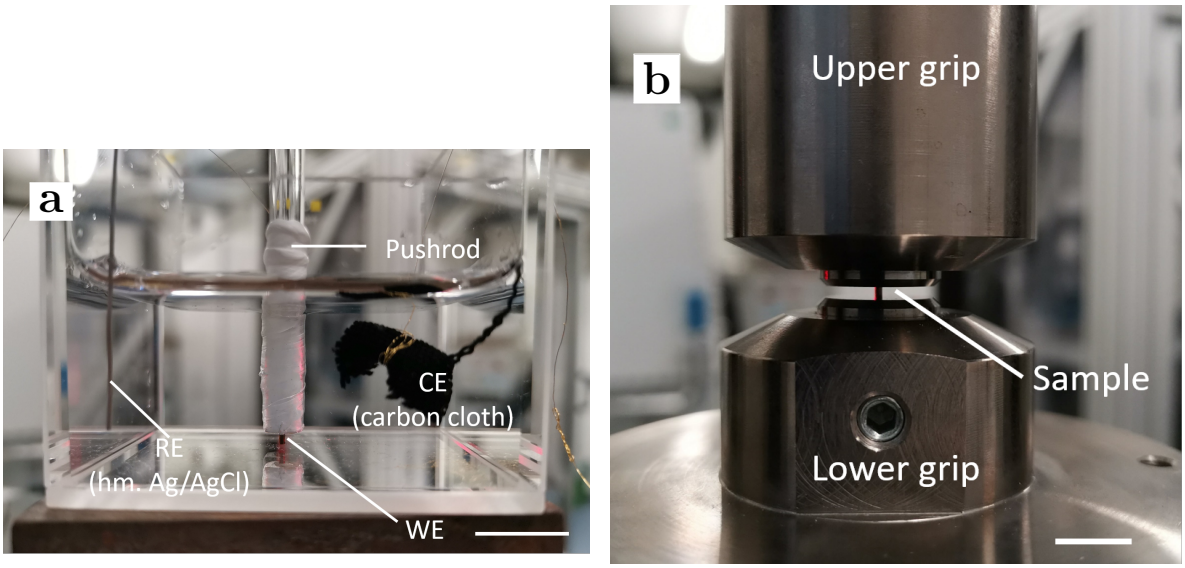

Figure 3.8. (a) Electrochemical cell built in compression machine (Zwick/Roell Z010) for *in situ* compression in 0.1 M $HClO_4$. WE: working electrode (NPG or NPG/PPy hybrids), CE: counter electrode (carbon cloth), RE: reference electrode (homemade Ag/AgCl). WE was placed under the pushrod which transferred force from the compression machine. (b) The setup for compression test in the air with sample (NPG or NPG/PPy hybrids) locating between upper and lower grips. The white scale bars at the lower right of (a) and (b) indicate 1 cm.

3.5.2.1 *In situ* compression

In situ compression tests were carried out on NPG/PPy hybrids using a mechanical testing machine (Zwick/Roell Z010, ZwickRoell) coupled with electrochemical setups. A mm-sized cylindrical sample was placed under the pushrod, as shown in Figure 3.8a. The compression was performed at a constant engineering strain rate of $10^{-4}s^{-1}$ monitored by the program. During experiments, the sample length variations were detected by laser speckle extensometer (Zwick laserXtens, ZwickRoell). The deformations of the pushrod and electrochemical cell were considered to be negligibly small so that the detected length changes were only from the samples.

In a typical experiment, a constant force (e.g., 5 N) was set for a certain period of time and cyclic voltammetry or potential steps were simultaneously applied to change the oxidation state of NPG/PPy.

In the study of the actuation under load, a series of loads were applied to obtained different deformation degrees of the sample. The actuation was then monitored upon charging the sample in the electrolyte.

3.5.2.2 Load-unload test

The strength and elastic modulus of NPG or NPG/PPy hybrids were obtained from a load-unload stress-strain curve. The load-unload experiments were performed using the mechanical testing machine. As shown in Figure 3.8b, a sample was placed between the

grips, and the compression was carried out with a strain rate of $10^{-4}s^{-1}$. The sample was unloaded up to 2 N when an engineering strain reached a certain strain level. Afterwards, a load was again applied until the next strain level. All load-unload steps were controlled by a custom designed program in 'testXpert II'. After the experiments, the stress-strain curves with load-unload loops were obtained.

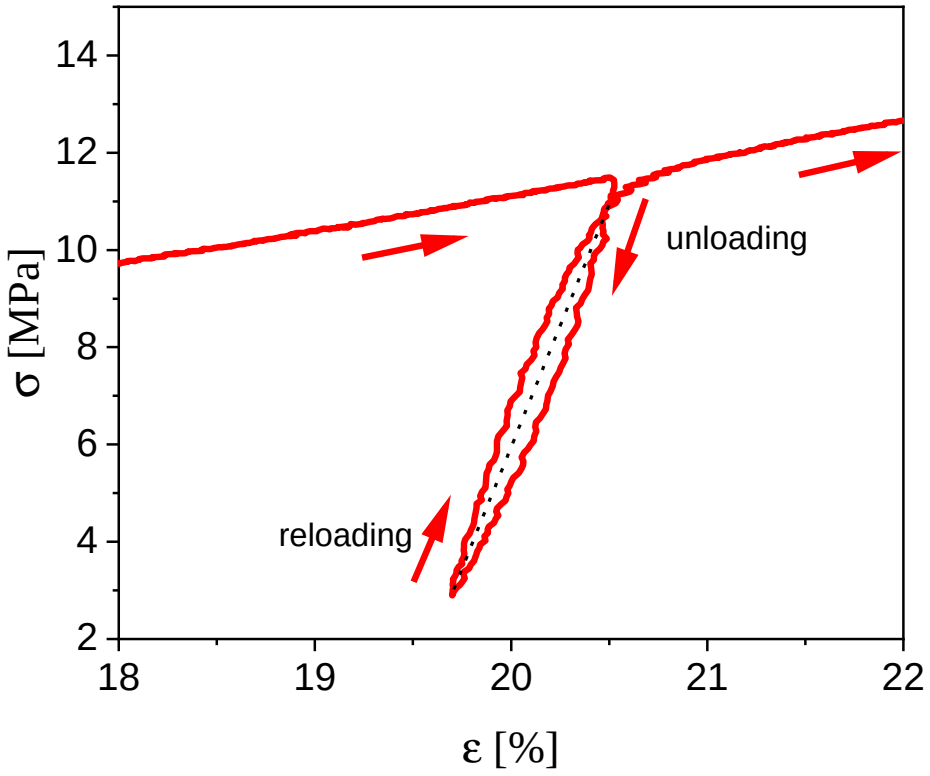

Figure 3.9. A typical loading-unloading segment of NPG. Dashed line denotes the way for determination of Young's modulus.

The Young's moduli were determined from the load-unload segments in the stress-strain curve. A dashed line (as shown in Figure 3.9) was drawn between the intersects of unloading-reloading segments. The Young's modulus was estimated from the slope of the dashed line. It should be noted that Young's modulus of a nanoporous metal is dependent on several factors, including the ligaments size, the ligament connectivity, and the solid fraction [210].

3.5.3 *In situ* dynamic mechanical analysis

Performing the loading-unloading measurement in a mechanical testing machine allows one to obtain the Young's modulus of a nanoporous material. However, at these experimental conditions, the nanoporous materials are always compressed to a large extent (section 3.5.2.1) and only a few values of the elastic modulus are obtained at different strains. A dynamic mechanical analyzer overcomes this problem. When a sample is clamped in the device, a static force is applied to ensure good contact between the sample and the pushrod during the measurement. A sinusoidal force or strain oscillation with a defined frequency is applied as the input, and the output displacement or force is recorded, as illustrated in Figure 3.10.

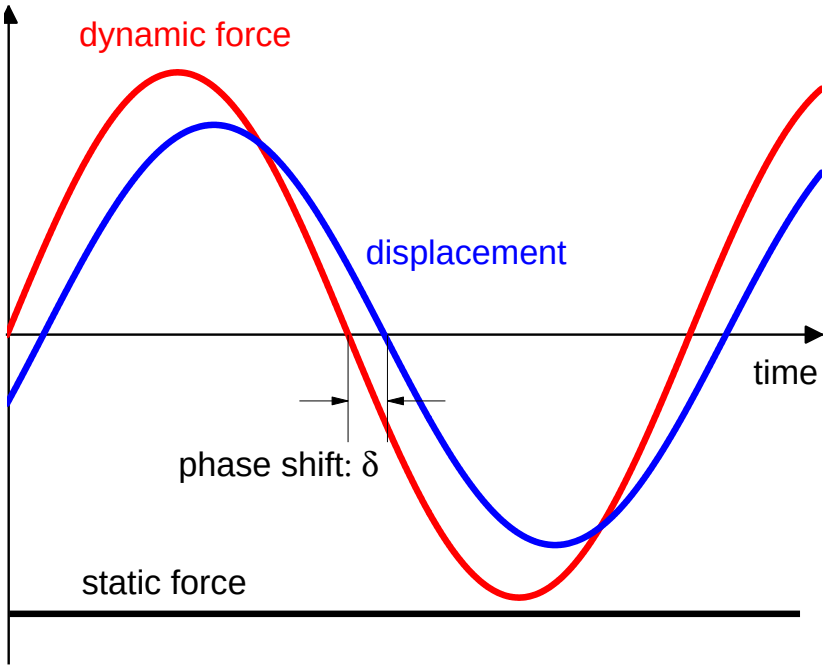

Figure 3.10. Schematics of dynamic mechanical analysis: The sinusoidal force and displacement with a phase shift of δ.

The applied stress as a function of time is described as:

$$\sigma(t) = \sigma_0 \sin(\omega t) \tag{3.8}$$

where σ_0 is the applied maximum stress and ω defines the frequency.

The resulting output strain of a viscoelastic material is observed with a phase shift δ, and the strain is:

$$\varepsilon(t) = \varepsilon_0 \sin(\omega t + \delta) \tag{3.9}$$

where ε_0 is the maximum actuation strain.

According to Hookes law, at uniaxial loading conditions, the input stress and output strain are associated with dynamic Young's modulus, $E^*(\omega)$:

$$\sigma(t) = E^*(\omega)\varepsilon(t) \tag{3.10}$$

where the dynamic Young's modulus is given by:

$$E^*(\omega) = E'(\omega) + iE''(\omega) \tag{3.11}$$

where $E' = (\sigma_0/\varepsilon_0)\cos(\delta)$ is the real part known as storage modulus which features the energy stored per cycle; whereas $iE'' = (\sigma_0/\varepsilon_0)\sin(\delta)$ is the imaginary part defined as loss modulus that characterizes the energy dissipated.

In this work, *in situ* DMA experiments were carried out using a dynamic mechanical analyzer (DMA/SDTA861^e, METTLER TOLEDO) equipped with a three-electrode electrochemical cell (in Figure 3.1c) as illustrated in Figure 3.11a. The tested specimen was placed in the middle of the cell and compressed by the pushrod (Figure 3.11b). The electrochemical reactions were carried out in 0.1 M $HClO_4$ at RT, with NPG or NPG/PPy as WE, carbon cloth as CE, and homemade Ag/AgCl as RE. The cyclic

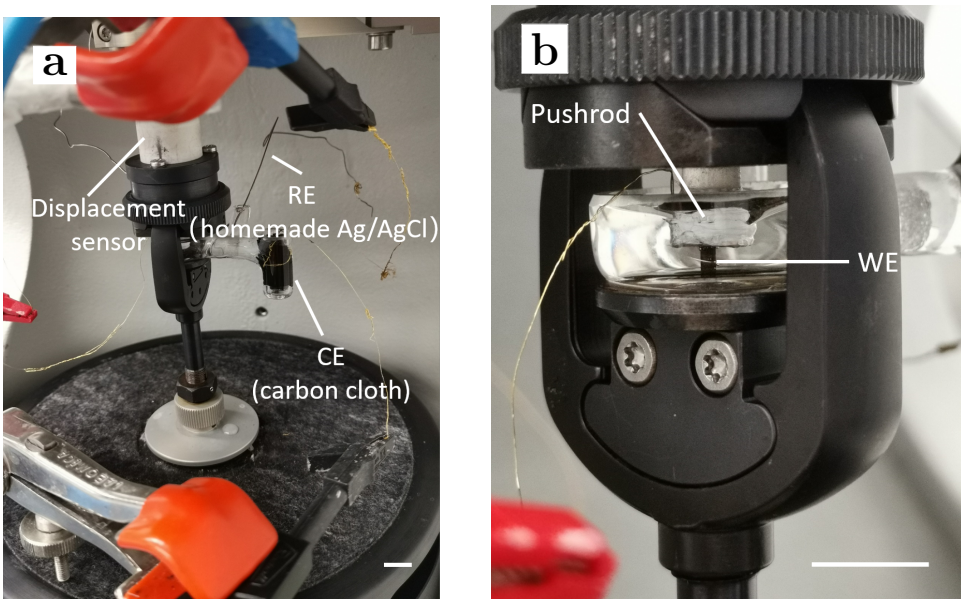

Figure 3.11. (a) *In situ* DMA setup consisting of the dynamic mechanic analyzer and three-electrode electrochemical cell filled with 0.1 M $HClO_4$. (b) Pushrod and WE at a higher magnification. WE: working electrode (NPG or NPG/PPy specimen), RE: reference electrode (homemade Ag/AgCl), CE: counter electrode (carbon cloth). A gold plate is attached to the pushrod for electrical contact. The dynamic and static forces passed via the pushrod and were applied to WE. Sample length change was detected by the displacement sensor marked in (a). The white scale bars at the lower right of (a) and (b) indicate 1 cm.

voltammetry was applied by the potentiostat. In a typical experiment, a dynamic force with a peak-to-peak amplitude of 0.5 N and a frequency of 1 Hz was applied. In order to keep good contact between DMA pushrod and working sample a, 5 N static force was imposed. When measuring the actuation under loads, a series of loads ranging from 1 to 18 N were exerted with other parameters unvaried.

Chapter 4

Results

4.1 Microstructure characterization of NPG

Samples of mm-sized nanoporous gold (NPG) were successfully fabricated by mean of electrochemical dealloying of $Ag_{75}Au_{25}$ under 1.265 V (vs. standard hydrogen electrode, SHE) and the subsequent 15 cycles electrochemical reduction in the potential range of 0.015 V ~ 1.515 V. As shown in Figure 4.1a, a smooth fracture surface of the central part of a typical specimen suggests that no cracks were formed. As marked in Figure 4.1a, a series of sites from the outer to the middle of the fracture surface were selected to inspect the chemical composition of NPG. Energy dispersive X-ray spectroscopy (EDX) analysis was carried out on those spots and a typical EDX spectrum of the central part of the sample is shown in Figure 4.1c. From the spectrum one can see that Ag cannot be completely removed by dealloying, which is in accordance with previous results [26, 42, 211]. The composition analysis reveals a residual Ag concentration of ~ 2.7 at.%.

A typical microstructure of NPG is shown in Figure 4.1b. A bicontinuous network is constructed by plenty of nanoscale ligaments with the mean characteristic width of ligaments $L_D = 27 \pm 4$ nm. In this work, *in situ* mechanical experiments were performed on NPG/PPy electroactuators with the remaining pore space filled with electrolyte which supplies a pathway for ionic diffusion and conduction. The pore space in NPG network should be large enough for the accommodation of PPy film deposition on gold ligaments and the electrolyte flow in the remaining pores. Therefore, the initial ligament-pore network in NPG should be coarsened. Annealing of NPG in the air is a facile way to grow ligaments and pores [26, 131]. Figure 4.2 depicts the microstructure of the annealed NPG. Clearly, the small ligaments have grown to the larger ones with the mean characteristic width $L_D = 160 \pm 40$ nm. The enlarged nanopores have enough space for PPy deposition and the diffusion of the electrolyte. The solid fraction, φ (estimated using $\varphi = \rho_{NPG}/\rho_{Au} = m_{NPG}/V_{NPG}/\rho_{Au}$, with ρ_{NPG}, ρ_{Au}, m_{NPG}, and V_{NPG} respectively representing density of NPG and the monolith Au, and the measured mass and outer volume of NPG), of the annealed NPG is 0.31 ± 0.009.

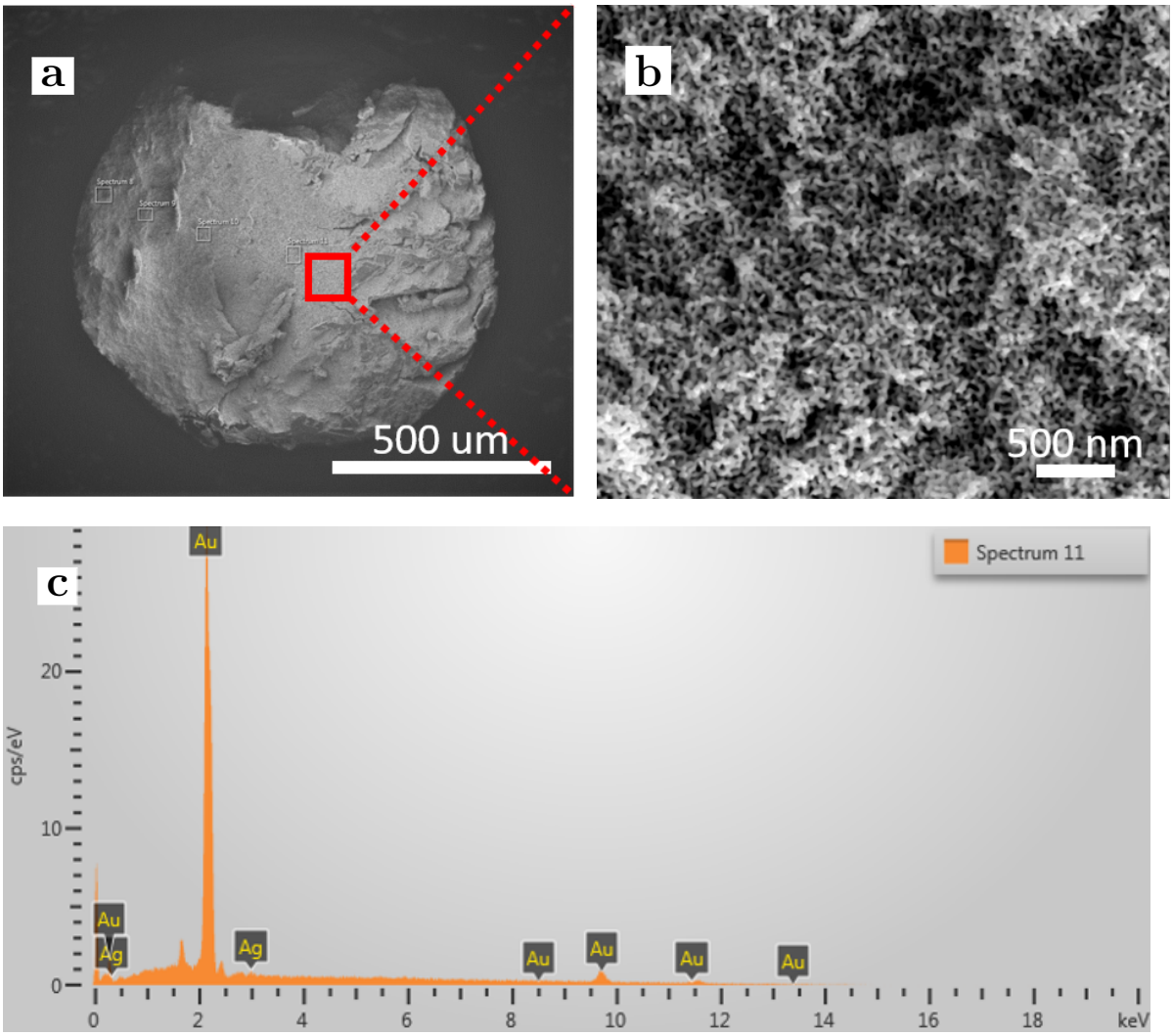

Figure 4.1. Microstructure and composition characterization of NPG. (a) Scanning electron microscopy (SEM) picture of the fracture surface of NPG fabricated by electrochemical dealloying and electrochemical reduction. (b) SEM image showing the microstructure in the area (red mark in a) at the larger magnification, showing the diameter of the ligaments $L_D = 27 \pm 4$ nm. (c) A representative energy dispersive X-ray (EDX) spectroscopy spectrum showing the composition of the central part of the sample shown in (a).

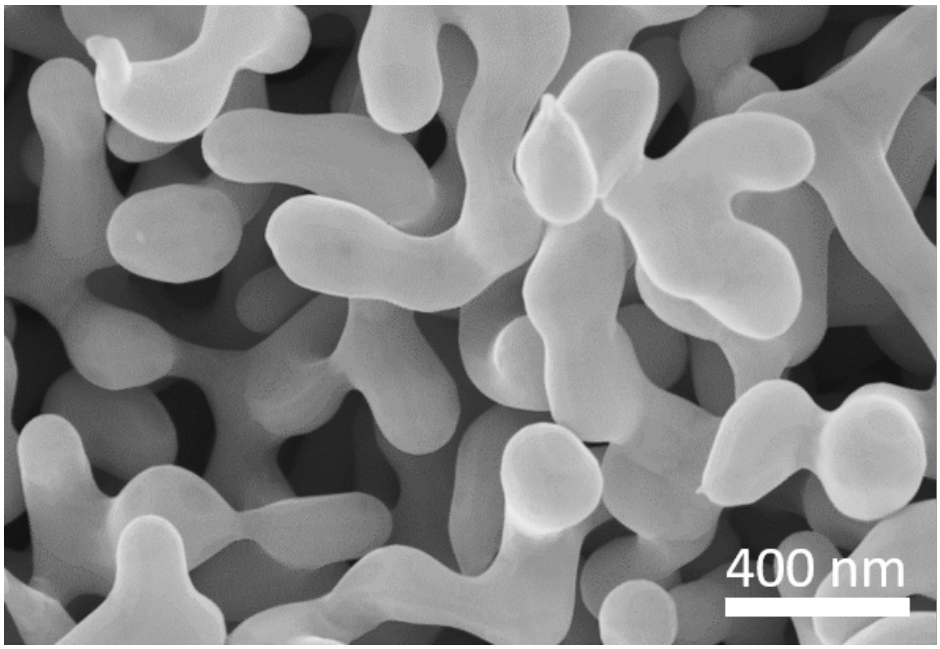

Figure 4.2. SEM picture showing the microstructure of the annealed NPG obtained by annealing at 300 °C for 30 min in the air. The mean ligaments diameter $L_D = 160 \pm 40$ nm.

4.2 Electrochemistry of NPG

4.2.1 Comparison of linear scan and staircase voltammetry

In this work, electrochemical characterizations and electrochemical control during *in situ* mechanical measurements were mainly carried out by means of cyclic voltammetry. As mentioned in section 3.2.2, linear scan voltammetry and staircase voltammetry work in different ways. It is, therefore, crucial to identify their performance with the mm-sized nanoporous samples so that a proper voltammetry is adopted in this work.

Figure 4.3 shows the current and charge responses of Au/PPy (section 3.3.4) subjected to the linear scan and staircase voltammetry in 0.1 M $HClO_4$. 20 nm-thick and 1200 nm-thick PPy films were deposited on the gold plates with the same surface area of 0.36 cm^2, which correspond to PPy volume of 7.22 × 10^{-4} mm^3 and 4.33 × 10^{-2} mm^3, respectively. In practice, 10 mV/s is the minimum scan rate that the potentiostat can apply in the linear scan voltammetry, yet, 2 mV/s is available in the staircase voltammetry. Figure 4.3a and Figure 4.3c show that the current, I, and charge, ΔQ, generated from 7.22 × 10^{-4} mm^3 PPy under the staircase voltammetry at 10 mV/s are much smaller than those under the linear scan voltammetry. However, when PPy volume increases to 4.33 × 10^{-2} mm^3, the current and charge responses under both linear scan and staircase voltammetry experiments at 10 mV/s do not show a big difference, as shown in Figure 4.3b and Figure 4.3d. For both Au/PPy(20 nm) and Au/PPy(1200 nm) bi-layers, when reducing the potential scan rate from 10 to 2 mV/s, the mean current values under the staircase voltammetry drastically decay by ~ 85% (Figure 4.3a and Figure 4.3b). However, as one can see in Figure 4.3c and Figure 4.3d, when reducing the scan rate from 10 to 2 mV/s, the corresponding ΔQ under the staircase voltammetry reduces only by 10% and 20% in Au/PPy(20 nm) and Au/PPy(1200 nm), respectively. As has been described in section 3.2.2, staircase voltammetry measures the Faradic current only and the charge obtained from staircase

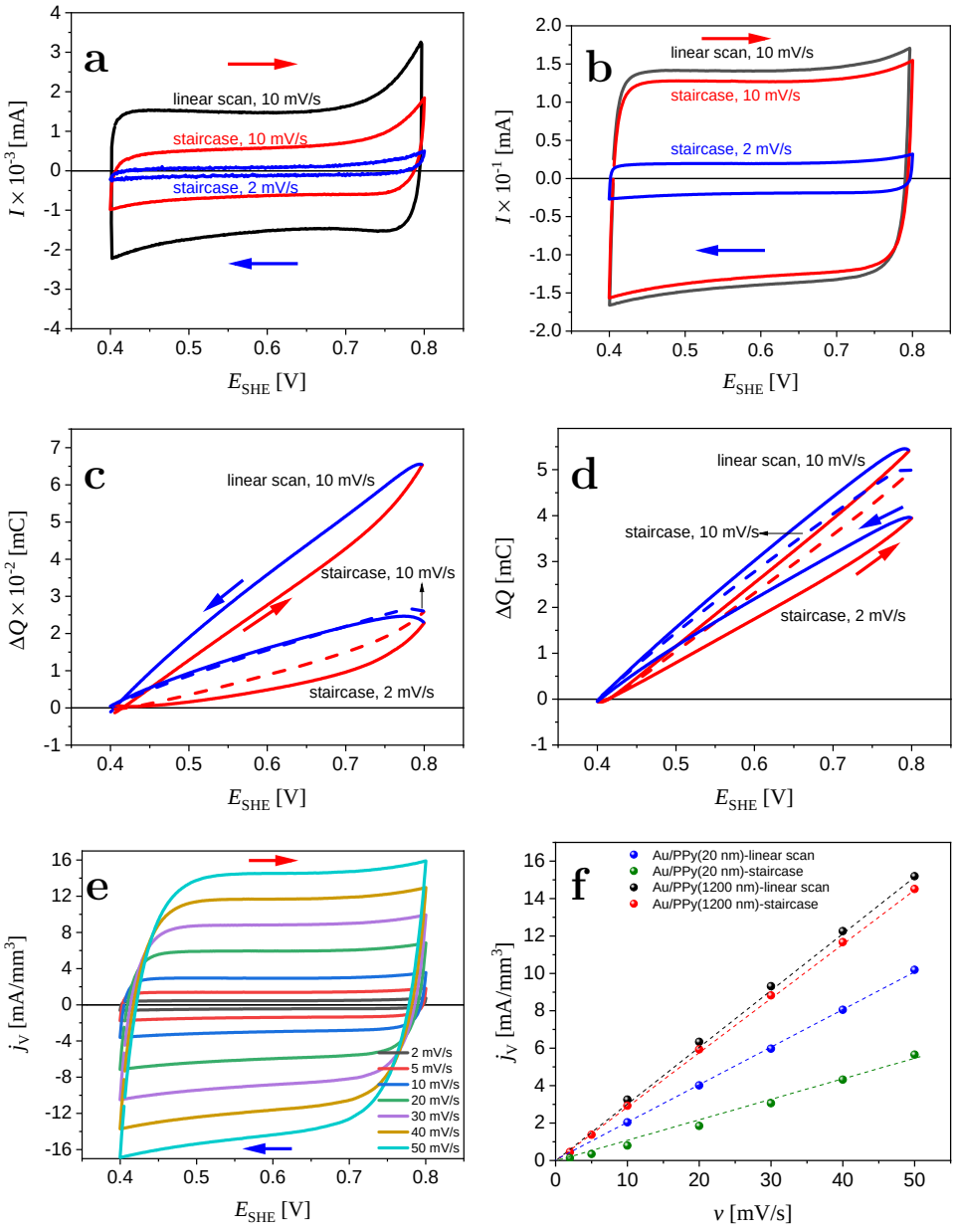

Figure 4.3. Electrochemical properties of Au/PPy with PPy thickness of 20 nm (a, c) and 1200 nm (b, d) in 0.1 M $HClO_4$ under different electrochemical conditions as marked in the figures. (a) and (b) display the current response, I, versus electrode potential, E_{SHE}. (c) and (d) present the charge, ΔQ, versus potential, E_{SHE}. (e) exhibits volumetric current density, j_V, of an exemplary Au/PPy(1200 nm) specimen versus potential, E_{SHE}, at scan rate, v, ranging from 2 to 50 mV/s. (f) plots the mean values of j_V as a function of v with the slopes of linear regressions (dashed lines), which pass through coordinate (0, 0), and present the volumetric capacitance, c_V. Red and blue arrows (in a - e) indicate the positive and negative sweep directions, respectively. Red and blue lines in (c) and (d) denote the anodic and cathodic branches. For the sake of distinction, ΔQ vs. E_{SHE} from staircase voltammetry at 10 mV/s are plotted as dashed lines (c, d).

voltammetry is underestimated in contrast to that obtained from linear scan voltammetry. Moreover, under staircase scan mode, a smaller scan rate of 2 mV/s allows more time for ClO_4^- to be incorporated into PPy matrix and the charge related to ClO_4^- diffusion predominates.

Figure 4.3e shows the cyclic voltammograms (CV) of a representative Au/PPy(1200 nm) specimen at various scan rates from 2 to 50 mV/s. The quasi-rectangular profiles are observed over the studied potential window, indicating that Au/PPy stores the charges in a pseudo-capacitive way [142, 172, 174, 175, 177, 212]. This is further confirmed by the linear current response dependency on the scan rate (as shown in Figure 4.3f). The slope of the linear regression gives the capacitance of the specimen. Au/PPy(1200 nm) with a PPy volume of 4.33×10^{-2} mm^3 exhibits a very similar volumetric capacitance, c_V, of 0.300 ± 0.003 and 0.290 ± 0.002 F/mm^3 under the linear scan and staircase voltammetry, respectively. For Au/PPy(20 nm) with PPy volume of 7.22×10^{-4} mm^3, however, a c_V of 0.110 ± 0.003 F/mm^3 was obtained under staircase voltammetry, which is only half of that (0.200 ± 0.002 F/mm^3) obtained under the linear scan voltammetry.

The current-potential and charge-potential results above indicate that the linear scan voltammetry works satisfactorily for Au/PPy hybrid with very a small PPy volume (~ 10^{-4} mm^3), whereas the staircase voltammetry is also applicable when PPy amount increases to ~ 10^{-2} mm^3. In this thesis, the amount of PPy in the mm-scaled NPG/PPy samples ranges from ~ 0.1×10^{-2} to ~ 3×10^{-1} mm^3. Moreover, equilibrium (or quasi-equilibrium) condition is available at a small scan rate, which can be realized in staircase voltammetry. Therefore, the staircase voltammetry was applied in this work.

4.2.2 Determination of the electrochemically active surface area of NPG

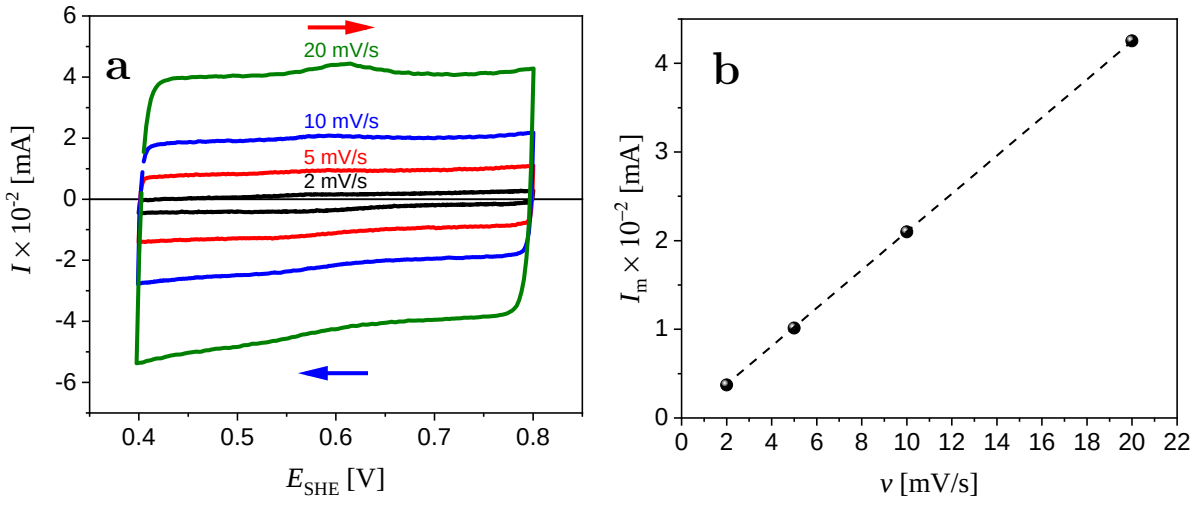

Figure 4.4. Capacitance determination by cyclic voltammetry (CV). (a) CV of the annealed NPG in 0.1 M $HClO_4$ at various scan rates, v. (b) Current in the middle of the potential range (at 0.6 V), I_m, as a function of scan rate, v. The dotted line shows the linear fit to the data. The red and blue arrows indicate the anodic and cathodic scan directions, respectively.

According to Eq. 3.2 (section 3.3.3), surface area, A, is an essential parameter to assess PPy thickness during electropolymerization process. As mentioned in sec-

tion 3.4.3, A can be obtained by the capacitance ratio method. Figure 4.4a shows the CV curves of NPG at various scan rates in the potential region where only double layer charging-discharging takes place. All CV curves exhibit rectangular shape, suggesting a pure capacitor behavior of NPG ligament-electrolyte interface. The current in the middle of the potential range (namely, at 0.6 V), I_m, is plotted versus scan rate, v, and a linear plot is obtained as shown in Figure 4.4b. According to Eq. 3.6, the slope of the linear plot gives the capacitance of ~ 2.2×10^{-3} F (~ 1.75×10^{-3} F/mm^3). By substituting $C^* = 20$ μF/cm^2 into Eq. 3.7, the surface area of an annealed NPG with a diameter of ~ 1 mm and length of ~ 1.6 mm is estimated to be ~ 110 cm^2. On the other hand, the surface area could also be estimated via Eq. 3.5. Taking the mean ligament characteristic size as $L_D = 150$ nm (section 4.1), NPG sample with a diameter of ~ 1 mm and length of 1.6 mm into consideration, the solid fraction of NPG ($\varphi = 0.3$), and the geometry constant $g = 4$, one also obtains the surface area of ~ 100 cm^2, which is very close to the value (110 cm^2) estimated through the capacitance ratio method.

4.3 Microstructure characterization of NPG/PPy

4.3.1 Microstructure characterization

The PPy coatings were electropolymerized on NPG specimens as described in section 3.3.3. According to Eq. 3.1 and Eq. 3.2, the PPy films with the desired thicknesses, t_{PPy}, can be achieved by monitoring the electropolymerization charge, Q. Figure 4.5 depicts the microstructure of the representative NPG/PPy compositions with various PPy film thicknesses, corresponding to the electropolymerization charge density, Q_A, from 2.12 to 12.29 mC/cm^2. It can be seen that for all NPG/PPy hybrids the original nanopores remain open, resulting in PPy with a high volume-specific surface area. The open network also favors an ion transport [213], and therefore facilitates the redox reactions during potential cycling. Figures 4.5e-g illustrate uniform PPy coatings with a thickness of 12 ± 2, 17 ± 2, 20 ± 2, 25 ± 3, and 36 ± 6 nm, which correspond to Q_A of 4.42, 6.03, 7.00, 7.73, and 12.29 mC/cm^2, respectively. Besides, as shown more clearly in Figure 4.5h (obtained under secondary electron mode), PPy film surface is composed of small nodular structures. Similar nodular features can also be expected in other PPy films. Irrespective of the surface conditions, the thicker PPy coatings are more visible on NPG ligaments as compared to the thin PPy coating synthesized at 2.12 mC/cm^2, as shown in Figure 4.5a. This thin PPy layer is observed at a higher magnification as shown in Figure 4.5b, whose thickness is ~ 6 ± 2 nm. In order to study the effect of PPy thickness on the mechanical properties, the PPy coatings with thickness < 6 nm were also synthesized.

4.3.2 Chemical composition analysis

Figure 4.6a shows the fracture surface of NPG/PPy with Q_A of 0.32 mC/cm^2 (NPG/PPy samples follow the same name convention in the following text). The smooth surface without cracks again confirms the reproducibility of the dealloying protocol and its applicability for mechanical testing. Figure 4.6b represents the microstructure of the central part of the specimen and displays a typical ligaments-pore network with PPy layer invisible at this scene. EDX analysis was performed within

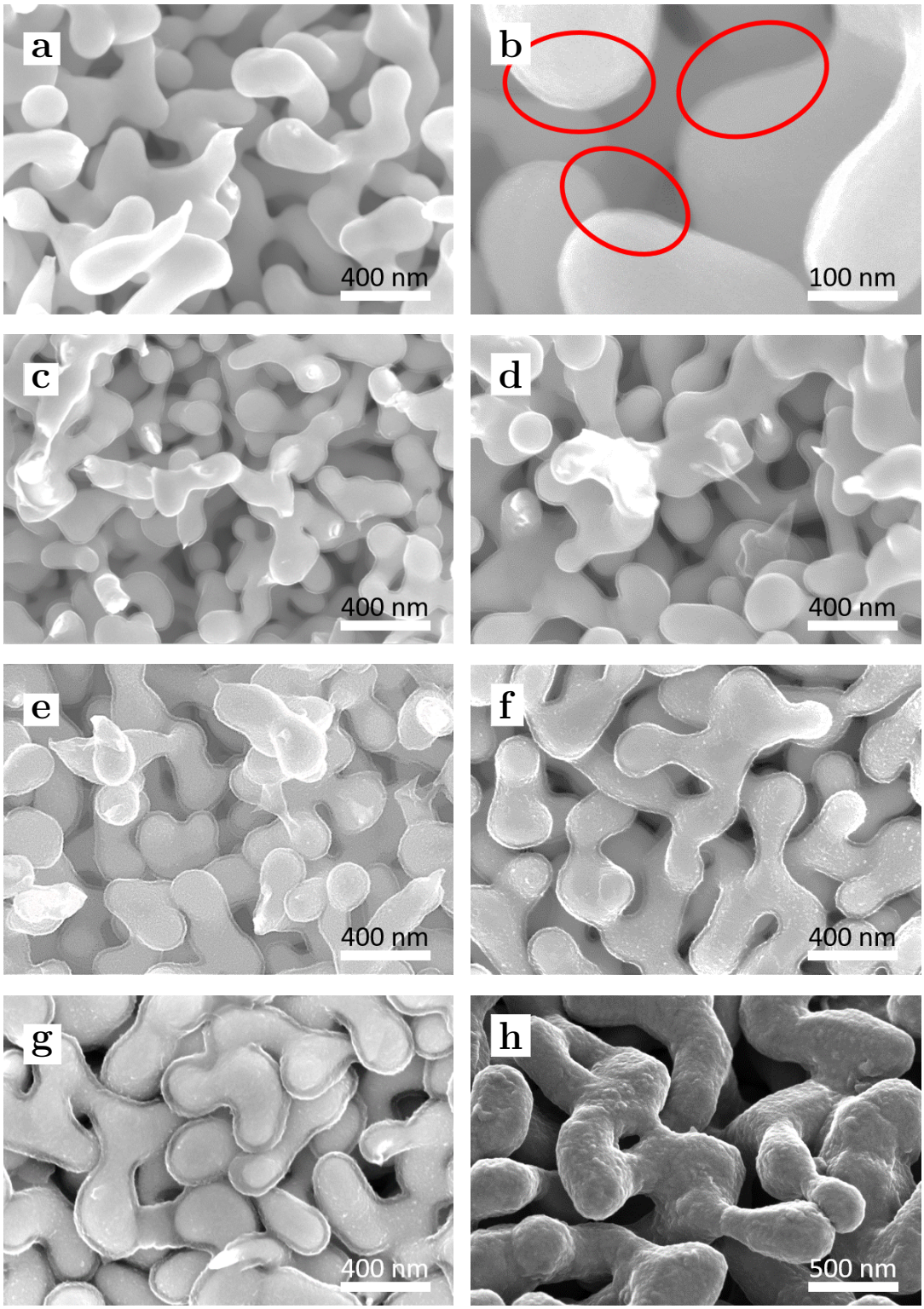

Figure 4.5. SEM images demonstrating microstructure of NPG/PPy with PPy thickness, t_{PPy}, of (a) 6 ± 2, (c) 12 ± 2, (d) 17 ± 2, (e) 20 ± 2, (f) 25 ± 3, and (g) 36 ± 6 nm, that corresponds to the electropolymerization charge density, Q_A, of 2.12, 4.42, 6.03, 7.00, 7.73, and 12.29 mC/cm^2, respectively. (b) SEM image showing microstructure in (a) at a higher magnification; red ellipses mark PPy layers on NPG ligaments. (h) SEM image obtained under secondary electron mode showing the surface morphology of the PPy in (g). Although the thin PPy layers in (a) and (b) are hardly recognized, the chemical composition analysis confirms the successful PPy electrodeposition on NPG ligaments as shown in Figure 4.6. All SEM pictures were taken from the fracture surfaces.

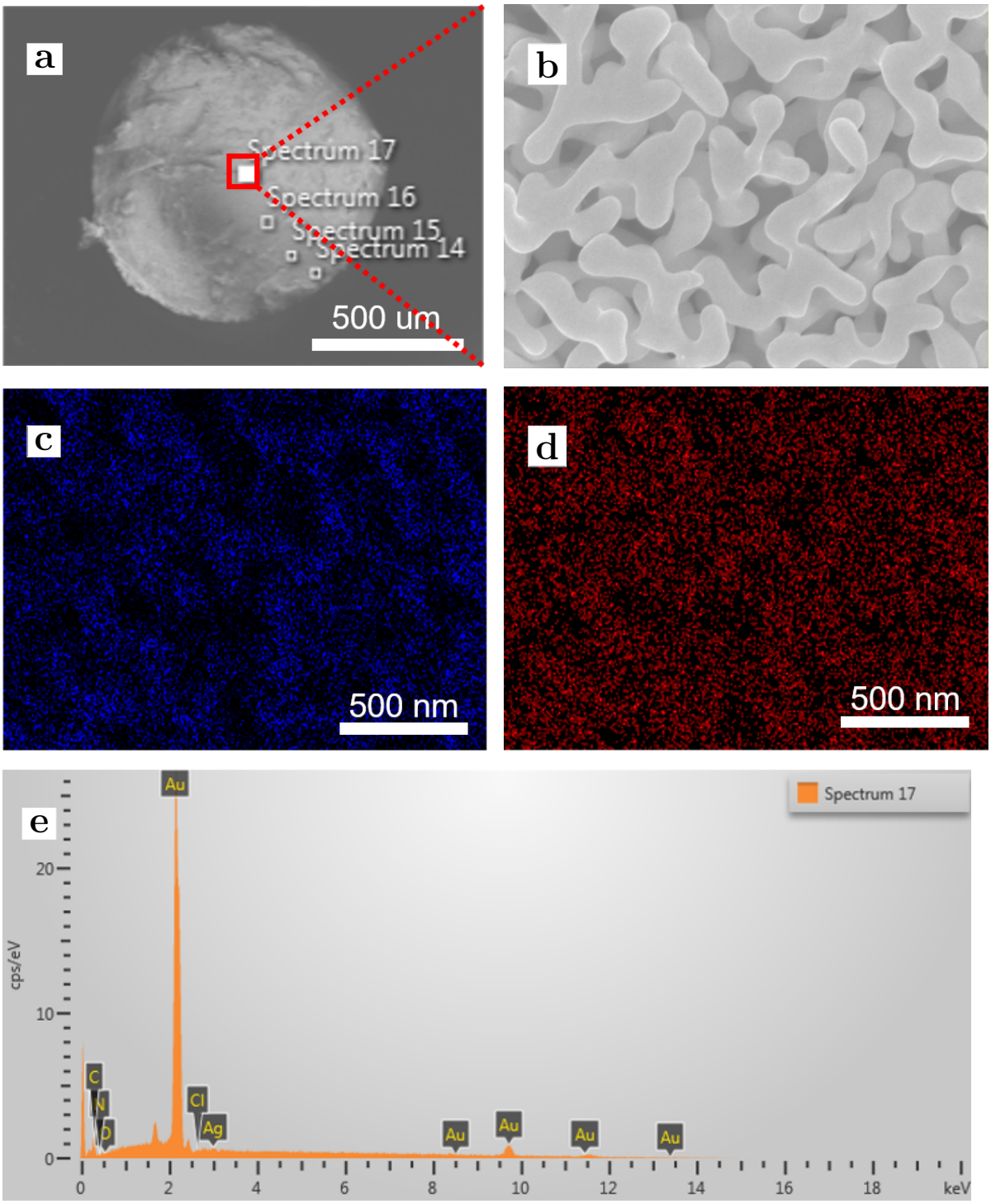

Figure 4.6. Characterization of microstructure and chemical composition of NPG/PPy. (a) SEM image showing the fracture surface of NPG/PPy with electropolymerization charge density $Q_A = 0.32$ mC/cm^2. (b) SEM image showing the magnified microstructure of the central part, marked by the red square in (a). EDX mapping of the whole area in (b) showing (c) carbon and (d) oxygen distributions. (e) EDX spectrum showing the chemical composition of the central part (as shown in a) of the sample.

the region displayed in 4.6b. The EDX spectrum (Figure 4.6e) demonstrates signals of nitrogen (N), carbon (C), chlorine (Cl), oxygen (O), gold (Au), and silver (Ag). Ag signal might come from the residual Ag in NPG ligaments or silver paste used to fix the sample. Because no other carbon source was introduced during the experiment, a heterocyclic aromatic ring (section 2.2.1 [132]) should be responsible for the appearance of C and N, confirming the successful electrodeposition of PPy. Cl and O approve the existence of dopant ClO_4^- that are incorporated during electropolymerization to maintain the charge neutrality. The element mappings of C and O in Figure 4.6c and Figure 4.6d also reveal a uniform distribution of C and O across the specimen, demonstrating a homogeneous PPy layer on the ligaments.

4.3.3 PPy thickness and volume fraction versus electropolymerization charge density

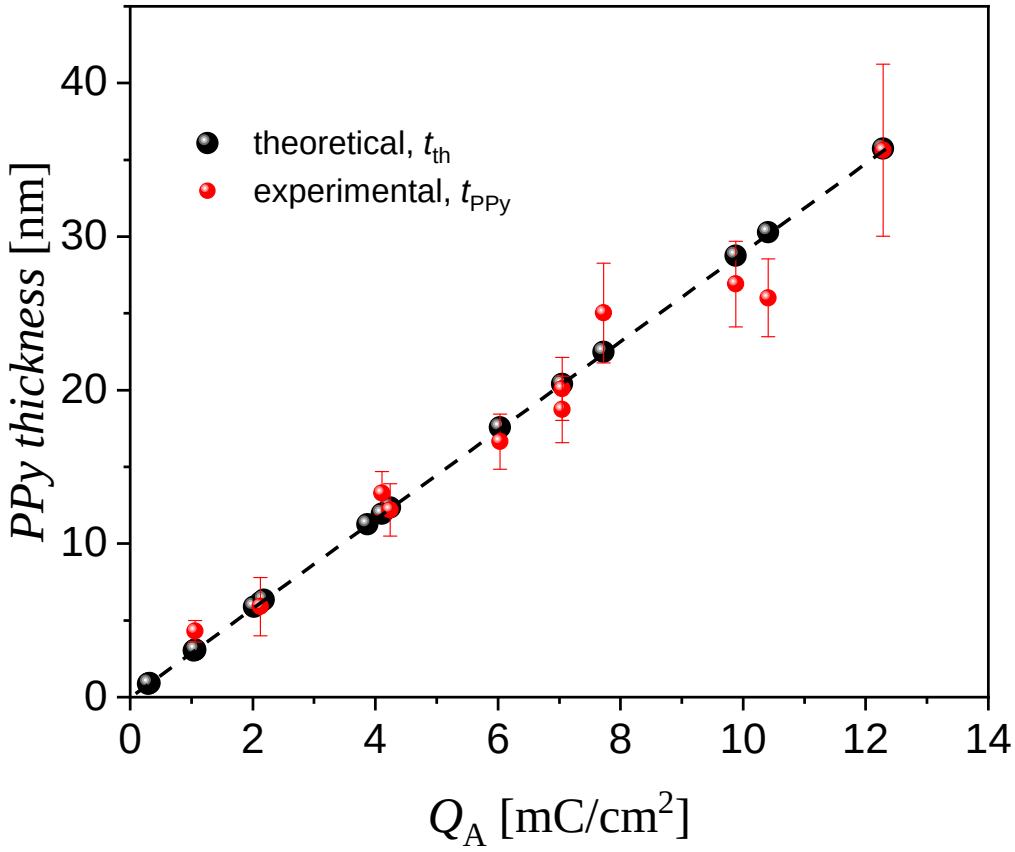

Figure 4.7. Theoretical (t_{th}) and experimental (t_{PPy}) PPy thickness with respect to the electropolymerization charge density, Q_A.

The experimental PPy film thicknesses, t_{PPy} (obtained from SEM images), as well as theoretical thickness, t_{th} (calculated as described in Eq. 3.1), are plotted versus the electropolymerization charge density, Q_A. As shown in Figure 4.7, t_{PPy} locates very close to the theoretical values. Both data sets are linear with Q_A with a slope of t_{PPy}/Q_A = 2.91 nm/(mC/cm^2). This value is in good agreement with that (2.5 nm/(mC/cm^2) [142, 214]) in literature. According to this relation, the thickness of PPy layer with Q_A = 3.2 C/cm^2 is ~1 nm, which is extremely thin and is difficult to be distinguished from NPG ligaments in SEM images. Although the thin PPy layers with thickness ≤

6 nm cannot be directly estimated from SEM, their effects on the electrochemical and mechanical responses on NPG is striking, as shown in sections 4.4 and 4.6.1.

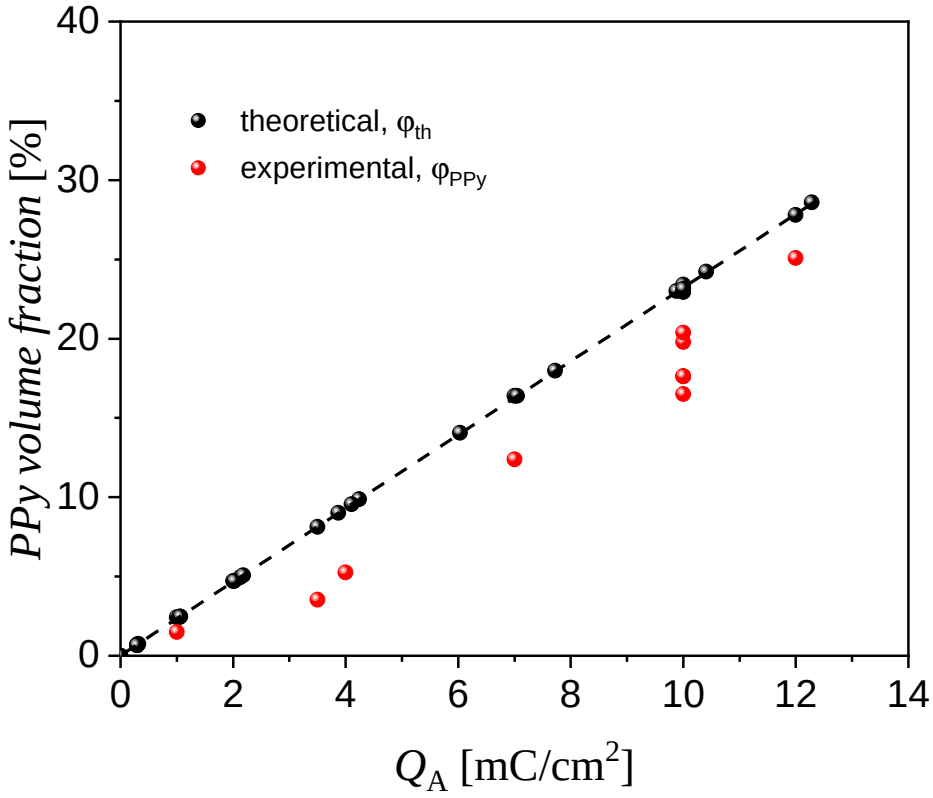

Figure 4.8. Theoretical (φ_{th}) and experimental (φ_{PPy}) PPy volume fraction with respect to the electropolymerization charge density, Q_A.

In addition to the thickness, PPy volume fraction is another parameter to quantify PPy in NPG/PPy. The theoretical PPy volume was obtained by dividing theoretical PPy mass over PPy density (section 3.3.3). On the other hand, actual PPy volume is obtained by dividing PPy mass, which is the mass difference of a specimen measured after and before electropolymerization, over PPy density. PPy volume fraction is obtained by dividing the theoretical and actual PPy mass over the sample volume. PPy volume fraction is plotted versus Q_A, as shown in Figure 4.8. The theoretical φ_{th} shows a linear behavior with respect to Q_A, with a slope of 0.023/(mC/cm²). The experimentally estimated φ_{PPy} values, however, are smaller than the theoretical values. This might originate from: 1) a measurement error since PPy mass is at the order of 10^{-4} ~ 10^{-5} g and 2) the loss of H_2O (in form of solvation shell around dopant and free water [7, 180, 187, 215]) incorporated during electropolymerization of PPy film. Therefore, the theoretical φ_{th} is applied in this work.

4.4 Electrochemical behavior of NPG/PPy

4.4.1 Determination of experimental potential window

Cyclic voltammetry (CV) was carried out to characterize the electrochemical behavior of mm-sized NPG/PPy samples with various PPy layer thicknesses. The CV measurements were first carried out in 0.1 M $HClO_4$ electrolyte at a potential window, E_{SHE},

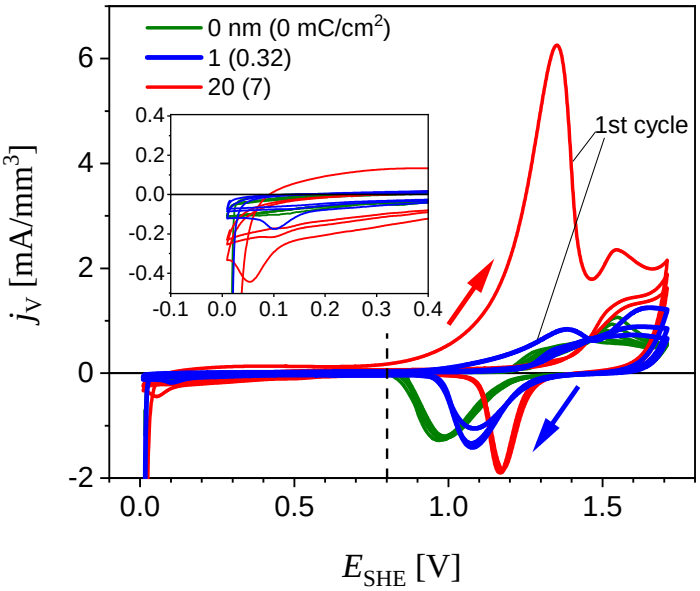

Figure 4.9. CV curves showing electrochemical behavior of the representative bare NPG, NPG/PPy(1 nm), and NPG/PPy(20 nm) specimens in a potential window of E_{SHE} between 0 and 1.7 V in 0.1 M $HClO_4$ at a scan rate of 5 mV/s. The inset figure plots the magnified CV curves in 0 ~ 0.4 V. The current density, j_V, denotes the current density normalized to the apparent volume of NPG/PPy samples. In the legend, the numbers in the brackets indicate the electropolymerization charge density, Q_A, and the numbers out of the brackets correspond to the theoretical PPy thickness, t_{th} (section 4.3). The red and blue arrows denote the anodic and cathodic potential scans, respectively. The dashed line at 0.8 V splits the potential window into two parts.

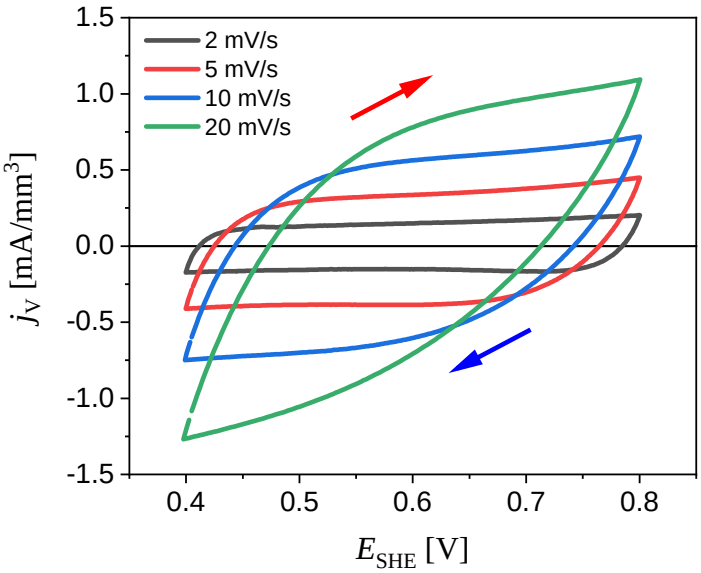

Figure 4.10. CV curves of NPG/PPy(35 nm) recorded in 0.1 M $HClO_4$ at a scan rate from 2 to 20 mV/s. The current density, j_V, was obtained by dividing the original current responses over the apparent volume of NPG/PPy(35 nm) specimen. Red and blue arrows indicate anodic and cathodic scan directions, respectively.

between 0 V and 1.7 V. The results are plotted in Figure 4.9. Obviously, the potential window can be separated into two parts: 1) a range of more negative potentials between 0 and 0.8 V, which is characterized by the small current and 2) the regime of more positive potentials between 0.8 V and 1.7 V, where a larger current and oxidation-reduction peaks are observed. For NPG, at the low potential range, the double layer charging-discharging occurs on the gold ligaments-electrolyte interface. As the potential increases, NPG is oxidized with the onset oxidation potential of ~ 1.2 V, which is in accordance with the literature results [29, 43]. During the successive redox cycling, gold surface reconstructs, resulting in the preferable formation of (111) or (100) facets coupled with the shift of the oxidation peak at ~ 1.5 V [216].

As far as NPG/PPy is concerned, when PPy is oxidized, the delocalized positive charges distribute on PPy chains and counterions (ClO_4^-) are incorporated to maintain the electric neutrality. During the 1st anodic scan, ClO_4^- anions are absorbed into PPy matrix at 0 ~ 0.8 V. However, the currents of both NPG/PPy(1 nm) and NPG/PPy(20 nm) start to increase drastically at ~ 0.9 V and a high peak appears at ~ 1.35 V. This peak observed at the 1st CV cycle disappears in the subsequent scans, where the anodic current exhibits similar profiles and amplitudes to those of NPG. The much smaller current values imply over-oxidation and degradation of PPy at the high potentials. Moreover, in comparison to the current of bare NPG, the relatively larger current magnitudes at 1 ~ 1.4 V in the 1st and in the following cycles also indicate the successful deposition of an extremely thin PPy layer of ~ 1 nm. The inset figure demonstrates the current response at a potential range of 0 ~ 0.4 V. The current under zero and small reduction peaks (accompanied by the appearance of bubbling on WE during the experiments) seen in CV curves of NPG/PPy specimens are not desired. Therefore, a potential window between 0.4 V and 0.8 V was selected in this work. Under this condition, oxidation of NPG, over-oxidation of PPy, and parasitic reactions in the electrolyte are avoided. In sections 4.2.1 and 4.2.2, the electrochemical behavior of NPG and Au/PPy bi-layers between 0.4 V and 0.8 V is reported. The electrochemical properties of NPG/PPy at the same conditions are investigated below.

4.4.2 Effect of scan rate

Figure 4.10 displays typical CV curves of a NPG/PPy(35 nm) specimen recorded between 0.4 V and 0.8 V at a scan rate of 2 ~ 20 mV/s in 0.1 M $HClO_4$. The voltammograms exhibit quasi-rectangular profiles at low scan rates ranging from 2 to 10 mV/s. There are no evident redox peaks observed in the whole potential range, suggesting that the electrode is charged and discharged in a pseudo-capacitive way over the whole CV. At a higher scan rate of 20 mV/s, the CV curve deviates from the rectangular shape. As compared to the quasi-rectangular shape obtained at a scan rate of 50 mV/s (as shown in Figure 4.3e) for the planar Au/PPy(1200 nm) bi-layer, this deviation might arise from the limited ion diffusion rate in porous structure [173, 212].

4.4.3 Effect of PPy thickness

Figure 4.11a exhibits the current responses of NPG/PPy specimens with different thicknesses which correspond to various electropolymerization charge densities, Q_A. The CV curves with quasi-rectangular profiles are obtained, suggesting the pseudo-capacitive charging-discharging mechanism of oxidizing and reducing the NPG/PPy

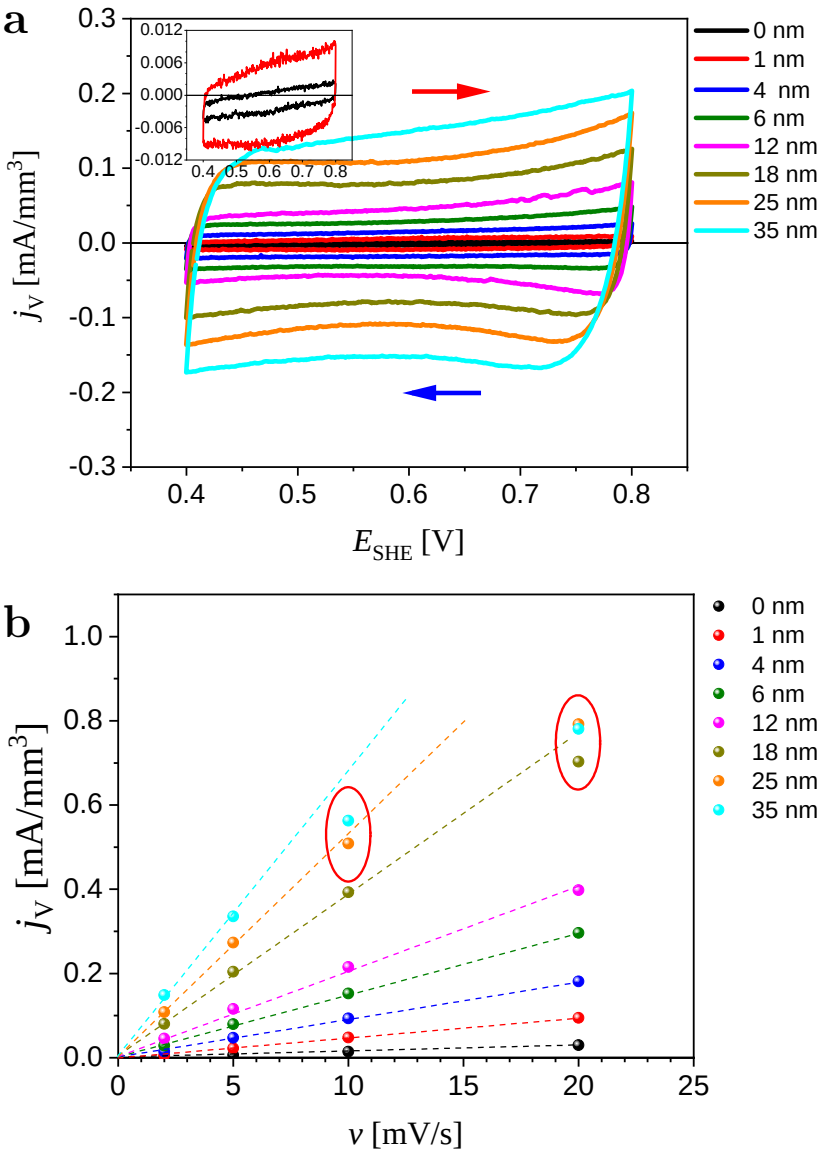

Figure 4.11. Electrochemical behavior of NPG/PPy with various PPy thickness. (a) CV curves of NPG/PPy with various thicknesses at a scan rate of 2 mV/s between 0.4 and 0.8 V in 0.1 M $HClO_4$. The inset figure plots the CV curves of NPG ($t_{PPy} = 0$ nm, black line) and NPG/PPy(1 nm, red line) at a higher magnification. (b) Mean values of current density, j_V, versus scan rates, v. Dashed lines: Linear regressions with the slopes providing the volumetric capacitance, c_V. Symbols with different colors denote specimens with different PPy thickness synthesized at various electropolymerization charge densities, Q_A. Some symbols overlap and do not fall on the linear regressions, as marked in red ellipses. Current density, j_V, refers to the current normalized to the apparent volume of NPG/PPy samples. Red and blue arrows indicate anodic and cathodic scan direction, respectively.

hybrids. Moreover, the current density, j_V, increases with PPy thickness (or Q_A), implying that the charges are stored in a pseudo-capacitive way, and the thicker the PPy layer, the more charges are stored. The inset figure in Figure 4.11a shows the CV of bare NPG and NPG/PPy(1 nm) with PPy theoretical thickness of 1 nm. Both NPG and NPG/PPy(1 nm) display rectangular CV curves with distortion which might arise from the internal resistances, including the electrical resistivity of the material, the resistance to ionic transport in the electrolyte and in the porous electrode [173, 217]. More importantly, NPG/PPy(1 nm) exhibits a higher j_V than NPG, further supporting the successful deposition of the extremely thin PPy coating on Au ligaments.

The mean magnitudes of j_V of NPG/PPy with different PPy thickness are obtained and plotted versus scan rate, v, as shown in Figure 4.11b. One can see that when PPy thickness is less than 12 nm, j_V increases linearly with v at all scan rates from 2 to 20 mV/s. However, while increasing PPy thickness up to 35 nm, j_V shows the linear behavior only within a limited range of v, up to 5 mV/s (t_{PPy} >25 nm) or 10 mV/s ($t_{PPy} \simeq$ 18 nm). Beyond the critical v, the j_V deviates from the corresponding linear regressions, as marked by the ellipses in the plot. However, this deviation is not seen in Au/PPy(1200 nm) bi-layer which shows a perfect linear current dependency on the scan rate up to 50 mV/s (Figure 4.3f). The restrained j_V of NPG/PPy at the high scan rates might be explained as follows: First, the diffusion coefficient, D_s, of ClO_4^- in PPy matrix is small (~ 10^{-13} m^2/s [218]). Also, the bicontinuous nanopores of NPG/PPy increase the pathway for ClO_4^- to diffuse throughout the mm-scaled specimen. The thicker the PPy layer, the narrower the nanopores, and that is why the maximum v for NPG/PPy(35 nm) and NPG/PPy(25 nm) is 5 mV/s, whereas that for NPG/PPy(18 nm) is 10 mV/s. Second, at higher scan rates, the time interval is small and insufficient to incorporate ClO_4^- into PPy matrix. On the contrary, scanning at $v \leq$ 5 mV/s for NPG/PPy($\geq$ 18 nm) and 2 ~ 20 mV/s for NPG/PPy($\leq$ 12 nm) achieve charge equilibrium and is not affected by the transport limitations. Under the equilibrium condition, the transferred charge reflects the capacitance of the PPy, with the slope (linear regression) of j_V - v representing the volumetric capacitance, c_V. c_V is plotted as a function of t_{PPy}, as shown in Figure 4.12. It can be seen that the volumetric capacitance increases with PPy thickness, indicating pseudo-capacitive charging in PPy matrix. This finding is in accordance with the literature [29, 142].

4.5 Mechanical behavior under compression in the air

Prior to studying the mechanical properties under *in situ* electrochemical conditions, the stress-strain behaviors of dry NPG/PPy samples were investigated in the air. Figure 4.13a shows the load-unload stress-strain responses of the representative NPG/PPy specimens with ligament size, L_D, ~ 150 nm and PPy thickness, t_{PPy}, varying from 0 (bare NPG) to 30 nm. The initial portion of the load-unload curve is magnified and presented in Figure 4.13b. Obviously, NPG shows a low strength, not exceeding 4 MPa up to a 7% deformation. Under compression, NPG undergoes plastic deformation even at the lowest strain, without a distinguished yield point. As the compression proceeds, NPG shows good ductility and it can be deformed to a strain up to 60% without breaking (as shown in Figure 4.13a).

When NPG ligaments are covered by PPy layer, the macroscopic strength is en-

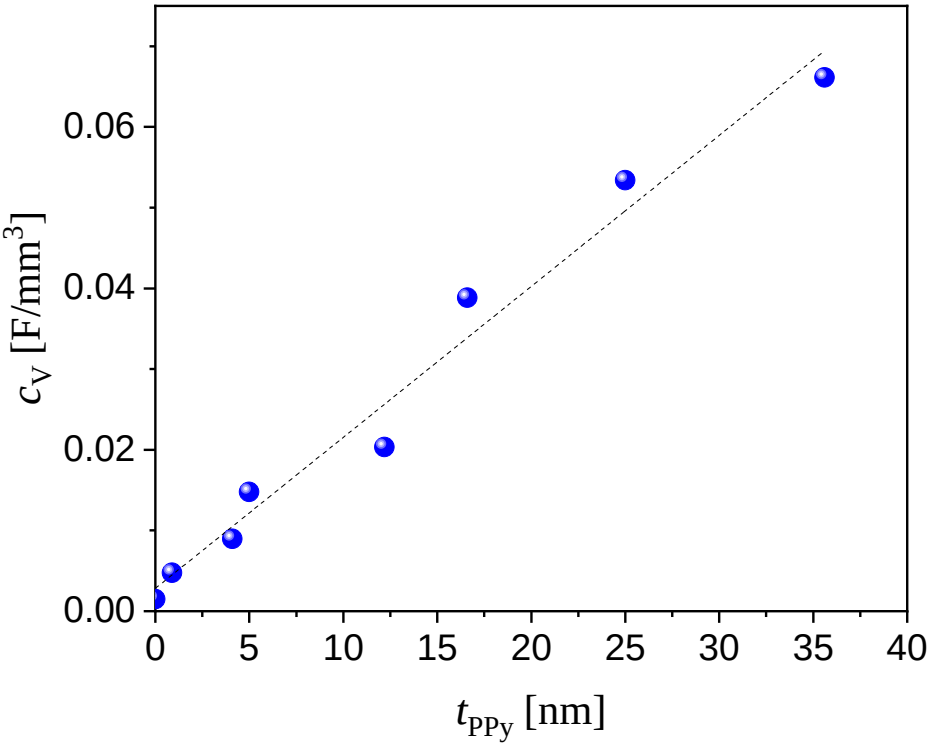

Figure 4.12. Volumetric capacitance, c_V, versus PPy layer thickness, t_{PPy}. Dashed line shows a linear c_V dependence on the scan rate, v.

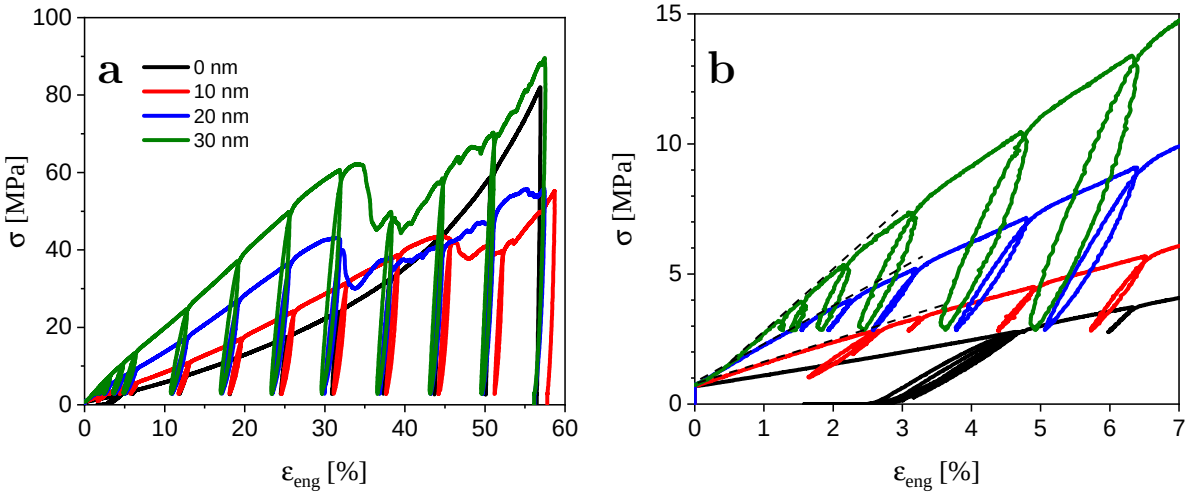

Figure 4.13. Stress-strain curves of NPG/PPy obtained from load-unload experiments in the air with a strain rate of 10^{-4} s^{-1}. (b) Magnified load-unload stress-strain curves up to a deformation of 7%. All NPG/PPy samples have the same ligament size L_D ~ 150 nm but different PPy layer thickness, t_{PPy}, ranging from 0 (bare NPG) to 30 nm. σ and ε_{eng} indicate macroscopic stress and engineering strain, respectively. Dashed lines in (b) indicate the apparent initial linearity of σ vs. ε_{eng}.

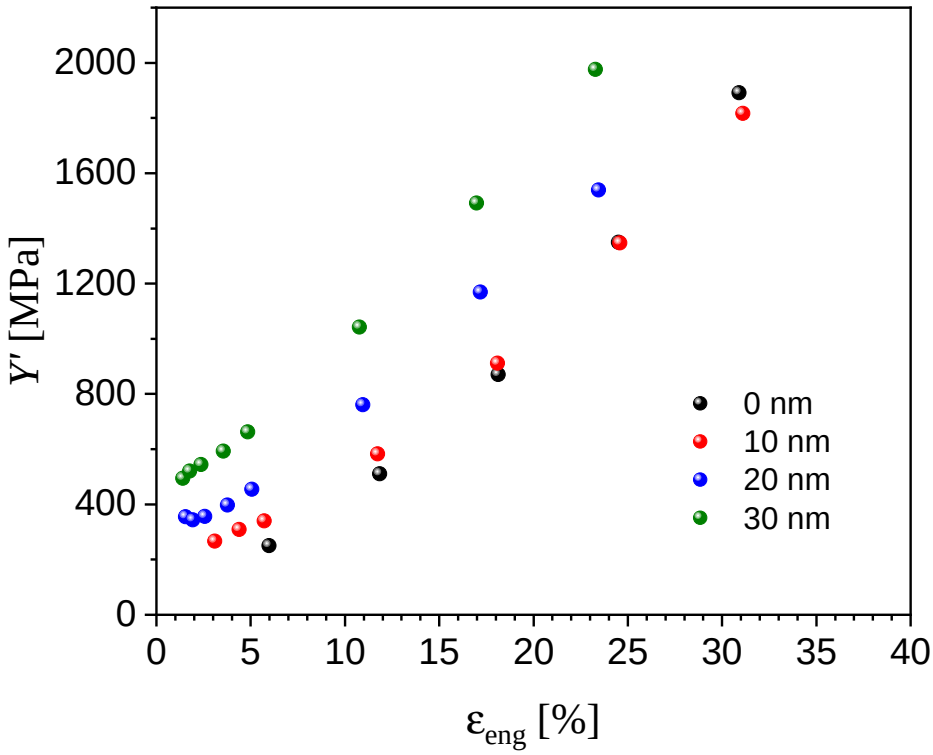

Figure 4.14. The effective Young's modulus, Y', as a function of engineering strain, ε_{eng}. Y' values were determined from the load-unload loops in the load-unload stress-strain curves of NPG/PPy with t_{PPy} ranging from 0 to 30 nm.

hanced, and the thicker the PPy layer, the higher the strength of the NPG/PPy hybrid, as shown in Figure 4.13b. NPG/PPy(10, 20 nm) specimens exhibit an apparently linear elastic regime below a 2% strain, as marked by the dashed lines. However, the early compression curve of NPG/PPy(30 nm) deviates from the linear portion of the fit. This might stem from the unplanar sample surfaces or the ill-suited contact between the sample and the compression grips. Regardless of the early plasticity in NPG/PPy(30 nm), the deviation of the stress-strain curves from the linear regressions at a strain around 2% suggests the yielding of NPG/PPy specimens (t_{PPy} = 10 ~ 30 nm). When compression continues, however, NPG/PPy specimens exhibit failure at a 30% ~ 40% deformation, as shown in Figure 4.13a.

The load-unload stress-strain curves allow identifying the elastic moduli under various deformation states in a single experiment. Based on the load-unload segments in the load-unload stress-strain curves, the effective Young's modulus, Y', was evaluated as described in section 3.5.2.2. Figure 4.14 plots the Y' values as a function of engineering strain, ε_{eng}. It can be seen that NPG exhibits Y' of ~ 250 MPa at ε_{eng} = 6%, which agrees well with the data reported in Ref. [210], in which L_{D} = 150 nm.

As compared to bare NPG, larger Y' values are found for NPG/PPy hybrids even at a smaller strain. Although Y' (~ 260 MPa at ε_{eng}= 3%) of NPG/PPy(10 nm) is slightly bigger than that (250 MPa at ε_{eng}= 6%) of NPG, Y' increases with PPy layer thickness (Figure 4.14). Y' values around 350 MPa and 500 MPa are obtained for NPG/PPy(20 nm) and NPG/PPy(30 nm) at ε_{eng} = 1.5%, respectively. These observations, although preliminary, demonstrate the enhancement effect of PPy coatings on the elastic behavior of NPG.

4.6 Elastic behavior of NPG/PPy

4.6.1 Impact of PPy thickness

4.6.1.1 Dynamic mechanical analysis during potential cycling

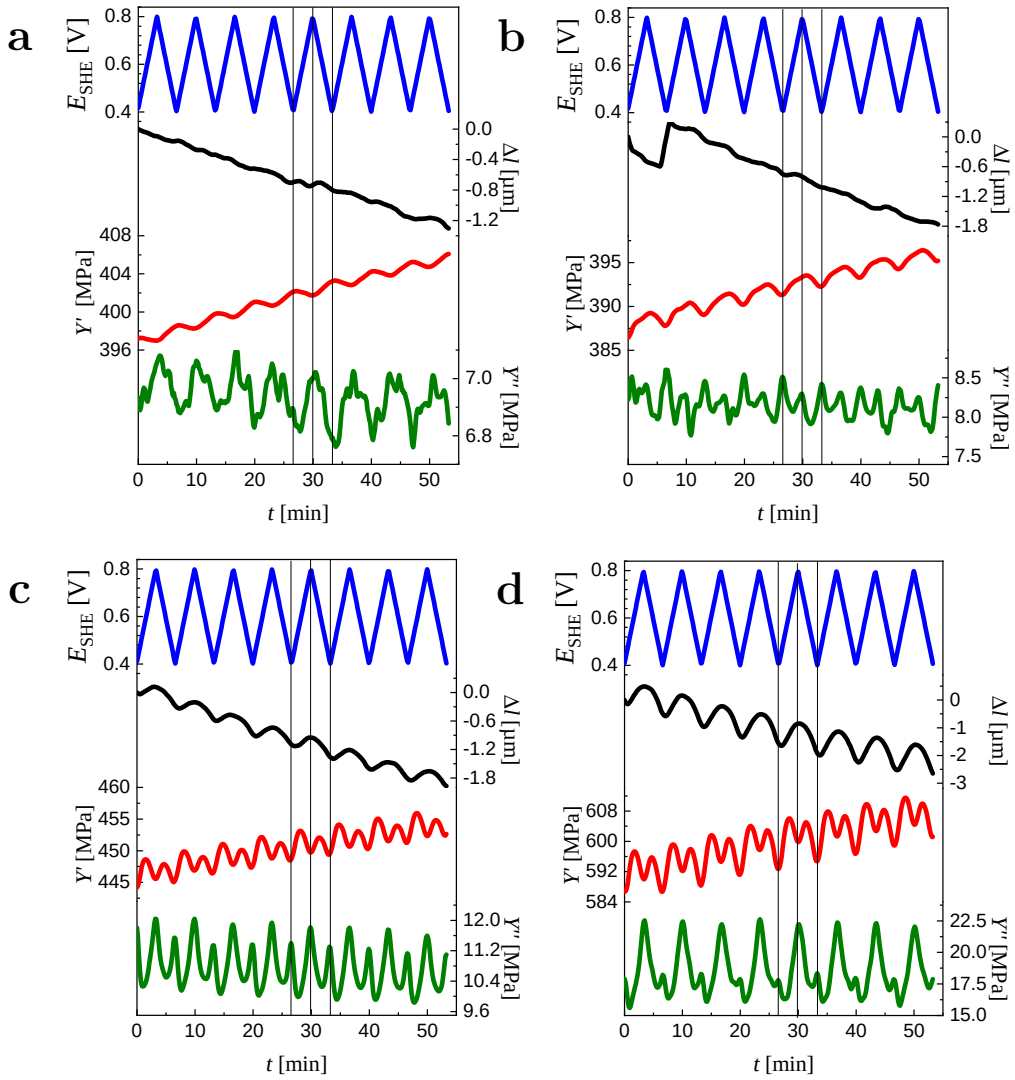

Figure 4.15. Exemplary mechanical responses of NPG and NPG/PPy hybrids measured during *in situ* DMA experiments in 0.1 M $HClO_4$ at a scan rate of 2 mV/s with compressive static stress, maximum dynamic stress, and dynamic stress frequency of ~ 5.02 MPa, ~ 0.64 MPa, and 1 Hz, respectively. Viscoelastic behavior of NPG/PPy with t_{PPy} of (a) 0 nm, (b) 1 nm, (c) 6 nm, and (d) 35 nm during potential sweeps are plotted versus time, t. Blue line and upper left ordinate: Variation of E_{SHE} with t; black line and upper right ordinate: Macroscopic length change, Δl; red line and lower left ordinate: Storage (effective) modulus, Y'; green line and lower right ordinate: Loss modulus, Y''.

The dynamic viscoelastic behaviors of bare NPG and NPG/PPy hybrids were inspected by a dynamic mechanical analyzer (DMA) *in situ* during the potential cycling (section 3.5.3). The NPG and NPG/PPy specimens, working as WE, were placed in the DMA electrochemical cell filled with 0.1 M $HClO_4$, as shown in Figure 3.11b.

The oxidation states of PPy were controlled by tuning the potential and the resulted changes in storage, Y', and loss, Y'', moduli as well as the macroscopic length change, Δl, were simultaneously detected. The frequency of the oscillating force was 1 Hz, whereas the frequency of the cycling electrode potential was 0.0025 Hz for a scan rate of 2 mV/s. In this way, the force oscillated within a constant potential period.

Figure 4.15 plots the response of the length change, Δl, the effective storage modulus, Y', as well as loss modulus, Y'', versus time, t, during eight successive potential sweeps, E_{SHE}. In the case of bare NPG, an appropriately linear behavior of Y' with E_{SHE} was found (Figures 4.15a and 4.16a). NPG softens upon positive charging and stiffens upon negative one. This agrees well with the previous observations in Ref. [21], although reported for NPG with a smaller ligament size. So far, the electrochemically modulated changes in the effective elastic modulus of NPG are attributed to the local stiffness variations at the metal surface upon positive (electron depletion) or negative (electron accumulation) charging. By contrast, Y'' response appears quite complex and shows an opposite trend to Y' - E_{SHE} behavior in all CV cycles. Y'' tends to increase along with potential until the upper vertex potential, followed by the decrease until the lower vertex potential. The fluctuations in Y'' might be due to the dissipation processes at the gold surface [21, 219, 220], involving the adatom rearrangements induced by the potential modulation. For the relatively larger ligaments in this work, these processes might subside and cannot be well recognized under the oscillating conditions applied. Irrespective of Y'' variations during potential scanning, the significantly smaller values of Y'' as compared to Y' in the whole potential range indicate that NPG behaves in a nearly ideal elastic way (section 3.5.3).

As shown in Figure 4.15a, DMA also fails to detect any definite variations of the macroscopic length of NPG specimen. Since the actuation of a nanoporous metal relies on the surface stress variations, a relatively small surface area in this work diminishes the effect [84]. Consequently, the NPG length variation is not identified by the DMA. Besides, a continuous decrease of Δl is observed, implying a gradual densification of the NPG specimen during the measurement. This goes along with the continuous stiffening, which is superimposed on the reversible Y' variations.

The viscoelastic response of NPG is drastically influenced by PPy coating, even with the thinnest polymer with a thickness of 1 nm, as shown in Figure 4.15b. It can be seen that within a CV cycle, the corresponding Y' behaves oppositely as compared to that of bare NPG (Figure 4.16j). When the electrode potential sweeps to more positive values, Y' ascends, whereas Y' descends when the potential scans back. Y'', however, exhibits a complex non-linear behavior with the potential. The results of the modulus response indicate that PPy coating plays a critical role in the mechanical behavior of NPG/PPy hybrids. The length variation of NPG/PPy(1 nm), however, is not well recognized (Figure 4.16n).

When a thicker PPy layer with $t_{\mathrm{PPy}} = 6$ nm is coated on NPG ligaments, more pronounced variations of the length and viscoelastic properties are observed (Figure 4.15c). The DMA reveals well-defined Δl variations. The hybrid material reversibly expands and shrinks as a function of E_{SHE}. However, contrary to the continuous softening of NPG (or continuous stiffening of NPG/PPy(1 nm)) upon anodic sweep, Y' behavior of NPG/PPy(6 nm) is non-monotonous. Y' shows a sharp increase up to 0.55 V followed by a decrease up to 0.8 V (Figure 4.16c). During the cathodic sweep, the Y' behavior is inverted. Y'' shows an opposite trend to Y' during potential scanning. It should be noted that the Y'' signal of NPG/PPy(6 nm) is much more stable than those of NPG

and NPG/PPy(1 nm) with the enhanced values.

When PPy thickness further increases to 35 nm, the essential characteristics of the appropriately linear macroscopic length variation and the non-linear viscoelastic behavior observed in NPG/PPy(6 nm) are preserved, albeit, with an enlarged amplitude of length change, Δl, effective modulus, Y', and loss modulus, Y'' (Figures 4.15d and 4.16d and p). The enhanced amplitudes of the properties suggest a prominent contribution of PPy layer to the mechanical response.

For both NPG/PPy(6 nm) and NPG/PPy(35 nm) hybrids, a downward drift of Δl and an upward drift of Y' and Y'' are observed, similar to bare NPG and NPG/PPy(1 nm). This phenomenon also implies the plastic deformation in NPG/PPy specimens with the thicker PPy layer. Overall, the cyclic variations of Δl, Y', and Y'' with the electrode potential, E_{SHE}, are well distinguished, indicating that densification does not affect the tunability of the mechanical properties.

Similar mechanical behaviors are also observed during *in situ* DMA measurements on NPG/PPy with t_{PPy} of ~4 nm, as well as of ~ 12 nm - ~ 26 nm. Overall, the mechanical behaviors over eight successive CV cycles demonstrate an excellent chemical and mechanical stability of all NPG/PPy(0 ~ 35 nm) hybrids.

4.6.1.2 Electro-chemo-mechanical coupling

The electro-chemo-mechanical coupling of NPG/PPy hybrids is further studied by plotting the effective Young's modulus variation, $\Delta Y'$, actuation strain, ε, versus electrode potential, E_{SHE}, or net volumetric charge density, Δq_{V}, at a single CV cycle as shown in Figure 4.16. Figures 4.16a, e, i, and m show the corresponding curves for bare NPG. In accordance with previous findings [21, 50], $\Delta Y'$ and ε of NPG exhibit linear dependence on E_{SHE} and Δq_{V} upon capacitive charging in the electrolyte (Figures 4.16a, e, i, and m). NPG expands and shrinks with a mean peak-to-peak strain amplitude of ~ 0.004% (Figure 4.16m) as well as softens and stiffens with the elastic modulus variation amplitude of ~ 0.9 MPa (Figure 4.16a). The relatively smaller magnitudes of ε and $\Delta Y'$ in this work are expected because of the four times larger ligament size (160 nm versus 40 nm in the Ref. [21]), and as a consequence, the reduced specific surface area of NPG.

In the case of NPG/PPy hybrids, larger Δq_{V} are transferred upon charging PPy, with Δq_{V} amplitude increasing with PPy thickness (Figures 4.16f, g, and h). Similar to the linear Δq_{V} - E_{SHE} relationship of the bare NPG, Δq_{V} of NPG/PPy also linearly scales with E_{SHE}.

Figures 4.16o and p illustrate reversible expansion and contraction of NPG/PPy hybrids versus the transferred charge Δq_{V} for the thicker PPy coating ($t_{\mathrm{PPy}} > 6$ nm). NPG/PPy(1 nm), however, shows non-linear ε as a function of Δq_{V}. In this case, PPy has an extremely small thickness of 1 nm, which is too thin to accommodate a large amount of the ClO_4^- (with a radius of 0.29 nm [180]) during charging-discharging process.

The most striking phenomenon is the non-monotonous dependence of $\Delta Y'$ on E_{SHE} and Δq_{V} (Figures 4.16b, c, d, j, k, and l) in contrast to the linear ε - Δq_{V} relationship. For NPG/PPy(1 nm), a gradual $\Delta Y'$ increase is observed upon positive scanning. $\Delta Y'$ - E_{SHE} curve shows a reflection point at ~ 0.6 V. Then, $\Delta Y'$ between 0.6 and 0.8 V increases at a lower rate (a smaller $\Delta Y'$ - E_{SHE} slope), as shown in Figure 4.16b. The cathodic scan shows a nearly linear $\Delta Y'$ decrease as a function of E_{SHE}. The $\Delta Y'$ - E_{SHE} curve during anodic and cathodic scans at the lower potential window (0.4 ~ 0.6 V)

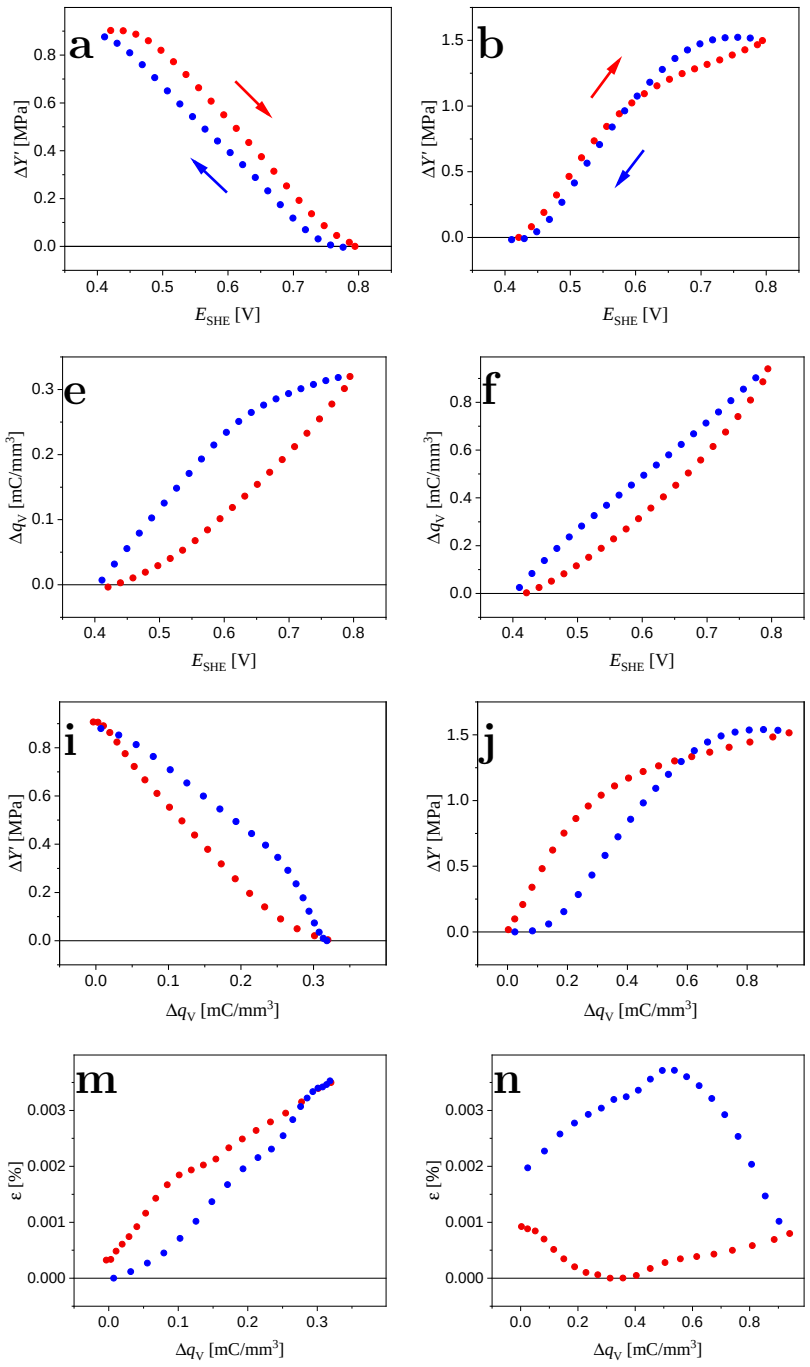
a
b
e
f
i
j
m
n
ΔY' [MPa]
E_SHE [V]
Δq_V [mC/mm³]
ε [%]

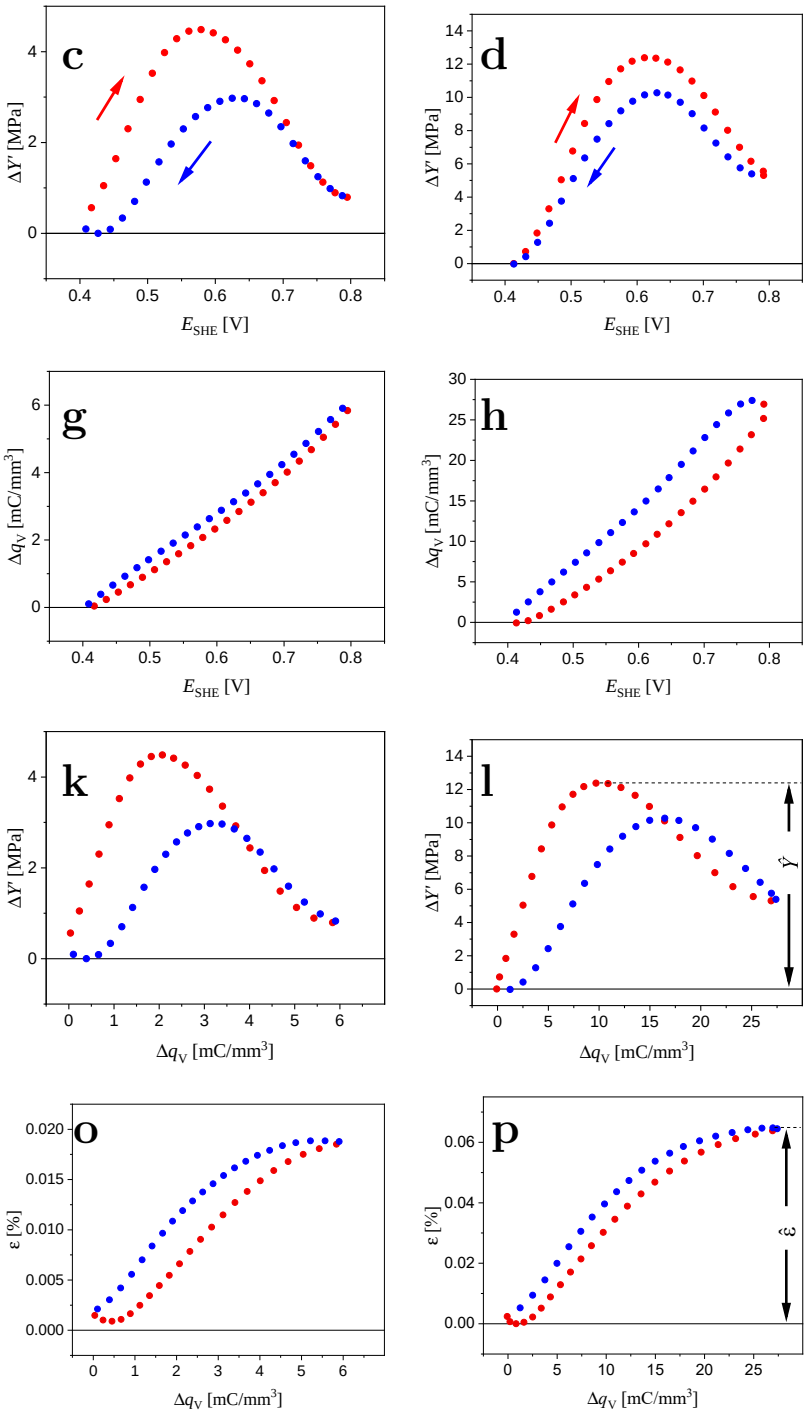

Figure 4.16. The electro-chemo-mechanical coupling of NPG/PPy with t_{PPy} of 0 nm (left column, on the previous page), 1 nm (2nd column, on the previous page)), 6nm (3rd column), and 35 nm (4th column) The *in situ* DMA experiments were performed in 0.1 M $HClO_4$ at a scan rate of 2 mV/s with compressive static stress, maximum dynamic stress, and dynamic stress frequency of ~ 5.02 MPa, ~ 0.64 MPa, and 1 Hz, respectively. $\Delta Y'$, the effective modulus variations; E_{SHE}, electrode potential; Δq_{V}, the total transferred charge per specimen volume; ε, the actuation strain (relative length change) of the specimen. Red and blue arrows and dotted lines demonstrate anodic and cathodic sweeps, respectively. The data were averaged over three successive CV cycles, separately for positive and negative-going sweeps. $\hat{Y}$ in (l) and $\hat{\varepsilon}$ in (p) indicate the peak-to-peak amplitudes of effective modulus variation and actuation strain, respectively.

superimposes. When PPy thickness increases, a different $\Delta Y'$ - E_{SHE} relationship is observed. From Figures 4.16c and d, it is clear that during the anodic scan $\Delta Y'$ increases until ~ 0.6 V, followed by the decrease until the end of the potential range. During the backward cathodic scan, an opposite trend in $\Delta Y'$ behavior is observed. In addition, the amplitude of $\Delta Y'$ during the cathodic scan is smaller than that of the anodic scan. Therefore, the stiffening-softening response of $\Delta Y'$ during the cathodic reduction scan does not replicate the stiffening-softening behavior observed during the anodic oxidation scan (Figures 4.16j, k, and l). This is especially apparent for $\Delta Y'$ - Δq_{V} dependencies, which exhibits a large hysteresis at the charge density in the range between 0 and $\Delta q_{\mathrm{V}}/2$.

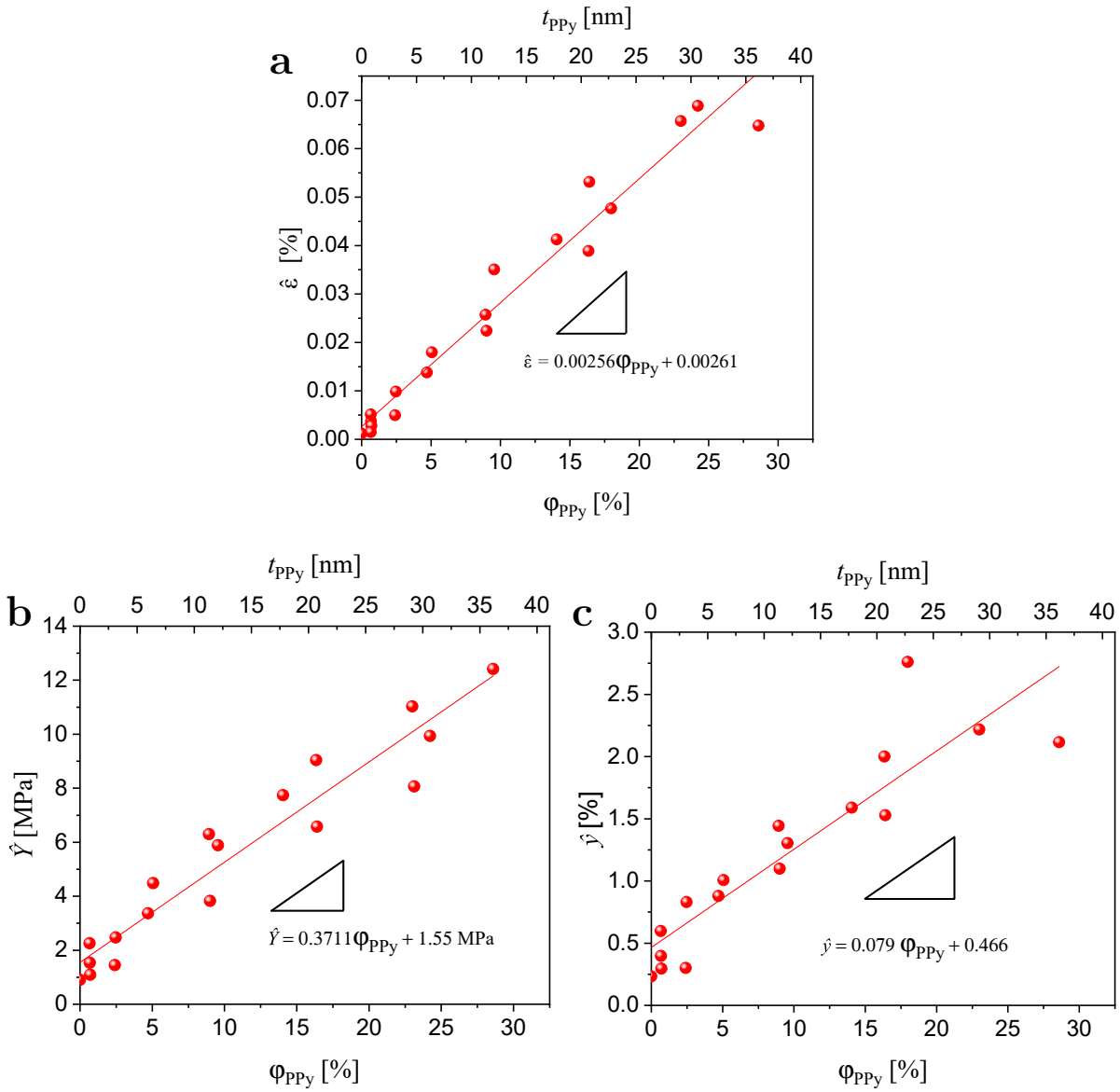

Figure 4.17. (a) Peak-to-peak amplitude of actuation strain, $\hat{\varepsilon}$ (as denoted in Figure 4.16p), (b) amplitude of the effective modulus variation, $\hat{Y}$ (as labeled in Figure 4.16l), and (c) amplitude of the relative changes of the effective modulus, $\hat{y} = \hat{Y}/Y_0'$, as a function of PPy volume fraction, φ_{PPy} Top axis is the corresponding PPy thickness, t_{PPy}. Red lines: The linear fit to the data, giving $\hat{\varepsilon} = 0.00256\varphi_{\mathrm{PPy}} + 0.00261$, $\hat{Y} = 0.3711\varphi_{\mathrm{PPy}} + 1.55$ MPa, and $\hat{y} = 0.079\varphi_{\mathrm{PPy}} + 0.466$.

Figure 4.17 summarizes the dependencies of the peak-to-peak amplitudes of actuation strain, $\hat{\varepsilon}$, the effective modulus variation, $\hat{Y}$, and the relative effective modulus variation, $\hat{y}$, on PPy volume solid fraction, φ_{PPy}, and PPy thickness, t_{PPY}. It can be seen that $\hat{\varepsilon}$ and $\hat{Y}$ scale linearly with φ_{PPy}. $\hat{\varepsilon}$ and $\hat{Y}$ values of NPG/PPy with $\varphi_{\mathrm{PPy}} <$ 2% are comparable to those of bare NPG and reach ~ 0.004% and ~ 1.5 MPa, respectively. At a maximum φ_{PPy} of around 30%, both $\hat{\varepsilon}$ and $\hat{Y}$ display about 7-fold increase compared to those of bare NPG. Yet, $\hat{y}$ vs. φ_{PPy} exhibits more scatter and does not precisely follow the linear dependence. This might originate from the discrepancies in the initial Young's modulus values, Y_0', of individual specimen as shown in Figure 4.15.

4.6.2 Impact of electrochemical conditions

4.6.2.1 Impact of scan rate

Section 4.6.1 reports *in situ* mechanical properties of NPG/PPy(0 ~ 35 nm) under cyclic potential sweeping with a potential scan rate, v, of 2 mV/s, which corresponds to a frequency of the applied potential cycle (0.4 ~ 0.8 V) of 0.0025 Hz. It has been found that Young's modulus behavior of NPG/PPy hybrids is drastically influenced by a PPy coating. In contrast to the double layer charging that takes place at the metal-electrolyte interface [168–170], the pseudo-capacitive charging-discharging occurs inside PPy matrix [172, 174]. These processes are related to the ion diffusion kinetics in PPy [164, 221], which can govern the viscoelastic response of NPG/PPy hybrids. For this reason, the effect of scan rate on the viscoelastic properties of NPG/PPy has been studied.

Figure 4.18 plots the electro-chemo-mechanical coupling of NPG/PPy(35 nm) at a scan rate of 5 mV/s (left column) and 0.2 mV/s (right column), which respectively corresponds to a frequency of applied potential cycle of 0.00625 and 0.000250 Hz which are much smaller than that (1 Hz) of the dynamic force. The Δq_{V} - E_{SHE} and ε - Δq_{V} relationships at 5 and 0.2 mV/s show the same features as the corresponding data recorded at 2 mV/s. Linear Δq_{V} - E_{SHE} relationships are observed with comparable Δq_{V} amplitudes around 25 mC/mm^3 at all 5, 2, and 0.2 mV/s (Figures 4.16h, 4.18c, and 4.18d). At 0.2 mV/s, the hysteresis between anodic and cathodic branches is the smallest, implying the predominant charge contribution from the PPy matrix as compared to the outer polymer surface. Therefore, the smallest and the largest ε are expected at 5 mV/s and 0.2 mV/s with a value of ~ 0.0028% and ~ 0.080% (Figures 4.18g and h), respectively.

The alternating stiffening-softening also exhibits a pronounced hysteresis during both anodic and cathodic scans at 0.2 mV/s, as shown in Figures 4.18b and f. Yet, at the fastest scan rate of 5 mV/s, such hysteresis is diminished and $\Delta Y'$ scales linearly with both E_{SHE} and Δq_{V} (Figures 4.18a and e).

The peak-to-peak amplitudes of actuation strain, $\hat{\varepsilon}$ (as defined in Figure 4.16p), and modulus variation, $\hat{Y}$ (as defined in Figure 4.16l), of NPG/PPy(35 nm) obtained at scan rates, v, of 0.2, 2 and 5 mV/s are summarized in Figure 4.19. Figure 4.19a shows $\hat{\varepsilon}$ and $\hat{Y}$ versus v. It can be seen that both of them follow a linear dependence on scan rate, with a slope of -2.650 ± 0.145 for $\hat{Y}$ - v and -0.010 ± 0.001 for $\hat{\varepsilon}$ - v. When extrapolating to the slowest scan rate, namely, $1/v \to +\infty$, a maximum $\hat{Y}$ and $\hat{\varepsilon}$ of 17.3 MPa and 0.083% could be achieved, respectively. However, if the potential scan rate is faster than 5 mV/s, length and modulus variations are too small to be detected. Figure 4.19b displays $\hat{\varepsilon}$ and $\hat{Y}$ as a function of the half-time, $t_{1/2}$, required for charging

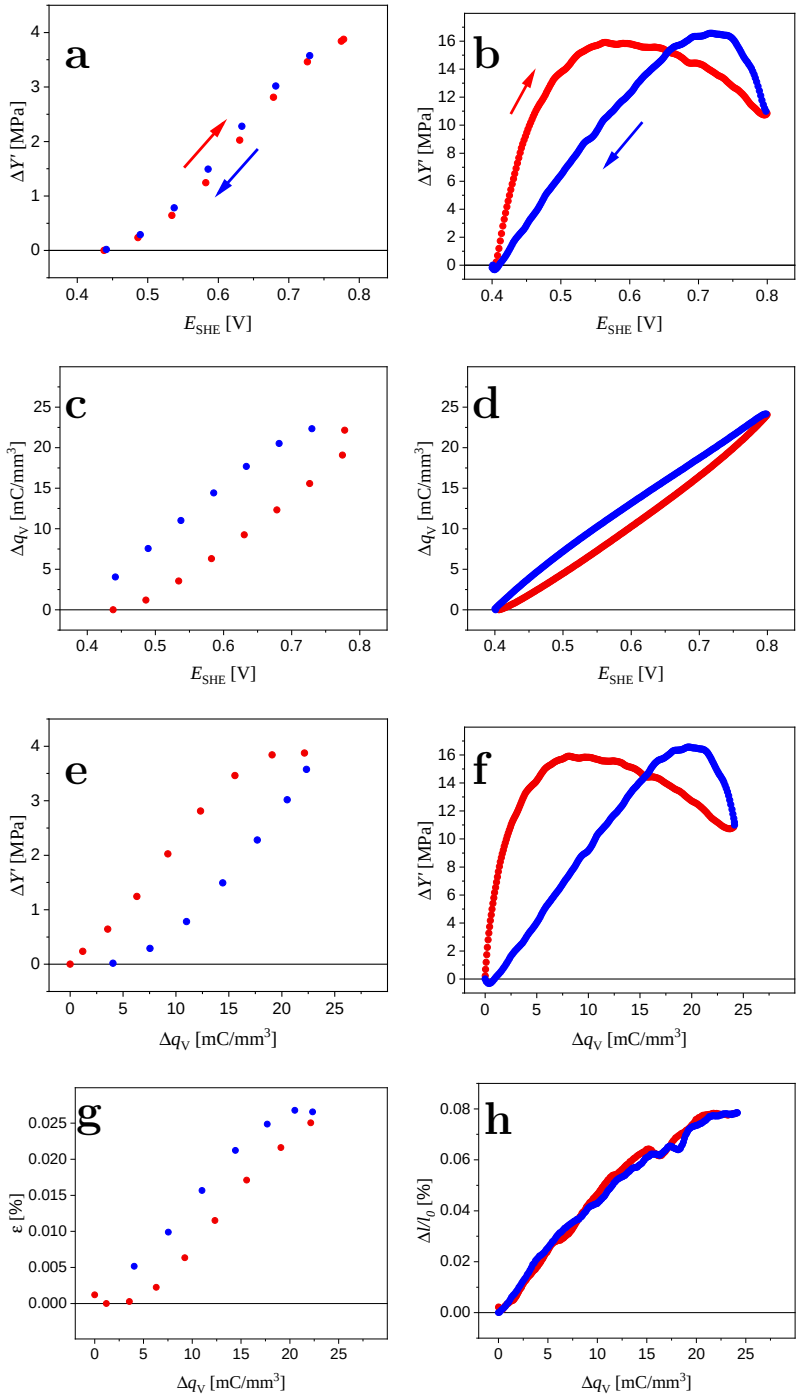

Figure 4.18. The electro-chemo-mechanical coupling of NPG/PPy(35 nm) at a scan rate of 5 mV/s (left column) and 0.2 mV/s (right column) in 0.1 M $HClO_4$ with compressive static stress, maximum dynamic stress, and dynamic stress frequency of ~ 5.02 MPa, ~ 0.64 MPa, and 1 Hz, respectively. $\Delta Y'$, the effective modulus variations; E_{SHE}, electrode potential; Δq_{V}, the net volumetric charge density; ε, the relative length change of the specimen. Red and blue arrows and dotted lines indicate anodic and cathodic sweeps, respectively. The data was averaged over three successive CV cycles, separately for positive and negative sweeps.

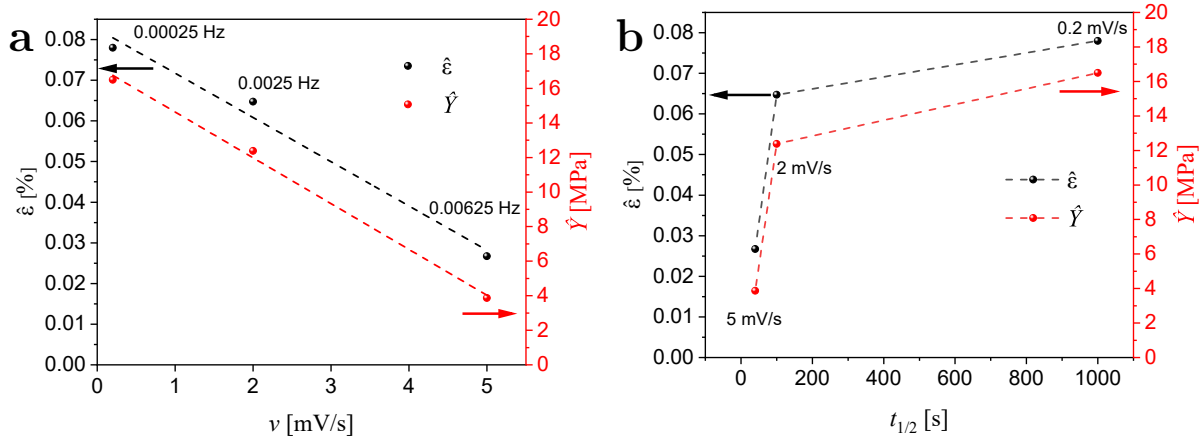

Figure 4.19. Peak-to-peak amplitudes of the actuation strain, $\hat{\varepsilon}$, and the effective elastic modulus variation, $\hat{Y}$, of NPG/PPy(35 nm) as a function of scan rate, v (a), and half-time required for charging and discharging, $t_{1/2}$ (b). The frequencies of the corresponding scan rates are marked in (a) and the scan rates of the corresponding half-time are labeled in (b). Left and right ordinates are $\hat{\varepsilon}$ and $\hat{Y}$, respectively. Dashed lines in (a): linear regressions with the slopes of -2.650 ± 0.145 for $\hat{Y}$ - v (red) and -0.010 ± 0.001 for $\hat{\varepsilon}$ - v (black).

and discharging. The $t_{1/2}$ for $\hat{\varepsilon}$ ~ 0.08% and $\hat{Y}$ ~ 16.5 MPa obtained at 0.2 mV/s are is 1000 s, whereas that for $\hat{\varepsilon}$ ~ 0.065% and $\hat{Y}$ ~ 12.4 MPa obtained at 2 mV/s is 100 s.

The electro-chemo-mechanical coupling results above, using NPG/PPy(35 nm) as an example, have revealed differences in the elastic modulus behavior at various scan rates. At the slower scan rate (under an approximately equilibrium condition), $\Delta Y'$ always shows a non-monotonous stiffening-softening behavior as a function of E_{SHE} (or Δq_{V}) during both anodic and cathodic scans. This is in contrast to the linear $\Delta Y'$ - E_{SHE} (or $\Delta Y'$ - Δq_{V}) seen at the faster scan rate.

4.6.2.2 Impact of potential range

In situ viscoelastic behavior was also investigated at different potential regimes, in which different oxidation and reduction states can be achieved within the same PPy film. In this section, the upper vertex potential was fixed, while the lower potential was varied (i.e. 0.6, 0.4, 0.2, and 0 V). Firstly, potential scanned in the potential regime of 0 ~ 0.8 V, immediately followed by potential sweeps in 0.2 ~ 0.8 V. Afterward, the potential window of 0.4 ~ 0.8 V was applied, after which potential finally scanned in 0.6 ~ 0.8 V. For all the four potential windows, potential scanned at a scan rate of 2 mV/s for eight cycles. The electrochemical and mechanical responses of the last three cycles were analyzed and the electro-chemo-mechanical couplings are displayed in Figure 4.20.

It can be seen that rectangular CV curves with comparable j_{V} values are observed (Figure 4.20a) at all potential ranges, indicating the same charging-discharging mechanism even at more negative potential regime E_{SHE} < 0.4 V. The corresponding $\Delta Y'$ were obtained and the anodic branch of $\Delta Y'$ - E_{SHE} curves are plotted in Figure 4.20b. Remarkably, non-linear $\Delta Y'$ - E_{SHE} relationships are observed in all potential windows. Taking a potential window of 0 ~ 0.8 V as an example, $\Delta Y'$ increases with E_{SHE} until ~ 0.16 V, followed by a decrease until the upper vertex potential with a tendency to invert its sign in the end of the potential range. The same behavior has also been

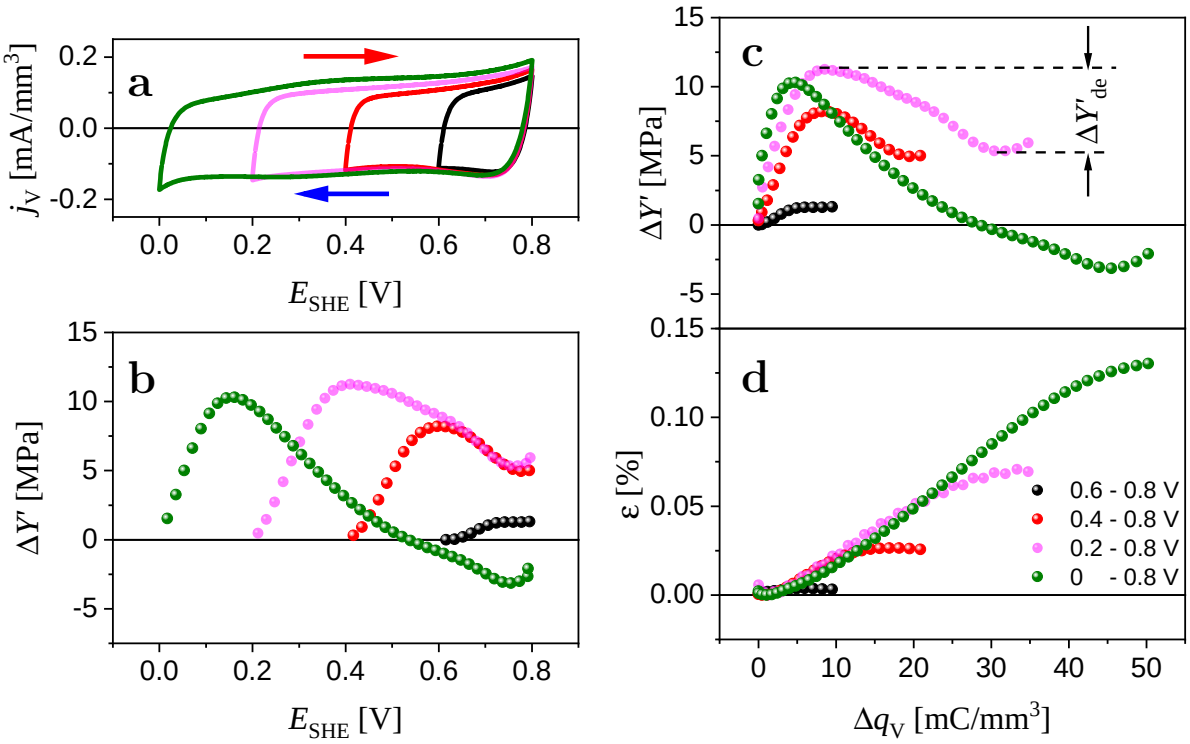

Figure 4.20. (a) CV curves showing the volumetric current density, j_V, versus potential, E_{SHE}, of NPG/PPy(30 nm) recorded at a scan rate of 2 mV/s in 0.1 M HCO_4 within various potential windows. The *in situ* DMA measurements were performed at compressive static stress, maximum dynamic stress, and dynamic stress frequency of ~ 5.02 MPa, ~ 0.64 MPa, and 1 Hz, respectively. The anodic branch of the effective elastic modulus variation, $\Delta Y'$, versus E_{SHE} (b) and volumetric charge density, Δq_V (c). (d) The anodic branch of relative length changes, ε, as a function of Δq_V. Red and blue arrows indicate positive and negative scan directions, respectively. The data was averaged over three successive CV cycles.

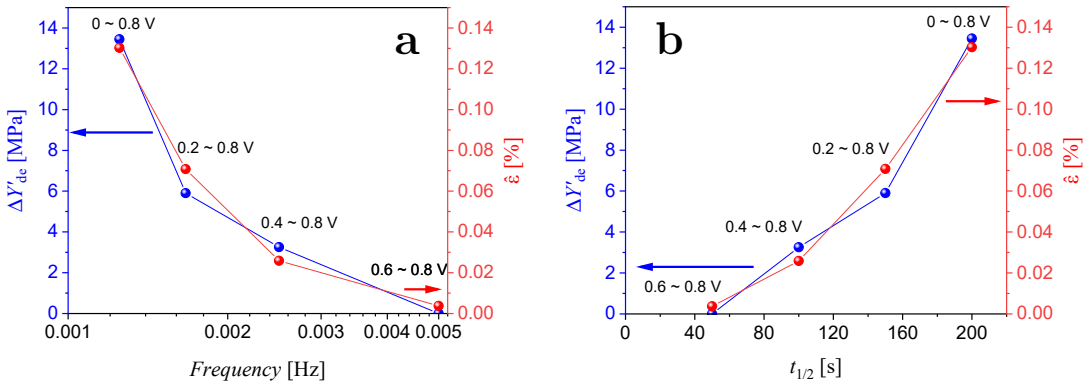

Figure 4.21. Peak-to-peak amplitudes of the actuation strain, $\hat{\varepsilon}$, elastic modulus decrease, $\Delta Y'_{de}$ (as defined in Figure 4.20c), as a function of the potential sweep frequency (a) and half-time, $t_{1/2}$ (b), required for charging and discharging. The frequencies are the inverse of the time per CV cycle of the selected potential regimes as indicated in the figure. Left and right ordinates in (a) and (b) indicate $\Delta Y'_{de}$ and $\hat{\varepsilon}$, respectively.

found in the potential ranges of 0.2 ~ 0.8 V and 0.4 ~ 0.8 V. It is notable that even for the smallest potential interval of 0.2 V (namely, 0.6 ~ 0.8 V), $\Delta Y'$ - E_{SHE} still shows a non-monotonous response. $\Delta Y'$ reaches 1.05 MPa at 0.71 V and essentially stays constant up to 0.8 V. Figure 4.20c shows the $\Delta Y'$ - Δq_{V} relationship and the same stiffening-softening phenomena is again observed. It is remarkable that irrespective of the potential window (the oxidation and reduction state in PPy matrix), $\Delta Y'$ changes its trend around Δq_{V} of 5 ~ 10 mC/mm^3. Moreover, the maximum $\Delta Y'$ values are the same (~ 10 MPa) for all the potential regimes except 0.6 ~ 0.8 V.

Figure 4.20d plots the relative length variation ε as a function of Δq_{V}. ε shows a linear dependence on Δq_{V}, and the bigger the potential window the larger the ε. Interestingly that, the linear parts of the ε - Δq_{V} curves overlap and exhibit the same slope of 0.026 ± 0.00047 mm^3/C.

The amplitude of the elastic modulus decrease, $\Delta Y'_{\mathrm{de}}$ (as defined in Figure 4.20c), and the peak-to-peak actuation strain amplitude, $\hat{\varepsilon}$, are plotted with frequency (the inverse of time per CV cycle) as shown in Figure 4.21a. At the smallest frequency, namely at the biggest potential window (0 ~ 0.8 V), $\Delta Y'_{\mathrm{de}}$ and $\hat{\varepsilon}$ exhibit the largest amplitudes of ~ 14 MPa and ~ 0.13%, respectively. Both $\Delta Y'_{\mathrm{de}}$ and $\hat{\varepsilon}$ decrease with frequency, and negligibly small $\Delta Y'_{\mathrm{de}}$ and $\hat{\varepsilon}$ are observed at the potential regime of 0.6 ~ 0.8 V. $\Delta Y'_{\mathrm{de}}$ and $\hat{\varepsilon}$ are also plotted versus half-time, $t_{1/2}$, required for the charging and discharging of the studied potential ranges (Figure 4.21b). It has shown that $\Delta Y'_{\mathrm{de}}$ and $\hat{\varepsilon}$ increase, in an approximately linear manner, with $t_{1/2}$, indicating the identical ions kinetics in the applied potential regimes.

4.6.3 Impact of H_2O molecule

Sections 4.6.1 ~ 4.6.2.2 investigate the elastic modulus behavior of NPG/PPy hybrids via *in situ* DMA analysis in aqueous $HClO_4$ electrolyte under various conditions. A non-monotonous $\Delta Y'$ - E_{SHE} behavior has been revealed. During oxidation and reduction processes, not only ClO_4^- are absorbed-repelled, H_2O molecules in form of solvation shell and free water are also involved (section 2.5.2). The flux of ClO_4^- can be monitored by oxidation states (e.g., scan rate and potential window), the effect of H_2O molecule can be studied by using an anhydrous organic solvent, such as propylene carbonate (PC). This section explores the impact of H_2O molecules on the elastic modulus behavior under *in situ* DMA analysis in PC solvent containing 0.3 M $LiClO_4$. Due to the large size, PC molecules are not incorporated into PPy matrix [33] so that only ClO_4^- anions are incorporated into PPy matrix during charging.

Figure 4.22 displays the electro-chemo-mechanical coupling of NPG/PPy(35 nm) obtained in the anhydrous organic electrolyte. The CV curves show a quasi-rectangular profile, indicating the pseudo-capacitive charging-discharging mechanism in the organic electrolyte (Figure 4.22a). The comparable current densities with those obtained in aqueous $HClO_4$ electrolyte (Figure 4.11a) as well as the superimposed CV curves suggest the stability and reversibility of PPy film in the organic electrolyte in the studied potential window.

Figure 4.22b depicts the elastic modulus variation, $\Delta Y'$, as a function of electrode potential, E_{SHE}. Clearly, an apparent linear $\Delta Y'$ - E_{SHE} relationship is observed irrespective of the hysteresis between anodic and cathodic scans at the larger potential regime. Figure 4.22c shows that the transferred charge density, Δq_{V}, linearly varies with E_{SHE}. The perfectly closed Δq_{V} - E_{SHE} curve indicates that the transferred charge

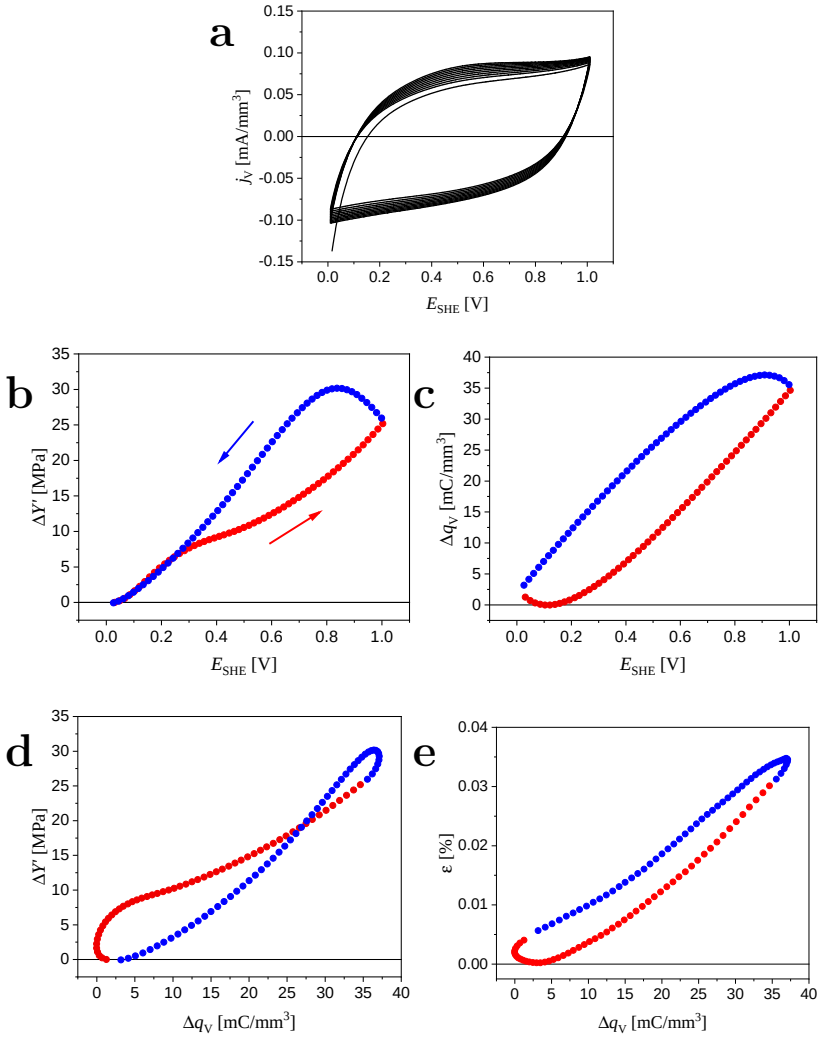

Figure 4.22. The electro-chemo-mechanical coupling of NPG/PPy(35 nm) hybrid obtained in anhydrous propylene carbonate (PC, 99.7%, Sigma-Aldrich) containing 0.3 M $LiClO_4$ at a scan rate of 2 mV/s with compressive static stress, maximum dynamic stress, and dynamic stress frequency of ~ 5.02 MPa, ~ 0.64 MPa, and 1 Hz, respectively. (a) Current per outer sample volume, j_V, as a function of electrode potential, E_{SHE}. (b) Elastic modulus variation, $\Delta Y'$, versus E_{SHE}. (c) Transferred charge density per specimen volume, Δq_V, with respect to E_{SHE}. (d) $\Delta Y'$ vs. Δq_V. (e) Actuation strain, ε, as a function of Δq_V. Red and blue dotted lines and arrows indicate respectively anodic and cathodic sweeps. The data in (b-e) was averaged over three successive CV cycles, separately for positive and negative-going sweeps.

is recoverable. Figure 4.22d plots $\Delta Y'$ - Δq_V curve. The linear $\Delta Y'$ - Δq_V obtained in the non-aqueous solvent is strikingly different from the non-monotonous $\Delta Y'$ - Δq_V obtained in aqueous $HClO_4$ electrolyte (Figures 4.16c and d), indicating the softening effect of H_2O molecule on the elastic modulus of NPG/PPy hybrids. Moreover, the hysteresis has diminished. Figure 4.22e depicts the actuation strain, ε, with Δq_V. The linear relation between the strain and the charge density is in accordance with the well-established notion that the actuation and the charge transfer are associated with the same anion exchange process between polymer and electrolyte.

4.7 Actuation under load

4.7.1 Overview of actuation under load

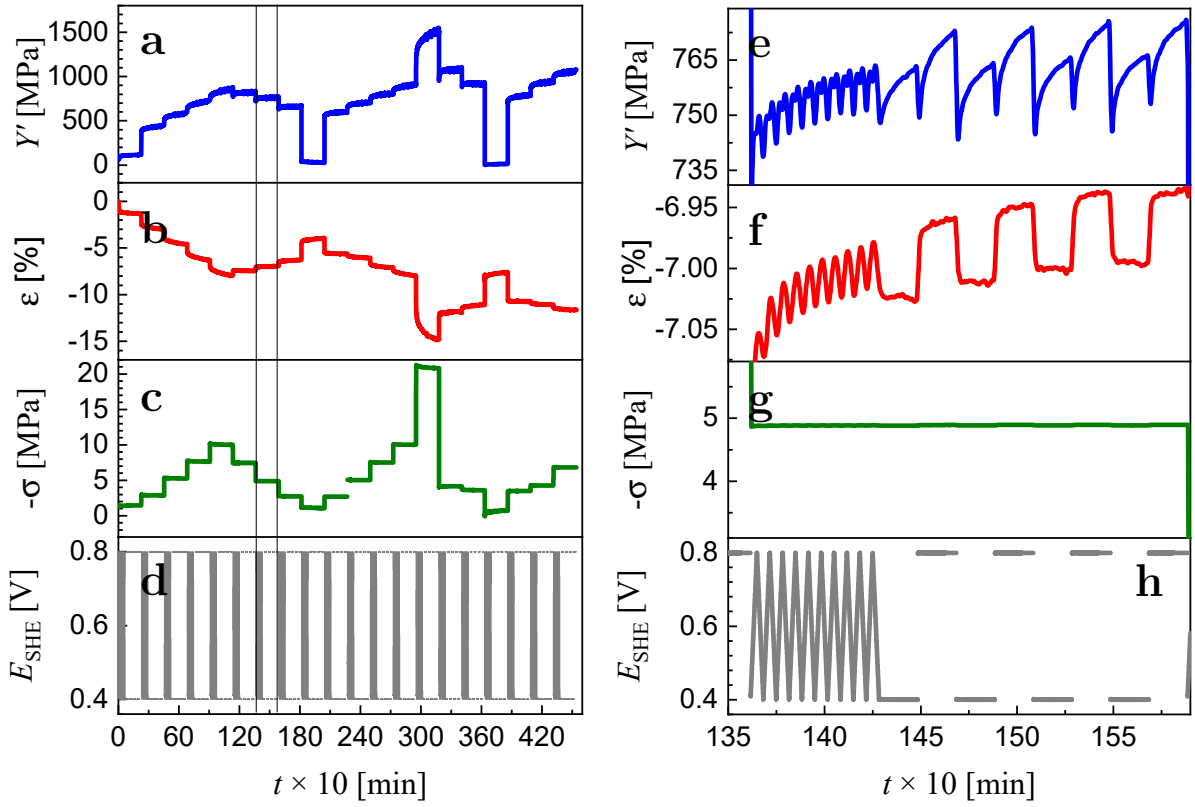

Figure 4.23. *In situ* DMA on NPG/PPy(30 nm) under various loads. Overview of the effective elastic modulus, Y' (a), strain, ε (b), compressive loads, σ (c), and electrode potential, E_{SHE} (d) versus time, t. (e) and (f) show the corresponding Y' and ε responses upon ten CV cycles and eight potential jumps (h) under a specific load of -4.88 MPa (g) as marked in the left figure. (c) shows the compressive stress variations from -1.13 to -20.88 MPa. During the measurement, the dynamic force with an amplitude of 0.64 MPa and a frequency of 1 Hz was superimposed on each load. The negative ε values in (b) indicate the contraction of the specimen. (g) magnifies the representative constant stress step, during which first a cycle voltammetry (ten cycles) with a scan rate of 2 mV/s was run followed by eight successive potential jumps with a duration of each step for 20 min. The measurements were performed in 0.1 M $HClO_4$.

The results above reveal NPG as an actuator with a small actuation amplitude, yet

the actuation strain of bare NPG can be greatly improved by coating Au ligaments with PPy.

So far, the actuation properties of nanoporous metals have been mainly studied at negligibly small loads applied by a dilatometer [51, 52, 55]. However, it is of practical importance to investigate the actuation behavior under the higher loads. The actuation of NPG under external loads was investigated and it has been found that the strain in response to the double-layer charging is invariant under an external load [31]. In contrast, the actuation strain amplitude of PPy films has been found to decrease when the load increases [1, 14, 38, 103, 222, 223]. In this work, taking NPG/PPy(30 nm) hybrids as an example, *in situ* actuation under loads was explored.

Because the upper force limitation of the DMA device is 20 N, a maximum compressive force of -18 N (-20.88 MPa) was applied. As indicated by the load-unload results in Figure 4.13, 20 MPa corresponds to a deformation of ~ 10% for NPG/PPy(30 nm), and NPG/PPy specimen is not destroyed under such conditions. A series of static compressive stresses ranging from -1.13 to -20.88 MPa were applied, while the dynamic stress with an amplitude of 0.64 MPa was kept constant.

The left subfigure in Figure 4.23 overviews the profiles of the effective elastic modulus, Y', actuation strains,ε, and electrode potential, E_{SHE}, under various stresses, σ. To eliminate the creep that has been found in PPy [8, 10], the sample was initially stepwise predeformed up to -10 MPa, as shown in Figures 4.23b and c. The NPG/PPy specimen exhibits the corresponding contractions up to ~ -7.8% (the negative sign indicates compression). Afterwards, the loads were decreased up to -1.13 MPa, which resulted in the recovery of ε to ~ -4%. This implies the total deformation of the specimen of ~ 3.8%. When the load went up to -10 MPa again, ε attains comparable values with those obtained during the former load release stage. This indicates that the densification induced by the predeformation extends the elastic regime and NPG/PPy specimen behaves elastically under a load ≤ -10 MPa. When the load increases to -20.88 MPa, the hybrid is compressed to ~ -12.5% followed by a continuous creep ($\varepsilon \simeq$ -14.5%) during the loading step. During this stage, NPG/PPy specimen is plastically deformed and the elastic regime is further extended so that comparable ε is observed during the following unloading and reloading steps.

Upon compression, the effective elastic modulus, Y', also varies in a stepwise manner (as shown in Figure 4.23a). Y' increases upon loading and decreases upon unloading, showing reproducible values after densification under -10 and -20.88 MPa. Figure 4.24 depicts Y' - $\varepsilon_{\mathrm{eng}}$ relationship and compares Y' values obtained from the load-unload compression tests (section 4.5) and that recorded from *in situ* DMA experiments. The consistency of the two data sets indicates the validity of the DMA measurement under the applied load protocol (Figure 4.23c). Note that under the loads around -1.13 MPa, Y' shows values less than 150 MPa (as marked by the rectangular dashed box in Figure 4.24). This might be due to the poor contact between the specimen and the pushrod under such low loads, and the corresponding results under these loads will not be analyzed.

Under each load, an electrochemical control was applied *in situ* (Figure 4.23d). The right subplot in Figure 4.23 shows Y', ε, and E_{SHE} under a representative load of -4.88 MPa, as marked in the left subfigure. Ten successive potential sweeps (between 0.4 and 0.8 V) were carried to achieve a continuous change of oxidation-reduction states in PPy. Prior to applying the next load, eight potential jumps (between 0.4 and 0.8 V) were carried out to get stationary oxidation and reduction status in PPy, as shown in

Figure 4.23h. This thesis focuses on the modulus behavior upon cyclic potential sweeps which provide a consecutive change of oxidation and reduction status.

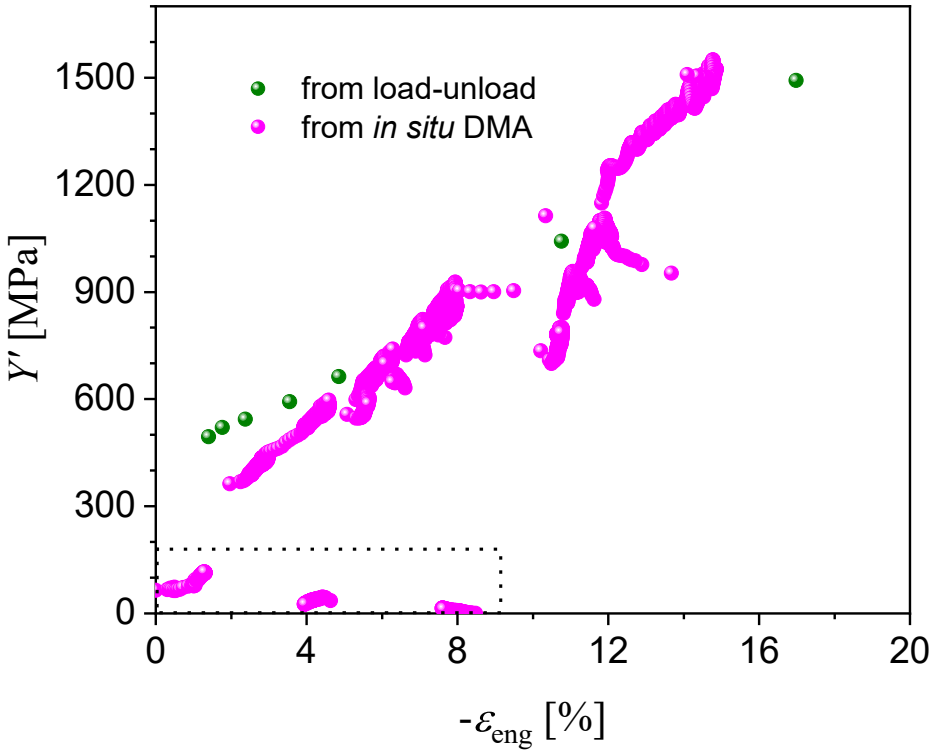

Figure 4.24. Effective elastic modulus, Y', versus strain, ε, of NPG/PPy(30 nm) obtained from load-unload and *in situ* DMA experiments. Although the two types of experiments were performed with two different specimens, a consistency of the two data sets is remarkable. The rectangular dashed box indicates the anomalously small Y' (< 150 MPa) obtained under the stress around -1.13 MPa. '$-\varepsilon_{eng}$' means the contraction of the specimen.

4.7.2 Actuation upon cyclic voltammetry

The actuation behavior under various loads was studied during *in situ* cyclic potential sweeps. As shown in Figure 4.23h, ten successive cyclic potential sweeps were applied. Figures 4.23e and f demonstrate that under a load of -4.88 MPa Y' and ε drift upwards with time and exhibit stable and reproducible signals. The electro-chemo-mechanical coupling is studied based on the last three potential cycles. Figure 4.25 depicts the effective elastic modulus variation, $\Delta Y'$, actuation strain, ε, and volumetric charge density, Δq_V, responses (with subtracting the baseline) during potential cycles under loads ranging from -2.74 to -20.88 MPa. As shown in Figure 4.25a, at all loads, change in Young's modulus, $\Delta Y'$, displays stiffening-softening behavior during both anodic and cathodic scans and increase with load.

Concerning the variation of the volumetric charge density, Δq_V, Δq_V versus t curves (Figure 4.25c) overlap upon successive potential sweeps at all loads, indicating that electrochemical processes are independent of loads. The actuation strain, ε, is constant as in the range of the applied stresses except at -20.88 MPa (Figure 4.25b). This might be due to the interference induced by the large creep at such a high load (the large ε decrease around t = 3000 min, Figure 4.23c). The stress (-20.88 MPa) was excluded from further analysis. Irrespective of the strain deviation at large load, the findings

point to the enhanced capability of NPG/PPy hybrids to sustain significant stress during actuation, in contrast to backward of bare NPG at large load [31].

The strain-charge coupling is further analyzed by plotting the actuation strain versus potential and charge in Figure 4.26. Figure 4.26a shows the anodic part of ε vs. E_{SHE}. ε first decreases up to ~ 0.475 V, followed by a linear increase. Since the existence of the polymer chains rearrangement inertia in PPy matrix during oxidation and reduction processes [38, 183, 224, 225], the decrease of ε at 0.4 ~ 0.45 V might be due to the contraction hysteresis of the proceeding reduction process. ε vs. E_{SHE} curves superimpose at all loads except at σ= -20.88 MPa. In other words, the actuation strain of NPG/PPy is independent of the applied load.

The contribution of Young's modulus variation to the actuation strain is obtained from the second term of Eq. 2.8 and is shown in Figure 4.26b. At all loads, $\varepsilon_{\delta \mathrm{Y}'}$ - E_{SHE} curves exhibit well reproducible increasing-decreasing behavior. Moreover, $\varepsilon_{\delta \mathrm{Y}'}$ - E_{SHE} curve increases with loads (as marked by the black arrow). This is expected in a view of the increasing $\Delta Y'$ with load (Figure 4.25a).

Subtracting $\varepsilon_{\delta \mathrm{Y}'}$ from ε allows one to separate a contribution of the strain induced by $\Delta Y'$ from ε. The resulting ε_0 - E_{SHE} curves are shown in Figure 4.26c. In the potential window 0.4 ~ 0.52 V, ε_0 - E_{SHE} curves decrease followed by the increase up to the end of the potential range. It is remarkable that at 0.4 ~ 0.52 V ε_0 increases with load, implying that the electrochemical hysteresis in PPy depends on loads. Yet, in 0.52 ~ 0.8 V, ε_0 - E_{SHE} points to the lesser expansion of NPG/PPy hybrids under load (except at σ = -20.88 MPa). This finding indicates that electrochemical actuation is affected by load, although the volumetric charge density variation, Δq_{V}, versus potential E_{SHE} are linear over the whole potential range and is not affected by the load (Figure 4.26d).

The electro-chemo-mechanical coupling was also studied by dilatometer which applied a load of -0.27 MPa, which is negligibly small in comparison to the loads provided by DMA. In this case, the NPG/PPy actuator can be regarded to work under no external load, and therefore, the corresponding strain can be reasonably treated as the actuator strain (free stroke) caused by the electrochemical oxidation-reduction process. The strain and transferred charge are plotted in Figure 4.26c and Figure 4.26d, respectively. It can be seen that the charge recorded at -0.27 MPa is superimposed on those gained at other loads. However, the linear ε_0 - E_{SHE} is different from those obtained under other loads. This observation again suggests the effect of load on the electrochemical actuation. Irrespective of ε_0 - E_{SHE} shapes, the strain difference between 0.4 V and 0.8 V, namely $\varepsilon_{0,0.8\mathrm{V}} - \varepsilon_{0,0.4\mathrm{V}}$, obtained at -0.27 MPa is ~ 0.017%, which is close to those evaluated from ε_0 - E_{SHE} curves of other loads.

Figure 4.26e depicts ε versus Δq_{V}. A small ε decrease is observed up to ~ 2.5 mC/mm^3. When more charge is passed, ε varies essentially linearly with Δq_{V} and all ε - Δq_{V} curves superimpose. The strain-charge coefficients are extracted from the slops of the linear regressions (A^* =dε/dq_{V}). Besides, the contribution of the free stroke, ε_0, to A^* is also obtained. The results are compiled versus applied load in Figure 4.26f. It can be seen that both A^* and A_0^* are invariant of load (except σ = -20.88 MPa) with respectively values around 0.025 and 0.006 mm^3/C, implying the independence of dε/dq_{V} on the load. At the small load of -0.27 MPa, a smaller $A_0^* \simeq$ 0.0011 mm^3/C is obtained. It should be noted that a $A^* \simeq 0.027$ mm^3/C is obtained at various potential windows as shown in Figure 4.20. The experiments were performed with different NPG/PPy(30) specimens, indicating excellent reproducibility of ε and A^* under load.

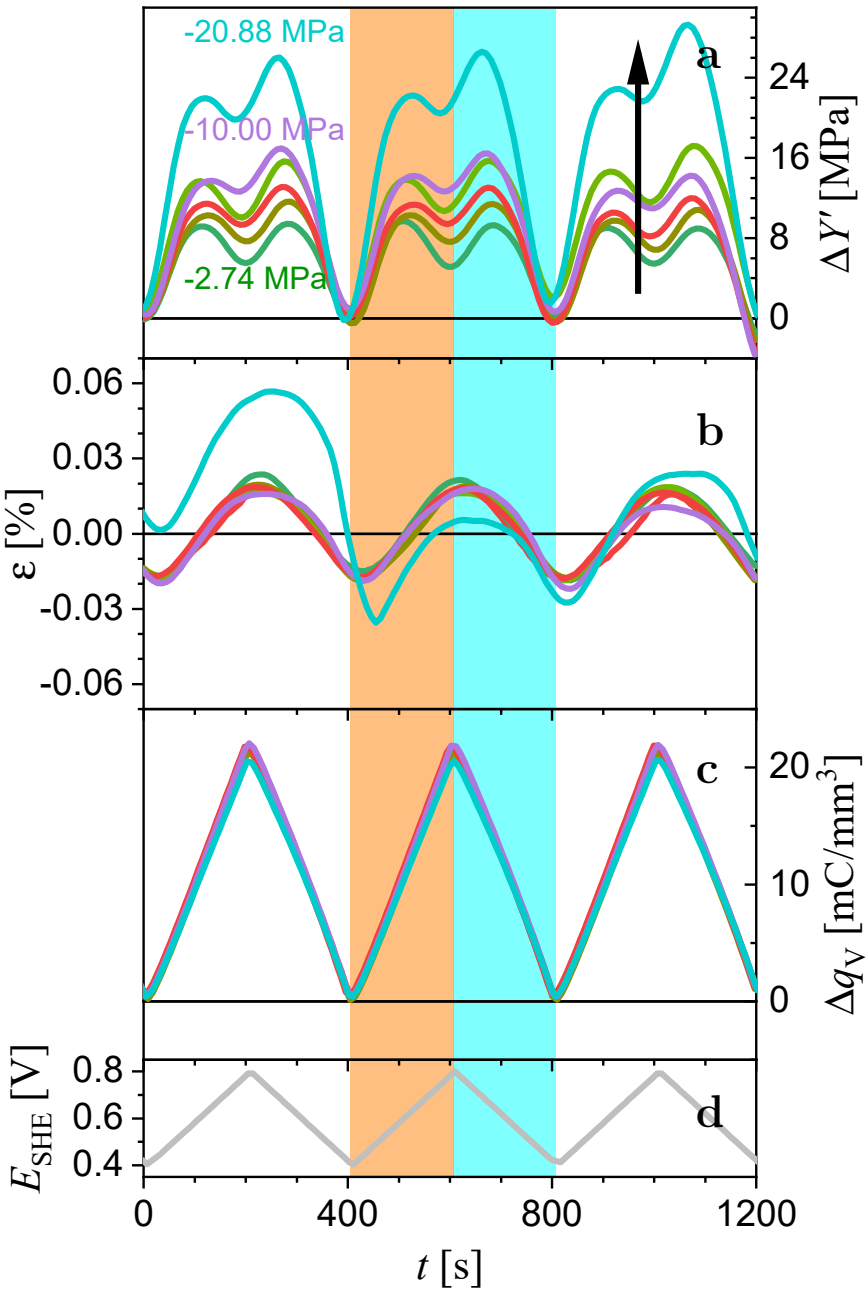

Figure 4.25. Electro-chemo-mechanical coupling of NPG/PPy(30 nm) during *in situ* cyclic potential sweeps at a scan rate of 2 mV/s in 0.1 M $HClO_4$ under loads with dynamic stress amplitude of ~ 0.64 MPa, dynamic stress frequency of 1 Hz. (a) Young's modulus variation, $\Delta Y'$, (b) actuation strain (relative length change), ε, (c) net volumetric charge density, Δq_V, and (d) applied potential sweeps, E_{SHE}, under various loads versus time, t. Load increases from -2.74 to -20.88 MPa as marked by the black arrow in (a). The curve color conventions are the same as those in Figure 4.26a. Volumetric charge density, Δq_V, is obtained by normalizing the net charge over the apparent volume of the specimen. Orange and cyan rectangles indicate positive and negative scans, respectively.

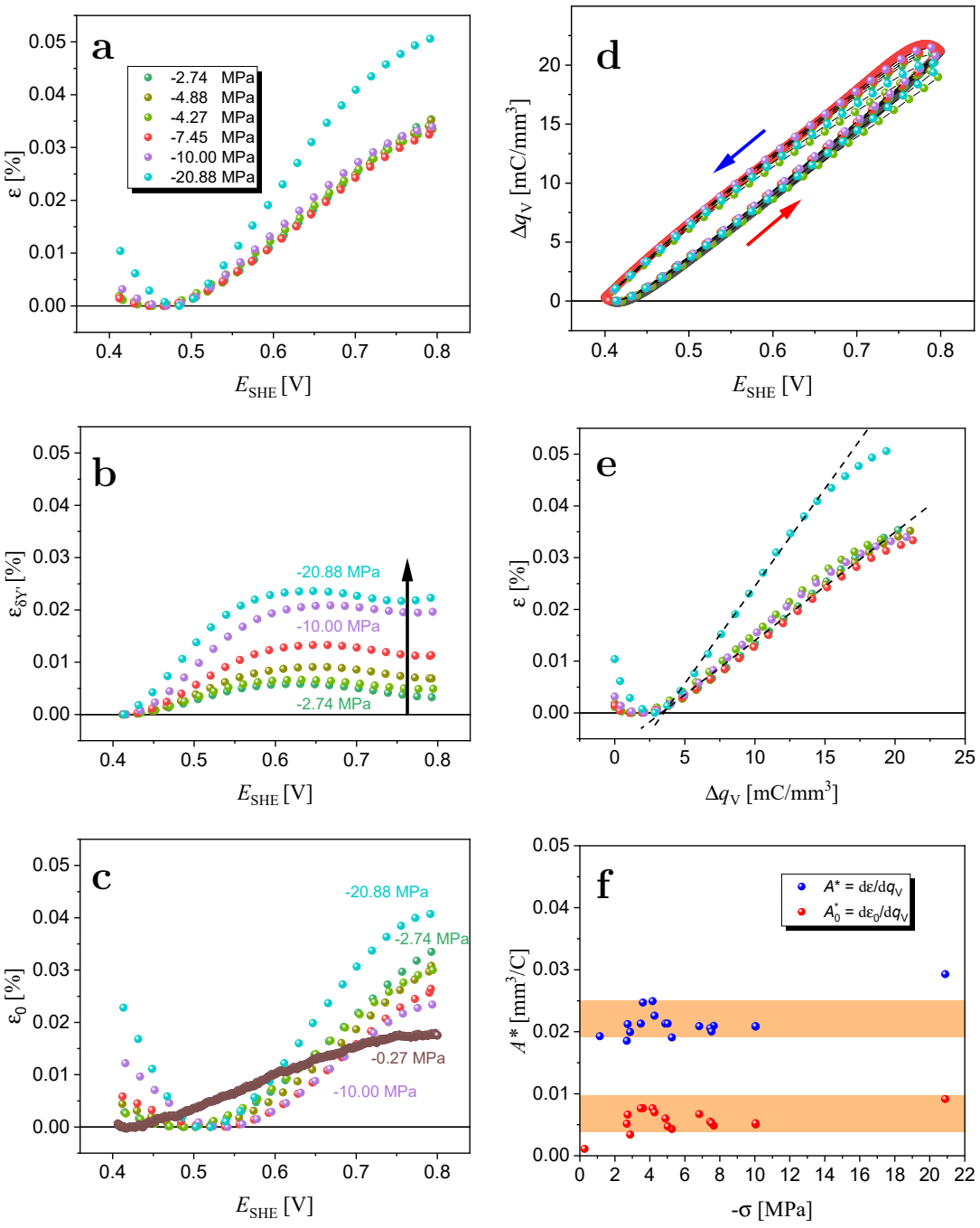

Figure 4.26. Electro-chemo-mechanical coupling of NPG/PPy(30 nm) during *in situ* cyclic potential sweeps under loads. The data are extracted from Figure4.25 and only the anodic scan is shown. (a) Actuation strain, ε, as a function of potential, E_{SHE}. (b) Strain induced by elastic modulus variation $\varepsilon_{\delta \mathrm{Y}'}$ (calculated according to the second term in Eq.2.8) versus E_{SHE}. The black arrow indicates increasing of the applied load. (c) Electrochemical actuation strain (free stroke, after subtracting $\varepsilon_{\delta \mathrm{Y}'}$ from ε), ε_0 versus E_{SHE}. The brown dotted line indicates the actuation recorded by the dilatometer at a load of -0.27 MPa. (d) Volumetric charge density, Δq_{V}, versus E_{SHE}. The charge density recorded during *in situ* dilatometry measurement is also plotted and it overlaps with those obtained from *in situ* DMA measurement. (e) Actuation train, ε, as a function of Δq_{V}. The dashed lines are linear regressions with slopes that denote the strain-charge coefficient $A^* = \mathrm{d}\varepsilon/\mathrm{d}q_{\mathrm{V}}$. (f) A^* (and A_0^*) vs. σ. Blue dots: A^* from the actuation strain, red dots: Contribution from the free stroke to A^*. Arrows in (d): Red and blue denote anodic and cathodic scan directions, respectively. The colors and symbols of the corresponding loads are denoted in (a) and are the same as conventions in Figure 4.25.

Chapter 5

Discussion

In this work, mm-scaled NPG/PPy electroactuators are synthesized. The elastic modulus and actuation behavior of NPG/PPy hybrid electroactuators are studied by *in situ* DMA under electrochemical control in the aqueous $HClO_4$. This chapter will discuss the microstructure, electrochemical behavior, mechanical behavior, the elastic modulus behavior under electrochemical control, and actuation under load.

5.1 Microstructure

Samples of mm-sized NPG are successfully produced via electrochemical dealloying of $Ag_{75}Au_{25}$ cylinders. The elaborate dealloying conditions and alloy composition allow the fabrication of bulk NPG free of cracks which is the precondition for mechanical testing under load. The as-dealloyed specimens are characterized by a 3D bicontinuous ligament-pore network with mean ligaments width $L_D \sim 27 \pm 4$ nm. After annealing, ligaments are coarsened with $L_D \sim 160 \pm 40$ nm (section 4.1). Meanwhile, the pores among the ligaments also grow to accommodate the deposition of PPy coating. PPy thickness is deliberately chosen so as to not completely fill the pore space which severs as the pathway for the flow of electrolytes.

PPy coatings with thickness, t_{PPy}, ranging from 1 to 35 nm are deposited on NPG ligaments. Although the coatings with $t_{PPy} < 6$ nm is not visible in SEM images (Figures 4.5a and b), the element distribution patterns of carbon and oxygen (which respectively comes from polymer chain and doped ClO_4^-, Figures 4.6c and d) from EDX suggest the successful deposition of PPy. Moreover, the deposition charge recorded by potentiostat is used to estimate PPy thickness [87, 201]. The measured PPy thicknesses agree well with those theoretically estimated ones (Figure 4.7). The relationship between PPy thickness and electropolymerization charge density obeys $t_{PPy} = 2.91$ nm/(mC/cm^2) * Q_A which is close to that ($t_{PPy} = 2.5$ nm/(mC/cm^2) * Q_A [142, 214]) in literature. This also allows one to get ultra thin PPy film with $t_{PPy} \sim 1$ nm at expense of $Q_A = 3.2$ C/cm^2. PPy volume fractions, however, are underestimated in contrast to the theoretical ones (Figure 4.8). That might be due to the loss of H_2O (incorporated in form of solvation shell out ClO_4^- and free water during polymerization process [7, 180, 187, 215]) during drying, consequently inducing measurement error.

5.2 Electrochemical behavior

The electrochemical study starts with the comparison of linear scan voltammetry and staircase voltammetry. As accounted in section 3.2.2, the charge obtained from staircase voltammetry is underestimated in contrast to that recorded from linear scan voltammetry. However, the minimum scan rate, v, of linear scan voltammetry is 10 mV/s which is too fast to be applied in this thesis.

Section 4.2.1 compares the performance of linear scan and staircase voltammetry on Au/PPy(20 nm) and Au/PPy(1200 nm) bi-layers which respectively corresponds to PPy volume of 7.22×10^{-4} mm^3 and 4.33×10^{-2} mm^3. In the case of Au/PPy(20 nm), it has been found that the charge obtained at staircase voltammetry is about half of that obtained at linear scan voltammetry (Figure 4.3c). In the case of Au/PPy(1200 nm), however, the charge obtained at staircase voltammetry is very close to that obtained at linear scan voltammetry (Figure 4.3d). The findings verify the descriptions in section 3.2.2. At staircase voltammetry, when reducing scan rate to 2 mV/s the current is greatly reduced (Figures 4.3a and b) but the charge does not show a big difference (Figures 4.3c and d). This might be because that although the charge at the material-electrolyte interface is less involved the Faradic charge associated with ions exchange between material matrix and bulk electrolyte plays a bigger role [176, 178]. Since the amount ($\sim 0.1 \times 10^{-2}$ to $\sim 3 \times 10^{-1}$ mm^3) of PPy in mm-scaled NPG/PPy specimens is comparable to that (4.33×10^{-2} mm^3) in Au/PPy(1200 nm) bi-layer and the time interval (1s, section 3.2.2) of a potential step is much bigger than that (33 ms for a 158 nm-thick PPy [197] and 6 ms for 35-nm-thick PPy as described in section 5.5) required for anions to diffuse into PPy film, the current and charge of NPG/PPy obtained at staircase voltammetry are reliable.

Cyclic voltammograms are applied to determine the surface area of NPG which is used to evaluate PPy thickness as discussed in section 5.1. As only double layer charging-discharging takes place on the gold-electrolyte interface [169, 171, 177], the slope of the current - scan rate plot (Figure 4.4b) gives the capacitance of NPG (L_D ~ 160 nm) of $\sim 1.75 \times 10^{-3}$ F/mm^3. According to the capacitance ratio method (section 3.4.3), the surface area of NPG of ~ 1 mm in diameter and ~ 1.6 mm in height is ~ 100 cm^2, which is very close to that (~ 110 cm^2) estimated from the geometry method as described in section 3.4.3.

The CV curves explored at an extended potential window of 0 ~ 1.7 V (Figure 4.9) enables one to determine the proper potential range for *in situ* DMA measurement. The current degradation of PPy at a high potential regime (E_{SHE}> 0.9 V) agrees with the over-oxidation of PPy reported in the literature [109, 200]. The lower potential regime of 0 ~ 0.4 V is not desired, since the Faradic current induced by the oxygen reduction in aqueous electrolyte [226] would interfere with the evaluation of charge.

PPy stores charge in a pseudo-capacitive way [142, 172, 174, 212]. The rectangular CV curves in Figures 4.3e, 4.10, and 4.11a suggest that NPG/PPy specimens also charge-discharge in a pseudo-capacitive manner. The specific capacitance increases with PPy thickness, which is in accordance with previous reports [29, 30]. It should be noted that the capacitance will be affected by the nanopores at high scan rates. For planar Au/PPy(1200 nm) bi-layer, current at 50 mV/s still falls on the linear regression (Figure 4.3f), however, current of NPG/PPy(35 nm) at scan rate > 10 mV/s fall below the linear regression (Figure 4.11b). In other words, the electrolyte exchange between NPG/PPy interior and bulk electrolyte at relatively high scan rates is limited. At a

high scan rate, the lack of ClO_4^- and the insufficient time for ClO_4^- to diffuse into PPy matrix will induce a smaller capacitance. By contrast, at small scan rates ≤ 5 mV/s, the electrolyte diffusion is fast enough and the depletion of ClO_4^- in pore space is avoided. Moreover, the time is sufficient to incorporate as much ClO_4^- as possible into PPy matrix.

5.3 Mechanical behavior

The study of flow stress - strain behavior allows one to determine the load and the elastic deformation range of NPG and NPG/PPy specimens during *in situ* DMA measurement. In this thesis, the relatively low strength of NPG has been found and it is in accordance with the low strength of nanoporous metals with increased L_D [26, 70, 72, 210, 227, 228]. The ligament strength, σ, and ligaments size, L_D, follows a scaling equation $\sigma_{lig} \propto L_D^{-n}$ where $n = 0.623$ is a power-law empirical exponent [229]. Because of the negligible lateral expansion during compression up to a 50% deformation [24], the compression induced change in axial direction causes the volume reduction, and consequently, producing an increased solid fraction, φ. Since the relationship between the strength and solid fraction follows $\sigma \propto \varphi^{3/2}$ [230], and therefore, a significantly increased σ of ~ 80 MPa at $\varepsilon_{eng} = 60\%$ is expected (Figure 4.13a). The relationship between the effective Young's modulus, Y', and solid fraction, of a metal foam follows one of the Gibson-Ashby scaling laws, $Y' = Y^{lig}\varphi^2$, with Y^{lig} denoting Young's modulus of the individual ligaments [231]. Upon continuous compression of NPG specimen to the larger deformations, solid fraction increases and therefore enhanced Y' values are observed as shown in Figure 4.14.

Contrary to the ductile NPG, NPG/PPy specimens are brittle and break at a deformation of 30 ~ 40%. Similar failure was also observed in the free-standing PPy films in tension as reported in Refs. [232, 233], which has been investigated from the aspects of the ionic crosslinking and microstructure. A cone-shaped structure has been found underneath the surface and cracks proceed around the cones or nodule boundaries [233]. It is also argued that the ionic crosslinking between charged polymer chains and counterions induce brittleness in the polymer [232]. The crosslinking can restrict the molecules movements and thus impede the yielding of PPy. In this work, electropolymerization experiments are performed under 0.8 V (vs. commercial Ag/AgCl electrode) and the as-synthesized PPy coatings are under oxidation state with counterion (ClO_4^-) incorporated so that ionic crosslinking is expected [215, 234].

5.4 Phenomenological description of tunable elasticity

During cyclic potential sweeps of NPG/PPy hybrids, the reversible variation in the material's elastic modulus, $\Delta Y'$, has been observed for the first time. The maximum amplitude of the relative modulus variation, $\hat{y}$, of NPG/PPy hybrids with ligament size L_D ~ 160 nm and PPy thickness t_{PPy} ~ 40 nm reaches 3%, which shows a 6-fold increase in comparison to that (0.5%) of bare NPG in the same potential range (Figure 4.17c). More strikingly, when the NPG/PPy hybrid is oxidized, the elasticity shows a non-monotonic behavior, which is in contrast to the linear actuation. At the

beginning of the oxidation stage, NPG/PPy hybrids gradually stiffen until the middle of the investigated potential range (~ 0.6 V for the potential window of 0.4 ~ 0.8 V). This is followed by softening as the polymer oxidation proceeds (Figures 4.16c and d). Yet, $\Delta Y'$ at 0.8 V does not attain its magnitude at the initial state at 0.4 V (Figures 4.16c, d, and 4.18b). When the material is reduced, an opposite behavior is found. This non-linear $\Delta Y'$ behavior is reproducible over all investigated potential cycles (Figure 4.15), with an upward drift of Y' during the measurement. Irrespective of Y' drift, the amplitude of the $\Delta Y'$ of each CV cycle is not affected. The slow increase of Y' can be attributed to the gradually irreversibly plastic deformation of the specimen under the testing load. Since the amplitude of the elastic modulus variation strongly correlates with PPy thickness of NPG/PPy (Figure 4.17b), it is suggested that the reversible non-linear $\Delta Y'$ is related to the redox reactions in PPy bulk.

According to the conductive zone propagation theory [235, 236], when PPy film is electrochemically oxidized, the side of the film attached to the metal electrode substrate becomes conductive first. Next, the conductive front propagates to the side exposed to the electrolyte. In other words, when the potential positively sweeps, NPG, serving as a substrate, is positively charged first and the PPy at NPG/PPy interface initially becomes conductive. It has been reported that when NPG is positively charged at the potential regime of 0.4 ~ 0.8 V vs. SHE, the elastic modulus of NPG continuously decreases [21]. It is thus to expect the competition between the descending modulus of NPG and the ascending modulus of PPy as reported in studies on elastic properties of PPy [32, 34, 35, 237], at least at the initial stage of electrochemically oxidizing the NPG/PPy. However, an entirely opposite elastic modulus behavior is observed for NPG/PPy with negligibly small PPy thickness around 1 nm (Figure 4.16b). In addition, the electro-chemo-mechanical coupling of planar Au/PPy electroactuators within a potential range of 0.4 ~ 0.8 V in 1 M $HClO_4$ was explored [142]. It has been reported that the potential is screened within PPy film and the change in electrode potential does not impact the space charge region at the Au-PPy interface. Therefore, charging of the gold surface will not contribute to the changes in the elastic modulus of NPG/PPy. It is therefore assumed that the non-monotonous variation of $\Delta Y'$ observed in NPG/PPy hybrids are caused by the electrochemical processes in the PPy film. This assumption is also supported by the linear dependence of $\hat{Y}$ and $\hat{y}$ on the PPy volume fraction, φ_{PPy} (Figures 4.17b and c).

Although the effect of Au/PPy interface on the elastic behavior has been ruled out, the difference in the linear ε - E_{SHE} (or ε - Δq_{V}, Figures 4.16o, p, and Figure 4.18h) and the non-linear $\Delta Y'$ - E_{SHE} (or $\Delta Y'$ - Δq_{V}, Figures 4.16c, d, and Figure 4.18b) suggests that the doping/dedoping processes induced volume changes are not capable to thoroughly clarify the complex elastic modulus behavior.

The elastic modulus behavior of free-standing PPy films or PPy-covered planar electroactuators upon electrochemical redox reactions have been studied [32, 33, 35–37, 103, 112]. However, the mechanism of the stiffness dependence on the electrochemical oxidation of the polymer has not been fully clarified so far. The mechanical behavior of the PPy films will be influenced by several factors, including electropolymerization conditions (e.g., temperature, electrode potential, and types of solvents and counterions [9, 11, 113, 238]), sample geometries [144, 223], and the testing environments (e.g., potential regime, type of anions in the electrolyte, and loading conditions [32, 33, 35–37, 103, 112, 232, 238, 239]). These factors can result in specimens with diverse mechanical behavior. For example, it has been reported that Young's modulus of ClO_4^- doped PPy

increases under oxidation in $LiClO_4$ aqueous electrolyte [32]. However, when PF_6^- doped PPy films is oxidized in $NaPF_6$ aqueous electrolyte and tetrabutylammonium hexafluorophosphate - propylene carbonate (TBAPF6/PC) anhydrous electrolyte, the corresponding Young's modulus decreases [33, 37].

It has been hypothesized that the observed electrochemically modulated modulus behavior is influenced by several effects in CPs during electrochemical redox processes in the electrolyte. Upon oxidation, the polymer chains stretch and the degree of freedom of the chains decreases, leading to a rise of the elastic modulus [32]. Meanwhile, the positively charged polymer chains interact with the incorporated hydrated anions, forming crosslinks, resulting in the enhancement of modulus [34, 35, 237]. On the other hand, penetration of hydrated ions and the free water into the polymer network reduces the density of the crosslinks and softens the polymer, resulting in the reduced modulus [9, 33, 37, 38, 112].

In the present thesis, the very same processes might be responsible for the tunable stiffness of NPG/PPy as well. Thus, the competition between the stiffening and softening of PPy results in the non-monotonous variation of modulus of NPG/PPy hybrids. At the initial oxidation stage, the chain stiffening and formation of the ionic crosslinking predominate, leading to an increase in $\Delta Y'$ of NPG/PPy hybrids. As the oxidation proceeds, the continuous ingress of hydrated anions and free water will induce a more pronounced softening effect. At the later oxidation stage, the softening effect outweighs the stiffening effect, resulting in the decrease of the NPG/PPy hybrids modulus. On the other hand, during the initial stage of the reduction process, the anions and solvent are repelled, the softening effect is reduced, promoting the modulus increase. Afterwards, at the lower potential range, the continuous loss of anions and crosslinking will soften the polymer chains, resulting in the observed decrease of $\Delta Y'$.

The synergetic effect between stiffening and softening effects can be verified by the findings in the sections 4.6.2 ~ 4.6.3. At the scan rate, v, of 5 mV/s (section 4.6.2.1), a macroscopic actuation strain of ~ 0.028% of NPG/PPy(35 nm) is detected, which is ~ 1/3 of that (~ 0.08%) obtained at 0.2 mV/s (Figures 4.18g and h). The linear dependence of current density, j_V, on v of NPG/PPy(35 nm) (Figure 4.11b) indicates that at $v \leq 5$ mV/s the CV time is sufficient for electrolyte diffusion from the bulk electrolyte into the interior of a specimen and implies that the electrochemical redox throughout the specimen is uniform. The smaller actuation strain at higher v originates from less hydrated anions and free water involved during the short CV time [107]. Under such a circumstance, the softening effect might be negligibly small and outweighed by the stiffening effect, resulting in the linear $\Delta Y'$ - E_{SHE} (Figure 4.18a). While at 0.2 mV/s, more hydrated anions and free water are incorporated during the cycling time, leading to the stronger softening effect and provoking the stiffening-softening phenomena at the overall potential range (Figure 4.18b).

When *in situ* DMA measurements are performed in different potential regimes (section 4.6.2.2), as has been shown in Figure 4.20d, NPG/PPy hybrids are at various oxidation statuses with different amounts of charge and hydrated anions involved. At the smallest potential window (0.6 ~ 0.8 V, Figure 4.20c), $\Delta Y'$ first increases with Δq_V until ~5 mC/mm^3, followed by an invariance of $\Delta Y'$ until ~ 10mC/mm^3. This can also be explained by the stiffening-softening competition. At the initial oxidation stage, few hydrated anions are absorbed into PPy, the stiffening effect predominates; when oxidation proceeds, hydrated anions and free water are progressively incorporated, whereas the softening effect is relatively weak (due to the small Δq_V) and it might be

counteracted by the stiffening effect, leading to an equilibrium in the stiffness, namely, the invariant $\Delta Y'$ vs. Δq_V. When larger potential windows were applied, the softening effect exceeds the stiffening effect, and in the biggest potential window (0 ~ 0.8 V), $\Delta Y'$ exhibits the largest decrease at the later oxidation stage (Figure 4.20c).

The softening effect caused by water is examined via performing *in situ* DMA analysis in anhydrous PC electrolyte (section 4.6.3). Since the large size of the PC molecule, only ClO_4^- anions are absorbed into PPy during oxidation [33]. The linear $\Delta Y'$ - E_{SHE} and $\Delta Y'$ - Δq_V curves (Figures 4.22b and d) imply the effect of H_2O molecules on the softening effect, which consequentially results in non-monotonous $\Delta Y'$ obtained in aqueous $HClO_4$. As has been revealed [7, 185–187], H_2O molecules exists in the form of solvation shell outside counteranion as well as free water, and the amount of free water is more than that of water in the solvation shell. It has been reported that the solvation shell directly associated with counteranion is inserted into PPy matrix at a faster speed during oxidation, whereas the free water molecules are moved into PPy by osmotic effect much more slowly [7]. At a higher actuation frequency, namely, at a faster scan rate (i.e. 5 mV/s) and in a smaller potential window (i.e. 0.6 ~ 0.8 V), the cycling time is too short and the insertion of hydrated ClO_4^- predominates in comparison with free water, giving rise to smaller $\hat{\varepsilon}$, $\hat{Y}$, and $\Delta Y'_{de}$ (Figures 4.19a and 4.20e). At a smaller actuation frequency, that is at a slower sweep speed (i.e. 2 mV/s and 0.2 mV/s) and in a wider potential regime (i.e. 0.4 ~ 0.8 V, 0.2 ~ 0.8 V, and 0 ~ 0.8 V), the cycling time is long enough for the insertion of both hydrated ClO_4^- and free water, producing much larger $\hat{\varepsilon}$, $\hat{Y}$, and $\Delta Y'_{de}$ as shown in Figures 4.19a and 4.20e. The difference in the linear $\Delta Y'$ - E_{SHE} in 0.4 ~ 0.8 V at 5 mV/s (Figure 4.18a), the essentially invariant $\Delta Y'$ in 0.7 ~ 0.8 V at 2 mV/s (Figure 4.20b), the non-monotonous $\Delta Y'$ - E_{SHE} in 0.4 ~ 0.8 V at 2 mV/s (Figures 4.16c and d), and the non-linear $\Delta Y'$ - E_{SHE} in the wider potential regimes at 2 mV/s (Figure 4.20b) suggests the considerable effect of free water induced by osmotic process on the softening of NPG/PPy hybrids.

5.5 Quantitative description of elasticity

As described in section 2.6, Larché-Cahn theory accounts for the relationship between chemical composition and mechanics of crystalline materials under mechanical stress conditions. The concept of open elasticity was adopted in this work as an approach to clarify that. This theory was experimentally verified by studying the elasticity and behavior of hydrogen content in bulk nanoporous (np) Pd-H and Pd-Au-H under dynamic stress [76] (section 2.6).

The insertion of hydrogen into np Pd lattice is similar to the scenario of incorporating ClO_4^- into PPy matrix, therefore, an attempt has been made to explain the changes in Young's modulus of NPG/PPy hybrids using Larché-Cahn theory. The concept of open-system compliance was adopted in this work as an approach to clarify the experimentally revealed compliance variation of NPG/PPy under dopants exchange in the polymer. The calculation of the experimental compliance variation is based on the data from the *in situ* DMA experiment conducted with NPG/PPy (35 nm) at a scan rate of 0.2 mV/s (section 4.6.2.1). The diffusion coefficient, D_s, of ClO_4^- in PPy matrix is ~ 10^{-13} m^2/s [218]. The diffusion time, $t \sim l^2/2D$, where l is the diffusion distance (35 nm, for the PPy film), for the diffusion path is around 6 ms. Thus, at a scan rate of 0.2 mV/s, the doping specimen ClO_4^- is regarded to be in equilibrium under a constant

potential.

The doping level (amount of ClO_4^- per pyrrole unit, $x_{ClO_4^-}$) is assessed as follows [6, 37]:

$$x_{ClO_4^-} = \frac{2q_{red}}{q_{poly} - q_{red}} \tag{5.1}$$

where $q_{poly} = 1.19$ C is the polymerization charge and q_{red} is the reduction charge in Figure 4.18d. Doping level ranging from 0 to 0.05 in the applied potential window is obtained.

The concentration-strain coefficient, η, is determined according to:

$$\eta = \frac{\varepsilon}{x_{ClO_4^-}} \tag{5.2}$$

where ε is the strain (Figure 4.18h). The concentration-strain coefficient for the strain obtained at 0.2 mV/s is 2.118.

The solute fraction, χ, is evaluated as:

$$\chi = \frac{1}{\rho}\frac{dx_{ClO_4^-}}{d\mu}|_{stress} \tag{5.3}$$

where ρ is the volumetric density of sites of ClO_4^- in the ClO_4^- doped NPG/PPy. Based on the ideal PPy chain network in section 2.2.1, assuming one pyrrole monomer in PPy monoclinic unit cell, $1/\rho$ is 9.8624×10^{-4} m^3mol^{-1}. μ is the chemical potential of ClO_4^- and follows:

$$\mu = \mu_0 + RT\ln x_{ClO_4^-} \tag{5.4}$$

where μ_0 is the chemical potential of pure species, R is the molar gas constant, and T is temperature. When substituting Eq. 5.4 into Eq. 5.3, one gets:

$$\chi = \frac{1}{\rho}\frac{x_{ClO_4^-}}{RT}|_{stress} \tag{5.5}$$

Substituting χ and η into Eq. 2.12, the theoretical relative compliance is obtained.

Figure 5.1 depicts the experimental relative compliance, Δs_{exp}, and theoretical relative compliance, Δs_{th}, of NPG/PPy(35 nm) as a function of ClO_4^- fraction. It is seen that Δs_{exp} and Δs_{th} exhibit a big difference in magnitude. Moreover, Δs_{th} increases with $x_{ClO_4^-}$ (inset figure in Figure 5.1), whereas Δs_{exp} first decreases up to doping level $x_{ClO_4^-} = 0.02$, followed by rapidly increases upon further incorporation of ClO_4^-. The increase of Δs_{exp} at the more composition scale of 0.02 ~ 0.05 indicates the compatibility of Larché-Cahn theory. In other words, the diffusion of ClO_4^- in PPy matrix under stress will induce the elastic modulus decrease of NPG/PPy. The large difference in the magnitude of Δs_{exp} and Δs_{th} might be due to the insertion of hydrated and free water as accounted in section 5.4. However, at the smaller composition below 0.02, the chain stiffening and the formation of crosslinking caused by charging and incorporation of ClO_4^- might be stronger than the softening caused by ClO_4^- insertion, consequently giving rise to the Δs_{exp} decrease at $x_{ClO_4^-} < 0.02$.

Overall, irrespective of the exact mechanism, NPG/PPy electroactuators exhibit elasticity change in response to the electrochemical conditions. Because the variation of elasticity will also contribute to the strain of an actuator, it is possible to distinguish the contributions of modulus variation to the total actuation strain.

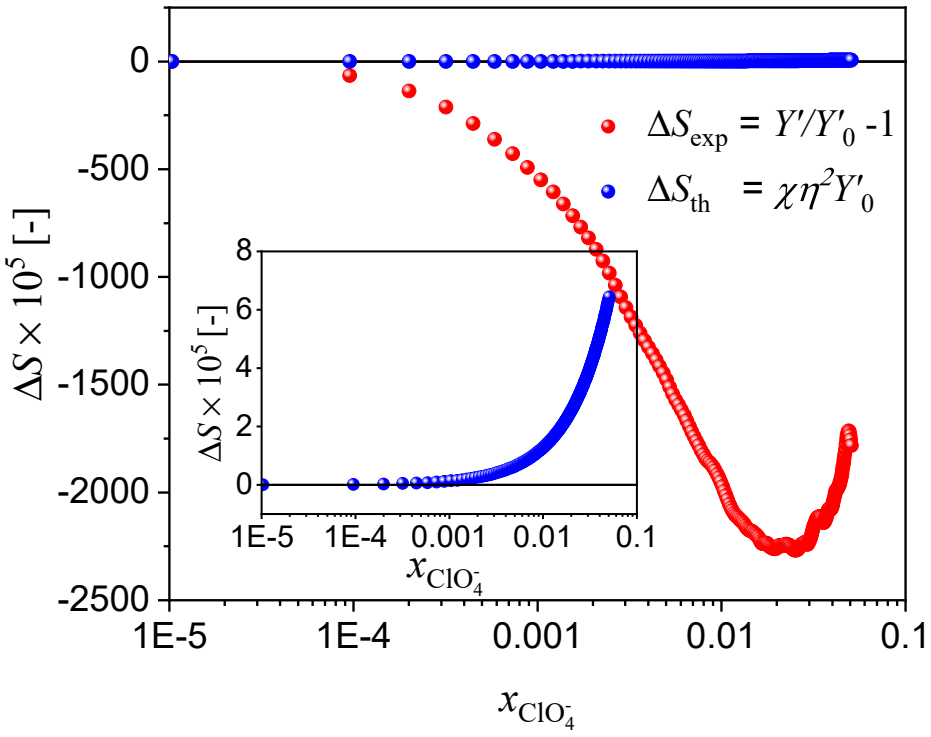

Figure 5.1. Anodic branch of experimental relative compliance (red), Δs_{exp}, and theoretical relative compliance (blue), Δs_{th}, of NPG/PPy(35 nm) as a function of ClO_4^- fraction at a scan rate of 0.2 mV/s in 0.1 M $HClO_4$ under DMA frequencies of 1 Hz. The inset figure shows the theoretical relative compliance at a higher magnification.

5.6 Actuation under load

In practical applications, the actuators always work under a load. It is, therefore, crucial to study the performance of an electroactuator against the load.

The actuation behavior of PPy films under loads has been studied and it has been found that actuation strain decreases with the external load [1, 14, 38, 103, 189, 222, 223]. The load-dependent strain is related to the polymer chain alignment [189]. In a stretched highly chain-oriented polymer, the electrochemical doping and dedoping processes are much slower than those in unoriented polymers. However, it is difficult to quantitatively determine the orientation of the chains in polymer, which strongly depends on the synthesis parameters (section 2.2.2). In addition, some investigations have found that most of the chains are not oriented at all even though under large deformations [240].

As accounted in section 2.5.2, actuation strain is composed of two parts: 1) strain induced by electrochemical oxidation and reduction, $\delta\varepsilon_0$; 2) strain caused by the change in Young's modulus, $-\frac{\sigma}{Y'^2}\delta Y'$, which is also related to the applied load, σ. Note that in this thesis specimens were tested in compression, so the σ values are negative. If $\delta Y'$ is positive, the term $-\frac{\sigma}{Y'^2}\delta Y'$ is positive as well. In other words, stiffening of the material will contribute an expansion to the actuation strain. While $\delta Y'$ is negative, the modulus variation will contribute a contraction to the actuation strain. Whereas $\delta\varepsilon_0$ simply depends on the electrochemical process. The incorporation of ClO_4^- into PPy matrix during oxidation gives rise to expansion and a positive $\delta\varepsilon_0$ value; the repulsion of ClO_4^- from PPy matrix during reduction causes contraction and a negative

$\delta\varepsilon_0$ value.

In this thesis, studies of actuation under loads are carried out at cyclic potential sweeps, which consecutively changes oxidation and reduction states (section 4.7.2). For as-synthesized NPG/PPy specimens, oxidation will lead to an expansion while reduction will give rise to a contraction to the total actuation. In dilatometer, the load is negligibly small and the variation of Young's modulus does not contribute to total strain, therefore, the strain obtained in dilatometer is smaller than those obtained from DMA.

When potential sweeps at a relatively small scan rate, the oxidation status in PPy matrix is gradually changed and so is the variation of Young's modulus. The non-linear $\Delta Y' - E_{\mathrm{SHE}}$ curves are used to determine the contribution of modulus variation to total strain at any oxidation status. At ~ 0.6 V, the maximum contribution of modulus variation to total actuation will be obtained, and it is found to vary from ~ 16% to ~ 60% under external load ranging from -2 to -10 MPa. Since the total actuation is found to be invariant with load, the corresponding contribution of electrochemical redox – as has been assumed so far – to total actuation at ~ 0.6 V decreases from ~ 74% to ~ 40%. However, it is inconsistent with the superimposed $\Delta q_{\mathrm{V}} - \mathrm{t}$ curves (Figure 4.25c) under the loads. This leaves an open question to be solved.

Chapter 6

Summary and Outlook

6.1 Summary

In this thesis, mm-scaled NPG/PPy hybrids are synthesized by electropolymerizing PPy coatings on NPG specimens produced by electrochemical dealloying of mm-sized $Ag_{75}Au_{25}$ cylinders. Annealing as-dealloyed NPG in the air is a facial way to get a monolithic network of coarsened ligaments and pores. Electropolymerization charge densities are carefully monitored to produce PPy films with desired thicknesses during the pulse electropolymerization processes. Elaborate PPy thicknesses are chosen so as to not entirely block the pores which provide the pathway for the flow of $HClO_4$. The good mechanical strength, the uniform bicontinuous network, and the facial preparation foreordain NPG/PPy as a good alternative of NPG for the study of electro-chemo-mechanical properties and function (e.g., actuation).

This thesis explores the strength of NPG/PPy. NPG/PPy hybrids exhibit higher strength in contrast to bare NPG. With the increasing of PPy thickness, the strength of NPG/PPy increases accordingly. At a deformation of ~ 30%, the high strengths of ~ 30, ~ 40, and ~ 60 MPa for NPG/PPy(10 nm), NPG/PPy(20 nm), and NPG/PPy(30 nm) suggest the promise of NPG/PPy hybrids in practical application.

Besides, the elastic modulus and actuation behavior of NPG/PPy hybrids, the main target in this thesis, are explored using *in situ* DMA under electrochemical control in $HClO_4$ at a scan rate of ≤ 2 mV/s. Within the applied potential regime of 0.4 ~ 0.8 V, a non-linear change in the effective elastic modulus ($\Delta Y'$) is found for the first time in contrast to the linear actuation behavior. At the initial stage of oxidation, the NPG/PPy hybrids stiffen, followed by softening at a further oxidation stage. $\Delta Y'$ strongly depends on PPy film thickness, showing a 7-fold increase at maximum thickness as compared to the non-coated NPG. It is striking that for the thinnest PPy film (~ 1 nm), the modulus behavior is inverted in comparison to the non-coated NPG. The peak-to-peak amplitudes of actuation strain and the relative variation of modulus also show a linear dependence on PPy thickness, respectively exhibiting ~ 14-fold and 5-fold increase at maximum thickness as compared to the non-coated NPG. These findings apparently imply the dominant impact of process in PPy matrix during doping and de-doping on the non-monotonous stiffness response. At a relatively higher content (>0.02) of incorporated anions, the same trend of experimental and theoretical compliance suggests that the diffusion of hydrated anions among the PPy matrix under stress might also contribute to the decrease of modulus of NPG/PPy hybrids. When incorporated

specimens is < 0.02, Larché-Cahn theory is not able to explain the modulus increase at the early oxidation stage, suggesting that the interactions between polymer chains and incorporated specimens in PPy matrix play a strong role in stiffening NPG/PPy.

The interactions between the charged polymer chains and the dopant anions will form crosslinks, thus stiffening the hybrid. However, the incorporation of the hydrated anions and water will induce a softening of the polymer. The water molecules are regarded to exist in form of solvation shells that move with anions and free water driven by osmotic pressure. The linear $\Delta Y'$ - E_{SHE} obtained at a relatively faster scan rate of 5 mV/s and the invariant $\Delta Y'$ - E_{SHE} obtained at 0.7 ~ 0.8 V at 2 mV/s suggest the more pronounced role of free water in softening PPy in contrast to the solvation shell. The competition between the stiffening and the softening will lead to the complex, non-linear modulus behavior. The major efforts from both experiment and simulation are required to confirm the suggested impact of the changes in PPy structure upon the redox reactions on the origin of the complex viscoelastic behavior.

The total actuation strains during potential sweeps have been found to be invariant under the increasing load, suggesting the capability for NPG/PPy electroactuator to work against load, implying promising application of NPG/PPy hybrids as electroactuators. The present results on $\Delta Y'$ - E_{SHE} relationships and $\Delta Y'$ - Δq_{V} enable one to distinguish the strain contribution from the modulus variation. An increase in $\Delta Y'$ will contribute an expansion to the net strain of the actuation. With the compressive load increasing from 2 to 10 MPa, the maximum contribution of modulus change to total strain increases from ~ 16% to ~ 60%. Thus, from a fundamental point of view, studying the elastic modulus behavior promotes understanding the actuation of NPG/PPy electroactuators.

6.2 Outlook

This thesis synthesizes NPG/PPy electroactuators and focuses on the electro-chemo-mechanical coupling of NPG/PPy hybrids. In addition to the observations in this thesis, one is led to several open questions in this thesis.

It has been reported that the densification induced by the load will lead to the connecting of the neighboring PPy coated ligaments [30], and the 'bridges' between neighboring ligaments will contribute to the strain. However, the almost same strain - charge coefficients obtained from the superimposed $\varepsilon - \Delta q_{\mathrm{V}}$ curves (Figure 4.26e) imply that the 'bridge' notion in the studied NPG/PPy specimens in this thesis is not applicable. In this thesis, the mean diameter of the ligaments is of ~ 160 ± 40 nm, which is bigger than that (~ 120 ± 10 nm) reported in Ref. [30]. Meanwhile, the slightly smaller PPy thickness of ~ 36 ± 6 nm than that (~ 42 ± 1 nm [30]) might induce more space between the neighboring ligaments so that the 'bridge' notion is not applicable in this thesis. Ref. [30] also points out that if the neighboring ligaments do not connect, the expansion of the PPy normal to the ligaments surface will not contribute to the macroscopic volume change. As has been found in section 4.7, the macroscopic strain is independent of load, and after subtracting the contribution of modulus variation the rest strain part decreases from ~ 74 to ~ 40%. One will be headed to ask where is this strain from if the normal strain of PPy does not contribute to the macroscopic volume change? Indeed, the charging process will incorporate ClO_4^- into PPy matrix and induce macroscopic volume change. So, there might be a third effect coupled to

contribute to the actuation. Special attention should be paid to the large surface area, on which the surface stress might be generated during charging-discharging processes. To this end, the charge required for double layer charging and for anions diffusion should be precisely distinguished. Cyclic voltammograms obtained at various scan rates can be used to realize this purpose. Afterward, Eq. 2.8 could be developed by considering the effect of surface stress on the strain.

Besides, the fracture is observed for NPG/PPy(10 ~ 30 nm) at a deformation of ~ 30% (Figure 4.13). From a scientific point of view, it is interesting to inspect the sites where fracture initiates and how the fracture develops until the failure of the material. Compression or tension testing using *in situ* SEM or X-Ray tomography technique might work this out.

Moreover, as has been primarily revealed in Figure 4.23, upon potential jumping between 0.4 and 0.8 V, the specimen expands and shrinks according to its oxidation states. However, irrespective of the potential jumping of 0.4 → 0.8 V or 0.8 → 0.4 V, elastic modulus instantly drops at the moment potential switches, followed by a gradual increase at the rest duration of the potential step. The elastic modulus behavior under potential jump at different loads should be explored so as to understand the actuation of NPG/PPy actuators under various electrochemical conditions.

References

[1] W. Zheng, J.M. Razal, P.G. Whitten, R. OvalleRobles, G.G. Wallace, R.H. Baughman, and G.M. Spinks. Artificial muscles based on polypyrrole/carbon nanotube laminates. *Advanced Materials*, 23(26):2966–2970, 2011.

[2] T. Shoa, J.D. Madden, T. Mirfakhrai, G. Alici, G.M. Spinks, and G.G. Wallace. Electromechanical coupling in polypyrrole sensors and actuators. *Sensors and Actuators A: Physical*, 161(1-2):127–133, 2010.

[3] S. Hara, T. Zama, W. Takashima, and K. Kaneto. Tris(trifluoromethylsulfonyl)methide-doped polypyrrole as a conducting polymer actuator with large electrochemical strain. *Synthetic Metals*, 156(2): 351–355, 2006.

[4] G. Vázquez, T. Otero, and J.L. Cascales. Electro-chemo-mechanical response of a free-standing polypyrrole strip. In *Journal of Physics: Conference Series*, volume 127, page 012005. IOP Publishing, 2008.

[5] H. Kim, S.K. Ahn, D.M. Mackie, J. Kwon, S.H. Kim, C. Choi, Y.H. Moon, H.B. Lee, and S.H. Ko. Shape morphing smart 3D actuator materials for micro soft robot. *Materials Today*, 41:243–269, 2020.

[6] L. Bay, K. West, and S. Skaarup. Pentanol as co-surfactant in polypyrrole actuators. *Polymer*, 43(12):3527–3532, 2002.

[7] M.J. Jafeen, M.A. Careem, and S. Skaarup. Speed and strain of polypyrrole actuators: Dependence on cation hydration number. *Ionics*, 16(1):1–6, 2010.

[8] J.D. Madden, D. Rinderknecht, P.A. Anquetil, and I.W. Hunter. Creep and cycle life in polypyrrole actuators. *Sensors and Actuators A: Physical*, 133(1):210–217, 2007.

[9] O. Uzun, N. Baman, C. Alkan, U. Kölemen, and F. Ylmaz. Investigation of mechanical and creep properties of polypyrrole by depth-sensing indentation. *Polymer Bulletin*, 66(5):649–660, 2011.

[10] K. Kaneto, T. Shinonome, K. Tominaga, and W. Takashima. Electrochemical creeping and actuation of polypyrrole in ionic liquid. *Japanese Journal of Applied Physics*, 50(9R):091601, 2011.

[11] B.F. Cvetko, M.P. Brungs, R.P. Burford, and M. Skyllas-Kazacos. Structure, strength and electrical performance of conducting polypyrroles. *Journal of Materials Science*, 23(6):2102–2106, 1988.

[12] E. Chalmers, Y. Li, and X. Liu. Molecular tailoring to improve polypyrrole hydrogels' stiffness and electrochemical energy storage capacity. *Frontiers of Chemical Science and Engineering*, 13(4):684–694, 2019.

[13] S. Cuenot, S. Demoustier-Champagne, and B. Nysten. Elastic Modulus of Polypyrrole Nanotubes. *Physical Review Letters*, 85(8):1690–1693, 2000.

[14] G.M. Spinks, L. Liu, G.G. Wallace, and D. Zhou. Strain Response from Polypyrrole Actuators under Load. *Advanced Functional Materials*, 12(6-7):437–440, 2002.

[15] G.M. Spinks, V. Mottaghitalab, M. Bahrami-Samani, P.G. Whitten, and G.G. Wallace. Carbon-nanotube-reinforced polyaniline fibers for high-strength artificial muscles. *Advanced Materials*, 18(5):637–640, 2006.

[16] M. Lay, J.A. Mndez, M. Delgado-Aguilar, K.N. Bun, and F. Vilaseca. Strong and electrically conductive nanopaper from cellulose nanofibers and polypyrrole. *Carbohydrate Polymers*, 152:361–369, 2016.

[17] K. Tominaga, K. Hamai, B. Gupta, Y. Kudoh, W. Takashima, R. Prakash, and K. Kaneto. Suppression of electrochemical creep by cross-link in polypyrrole soft actuators. *Physics Procedia*, 14:143–146, 2011.

[18] F. Gao, N. Zhang, X. Fang, and M. Ma. Bioinspired Design of Strong, Tough, and Highly Conductive Polyol-Polypyrrole Composites for Flexible Electronics. *ACS Applied Materials* & Interfaces, 9(7):5692–5698, 2017.

[19] G. Han and G. Shi. Conducting polymer electrochemical actuator made of high-strength three-layered composite films of polythiophene and polypyrrole. *Sensors and Actuators B: Chemical*, 99(2-3):525–531, 2004.

[20] G.M. Spinks, B. Xi, V.T. Truong, and G.G. Wallace. Actuation behaviour of layered composites of polyaniline, carbon nanotubes and polypyrrole. *Synthetic Metals*, 151(1):85–91, 2005.

[21] N. Mameka, J. Markmann, H.J. Jin, and J. Weissmüller. Electrical stiffness modulation-confirming the impact of surface excess elasticity on the mechanics of nanomaterials. *Acta Materialia*, 76:272–280, 2014.

[22] T.J. Balk, C. Eberl, Y. Sun, K.J. Hemker, and D.S. Gianola. Tensile and compressive microspecimen testing of bulk nanoporous gold. *JOM*, 61(12):26, 2009.

[23] M. Bürckert, N.J. Briot, and T.J. Balk. Uniaxial compression testing of bulk nanoporous gold. *Philosophical Magazine*, 97(15):1157–1178, 2017.

[24] B.N.D. Ngô, A. Stukowski, N. Mameka, J. Markmann, K. Albe, and J. Weissmüller. Anomalous compliance and early yielding of nanoporous gold. *Acta Materialia*, 93:144–155, 2015.

[25] J. Biener, A.M. Hodge, A.V. Hamza, L.M. Hsiung, and J.H. Satcher Jr. Nanoporous Au: A high yield strength material. *Journal of Applied Physics*, 97(2):024301, 2005.

[26] L.Z. Liu, X.L. Ye, and H.J. Jin. Interpreting anomalous low-strength and low-stiffness of nanoporous gold: Quantification of network connectivity. *Acta Materialia*, 118:77–87, 2016.

[27] N.J. Briot, T. Kennerknecht, C. Eberl, and T.J. Balk. Mechanical properties of bulk single crystalline nanoporous gold investigated by millimetre-scale tension and compression testing. *Philosophical Magazine*, 94(8):847–866, 2014.

[28] H. Hirakata, K. Shimbara, T. Kondo, and K. Minoshima. Size effect on tensile creep behavior of micrometer-sized single-crystal gold. *Materialia*, 1:221–228, 2018.

[29] K. Wang, C. Stenner, and J. Weissmüller. A nanoporous gold-polypyrrole hybrid nanomaterial for actuation. *Sensors and Actuators B: Chemical*, 248:622–629, 2017.

[30] B. Roschning and J. Weissmüller. Nanoporous-Gold-Polypyrrole Hybrid Materials for Millimeter-Sized Free Standing Actuators. *Advanced Materials Interfaces*, 7(24):2001415, 2020.

[31] L.Z. Liu, N. Mameka, J. Markmann, H.J. Jin, and J. Weissmüller. Surface-driven actuation: Sign reversal under load and surface load-memory effect. *Physical Review Materials*, 3(6):066001, 2019.

[32] T.F. Otero, J.L. Cascales, and G.V. Arenas. Mechanical characterization of free-standing polypyrrole film. *Materials Science and Engineering: C*, 27(1):18–22, 2007.

[33] R.Z. Pytel, E.L. Thomas, and I.W. Hunter. In situ observation of dynamic elastic modulus in polypyrrole actuators. *Polymer*, 49(8):2008–2013, 2008.

[34] A. MacDiarmid, Y. Min, J. Wiesinger, E. Oh, E. Scherr, and A. Epstein. Towards optimization of electrical and mechanical properties of polyaniline: Is crosslinking between chains the key? *Synthetic Metals*, 55(2-3):753–760, 1993.

[35] S. Koehler, A. Bund, and I. Efimov. Shear moduli of anion and cation exchanging polypyrrole films. *Journal of Electroanalytical Chemistry*, 589(1):82–86, 2006.

[36] M. Bahrami-Samani, C.D. Cook, J.D. Madden, G.M. Spinks, and P.G. Whitten. Quartz crystal microbalance study of volume changes and modulus shift in electrochemically switched polypyrrole. *Thin Solid Films*, 516(9):2800–2807, 2008.

[37] T. Shoa, T. Mirfakhrai, and J.D.W. Madden. Electro-stiffening in polypyrrole films: Dependence of Young's modulus on oxidation state, load and frequency. *Synthetic Metals*, 160(11):1280–1286, 2010.

[38] E. Smela, W. Lu, and B.R. Mattes. Polyaniline actuators: Part 1. PANI (AMPS) in HCl. *Synthetic Metals*, 151(1):25–42, 2005.

[39] C. Stenner, L.H. Shao, N. Mameka, and J. Weissmüller. Piezoelectric Gold: Strong Charge-Load Response in a Metal-Based Hybrid Nanomaterial. *Advanced Functional Materials*, 26(28):5174–5181, 2016.

[40] E. Detsi, Z. Chen, W. Vellinga, P. Onck, and J.T.M. De Hosson. Actuating and sensing properties of nanoporous gold. *Journal of Nanoscience and Nanotechnology*, 12(6):4951–4955, 2012.

[41] C. Xu, J. Su, X. Xu, P. Liu, H. Zhao, F. Tian, and Y. Ding. Low temperature CO oxidation over unsupported nanoporous gold. *Journal of the American Chemical Society*, 129(1):42–43, 2007.

[42] T. Fujita, P.F. Guan, K. McKenna, X.Y. Lang, A. Hirata, L. Zhang, T. Tokunaga, S. Arai, Y. Yamamoto, N. Tanaka, Y. Ishikawa, N. Asao, Y. Yamamoto, J. Erlebacher, and M.W. Chen. Atomic origins of the high catalytic activity of nanoporous gold. *Nature Materials*, 11(9):775–780, 2012.

[43] P.P. Zhang, J.T.and Liu, H.Y. Ma, and Y. Ding. Nanostructured Porous Gold for Methanol Electro-Oxidation. *The Journal of Physical Chemistry C*, 111(28): 10382–10388, 2007.

[44] E. Seker, W.C. Shih, and K.J. Stine. Nanoporous metals by alloy corrosion: Bioanalytical and biomedical applications. *MRS Bulletin*, 43(1):49–56, 2018.

[45] P. Daggumati, Z. Matharu, and E. Seker. Effect of Nanoporous Gold Thin Film Morphology on Electrochemical DNA Sensing. *Analytical Chemistry*, 87(16): 8149–8156, 2015.

[46] S.I. Kim, S.W. Kim, K. Jung, J.B. Kim, and J.H. Jang. Ideal nanoporous gold based supercapacitors with theoretical capacitance and high energy/power density. *Nano Energy*, 24:17–24, 2016.

[47] L.Y. Chen, J.L. Kang, Y. Hou, P. Liu, T. Fujita, A. Hirata, and M.W. Chen. High-energy-density nonaqueous MnO2@nanoporous gold based supercapacitors. *Journal of Materials Chemistry A*, 1(32):9202–9207, 2013.

[48] X.Y. Lang, A. Hirata, T. Fujita, and M.W. Chen. Nanoporous metal/oxide hybrid electrodes for electrochemical supercapacitors. *Nature Nanotechnology*, 6 (4):232–236, 2011.

[49] J. Weissmüller, R.N. Viswanath, D. Kramer, P. Zimmer, R. Würschum, and H. Gleiter. Charge-induced reversible strain in a metal. *Science*, 300(5617): 312–315, 2003.

[50] D. Kramer, R.N. Viswanath, and J. Weissmüller. Surface-Stress Induced Macroscopic Bending of Nanoporous Gold Cantilevers. *Nano Letters*, 4(5):793–796, 2004.

[51] H.J. Jin, S. Parida, D. Kramer, and J. Weissmüller. Sign-inverted surface stress-charge response in nanoporous gold. *Surface Science*, 602(23):3588–3594, 2008.

[52] H.J. Jin, X.L. Wang, S. Parida, K. Wang, M. Seo, and J. Weissmüller. Nanoporous Au-Pt alloys as large strain electrochemical actuators. *Nano Letters*, 10(1):187–194, 2010.

[53] Z. Han, Z. Qi, Q. Wei, Q. Deng, and K. Wang. The Mechanical Effect of MnO2 Layers on Electrochemical Actuation Performance of Nanoporous Gold. *Nanomaterials*, 10(10):2056, 2020.

[54] J. Biener, A. Wittstock, L. Zepeda-Ruiz, M. Biener, V. Zielasek, D. Kramer, R. Viswanath, J. Weissmüller, M. Bäumer, and A. Hamza. Surface-chemistry-driven actuation in nanoporous gold. *Nature Materials*, 8(1):47–51, 2009.

[55] E. Detsi, M.S. Selles, P.R. Onck, and J.T.M. De Hosson. Nanoporous silver as electrochemical actuator. *Scripta Materialia*, 69(2):195–198, 2013.

[56] S. Shi, J. Markmann, and J. Weissmüller. Actuation by hydrogen electrosorption in hierarchical nanoporous palladium. *Philosophical Magazine*, 97(19):1571–1587, 2017.

[57] C.L. Liao, C. Chu, K.Z. Fung, and I.C. Leu. Fabrication of nanoporous metal electrode by two-step replication technique. *Journal of Alloys and Compounds*, 441(1-2):L1–L6, 2007.

[58] Y. Kang, B. Jiang, Z.A. Alothman, A.Y. Badjah, M. Naushad, M. Habila, S. Wabaidur, J. Henzie, H. Li, and Y. Yamauchi. Mesoporous PtCu alloy nanoparticles with tunable compositions and particles sizes using diblock copolymer micelle templates. *Chemistry - A European Journal*, 25(1):343–348, 2019.

[59] S. Tang, S. Vongehr, Y. Wang, J. Cui, X. Wang, and X. Meng. Versatile synthesis of high surface area multi-metallic nanosponges allowing control over nanostructure and alloying for catalysis and SERS detection. *Journal of Materials Chemistry A*, 2(10):3648–3660, 2014.

[60] C. Wang and Q. Chen. Reduction-Induced Decomposition: Spontaneous Formation of Monolithic Nanoporous Metals of Tunable Structural Hierarchy and Porosity. *Chemistry of Materials*, 30(11):3894–3900, 2018.

[61] W. Yang, X.G. Zheng, S.G. Wang, and H.J. Jin. Nanoporous aluminum by galvanic replacement: Dealloying and inward-growth plating. *Journal of The Electrochemical Society*, 165(9):C492, 2018.

[62] I. McCue, A. Karma, and J. Erlebacher. Pattern formation during electrochemical and liquid metal dealloying. *MRS Bulletin*, 43(1):27, 2018.

[63] Z. Lu, C. Li, J. Han, F. Zhang, P. Liu, H. Wang, Z. Wang, C. Cheng, L. Chen, A. Hirata, T. Fujita, J. Erlebacher, and M. Chen. Three-dimensional bicontinuous nanoporous materials by vapor phase dealloying. *Nature Communications*, 9(1): 276, 2018.

[64] J. Erlebacher, M.J. Aziz, A. Karma, N. Dimitrov, and K. Sieradzki. Evolution of nanoporosity in dealloying. *Nature*, 410(6827):450–453, 2001.

[65] J. Weissmüller, R.C. Newman, H.J. Jin, A.M. Hodge, and J.W. Kysar. Nanoporous metals by alloy corrosion: Formation and mechanical properties. *MRS Bulletin*, 34(8):577–586, 2009.

[66] Z.H. Zhang, Y. Wang, Z. Qi, W.H. Zhang, J.Y. Qin, and J. Frenzel. Generalized fabrication of nanoporous metals (Au, Pd, Pt, Ag, and Cu) through chemical dealloying. *The Journal of Physical Chemistry C*, 113(29):12629–12636, 2009.

[67] Y. Ding, Y.J. Kim, and J. Erlebacher. Nanoporous gold leaf:"Ancient technology"/advanced material. *Advanced Materials*, 16(21):1897–1900, 2004.

[68] X. Zou, Y. He, P. Sun, J. Zhao, and G. Cui. A novel dealloying strategy for fabricating nanoporous silver as an electrocatalyst for hydrogen peroxide detection. *Applied Surface Science*, 447:542–547, 2018.

[69] J. Yu, Y. Ding, C. Xu, A. Inoue, T. Sakurai, and M. Chen. Nanoporous Metals by Dealloying Multicomponent Metallic Glasses. *Chemistry of Materials*, 20(14): 4548–4550, 2008.

[70] H.J. Jin, L. Kurmanaeva, J. Schmauch, H. Rösner, Y. Ivanisenko, and J. Weissmüller. Deforming nanoporous metal: Role of lattice coherency. *Acta Materialia*, 57(9):2665–2672, 2009.

[71] H.J. Jin and J. Weissmüller. A material with electrically tunable strength and flow stress. *Science*, 332(6034):1179–1182, 2011.

[72] K. Wang and J. Weissmüller. Composites of Nanoporous Gold and Polymer. *Advanced Materials*, 25(9):1280–1284, 2013.

[73] J. Biener, A. Wittstock, T.F. Baumann, J. Weissmüller, M. Bäumer, and A.V. Hamza. Surface chemistry in nanoscale materials. *Materials*, 2(4):2404–2428, 2009.

[74] R.H. Baughman, C. Cui, A.A. Zakhidov, Z. Iqbal, J.N. Barisci, G.M. Spinks, G.G. Wallace, A. Mazzoldi, D. De Rossi, A.G. Rinzler, O. Jaschinski, S. Roth, and M. Kertesz. Carbon Nanotube Actuators. *Science*, 284(5418):1340, 1999.

[75] Z. Luo, W. Gao, and C. Song. Design of multi-phase piezoelectric actuators. *Journal of Intelligent Material Systems and Structures*, 21(18):1851–1865, 2010.

[76] S. Shi, J. Markmann, and J. Weissmüller. Verifying Larché-Cahn elasticity, a milestone of 20th-century thermodynamics. *Proceedings of the National Academy of Sciences*, 115(43):10914–10919, 2018.

[77] J. Zhang, Y. Wang, C.H. Si, Q.G. Bai, W.S. Ma, H. Gao, and Z.H. Zhang. Electrochemical actuation behaviors of bulk nanoporous palladium in acid and alkaline solutions. *Electrochimica Acta*, 220:91–97, 2016.

[78] X. Li, M. Liu, B. Huang, H. Liu, W. Hu, L.H. Shao, and Z.L. Wang. Nanoporous-gold-based hybrid cantilevered actuator dealloyed and driven by a modified rotary triboelectric nanogenerator. *Scientific Reports*, 6(1):1–8, 2016.

[79] X.L. Ye, F. Liu, and H.J. Jin. Electrochemical Actuation of Nanoporous Gold Deformed by Compression. *Acta Metallurgica Sinica*, 50(2):252–258, 2014.

[80] E. Detsi, S. Punzhin, J. Rao, P.R. Onck, and J.T.M. De Hosson. Enhanced Strain in Functional Nanoporous Gold with a Dual Microscopic Length Scale Structure. *ACS Nano*, 6(5):3734–3744, 2012.

[81] E. Detsi, P. Onck, and J.T.M. De Hosson. Metallic Muscles at Work: High Rate Actuation in Nanoporous Gold/Polyaniline Composites. *ACS Nano*, 7(5): 4299–4306, 2013.

[82] L.H. Qian and M.W. Chen. Ultrafine nanoporous gold by low-temperature dealloying and kinetics of nanopore formation. *Applied Physics Letters*, 91(8):083105, 2007.

[83] X.L. Ye, N. Lu, X.J. Li, K. Du, J. Tan, and H.J. Jin. Primary and secondary dealloying of Au (Pt)-Ag: Structural and compositional evolutions, and volume shrinkage. *Journal of The Electrochemical Society*, 161(12):C517, 2014.

[84] Y.K. Cao, X.Y. Ma, Y.Z. Chen, G.B. Shan, and F. Liu. Size effect of ligaments on charge induced surface stress response of nanoporous Pd prepared by dealloying. *Scripta Materialia*, 123:1–4, 2016.

[85] H. Shirakawa, E.J. Louis, A.G. MacDiarmid, C.K. Chiang, and A.J. Heeger. Synthesis of electrically conducting organic polymers: Halogen derivatives of polyacetylene, (CH)x. *Journal of the Chemical Society, Chemical Communications*, 16:578–580, 1977.

[86] L. Zhang, S. Liu, H. Han, Y. Zhou, S. Hu, C. He, and Q. Yan. Studies on the formation process and anti-corrosion performance of polypyrrole film deposited on the surface of Q235 steel by an electrochemical method. *Surface and Coatings Technology*, 341:95–102, 2018.

[87] F.H. Meng and Y. Ding. Sub-Micrometer-Thick All-Solid-State Supercapacitors with High Power and Energy Densities. *Advanced Materials*, 23(35):4098–4102, 2011.

[88] X.X. Yuan, X.L. Ding, C.Y. Wang, and Z.F. Ma. Use of polypyrrole in catalysts for low temperature fuel cells. *Energy* & Environmental Science, 6(4):1105–1124, 2013.

[89] M. Sharma, G.I.N. Waterhouse, S.W.C. Loader, S. Garg, and D. Svirskis. High surface area polypyrrole scaffolds for tunable drug delivery. *International Journal of Pharmaceutics*, 443(1):163–168, 2013.

[90] S. Machida, S. Miyata, and A. Techagumpuch. Chemical synthesis of highly electrically conductive polypyrrole. *Synthetic Metals*, 31(3):311–318, 1989.

[91] D.P. Dubal, S.H. Lee, J.G. Kim, W.B. Kim, and C.D. Lokhande. Porous polypyrrole clusters prepared by electropolymerization for a high performance supercapacitor. *Journal of Materials Chemistry*, 22(7):3044–3052, 2012.

[92] X. Du, X. Hao, Z. Wang, X. Ma, G. Guan, A. Abuliti, G. Ma, and S. Liu. Highly stable polypyrrole film prepared by unipolar pulse electro-polymerization method as electrode for electrochemical supercapacitor. *Synthetic Metals*, 175:138–145, 2013.

[93] A. Davies, P. Audette, B. Farrow, F. Hassan, Z. Chen, J.Y. Choi, and A. Yu. Graphene-Based Flexible Supercapacitors: Pulse-Electropolymerization

of Polypyrrole on Free-Standing Graphene Films. *The Journal of Physical Chemistry C*, 115(35):17612–17620, 2011.

[94] J. Wang, Y. Xu, J. Wang, X. Du, F. Xiao, and J. Li. High charge/discharge rate polypyrrole films prepared by pulse current polymerization. *Synthetic Metals*, 160(17-18):1826–1831, 2010.

[95] M.S. Kiani, N.V. Bhat, F.J. Davis, and G.R. Mitchell. Highly anisotropic electrically conducting films based on polypyrrole. *Polymer*, 33(19):4113–4120, 1992.

[96] C.I. Awuzie. Conducting Polymers. *Materials Today: Proceedings*, 4(4, Part E): 5721–5726, 2017.

[97] X. Guo and A. Facchetti. The journey of conducting polymers from discovery to application. *Nature Materials*, 19(9):922–928, 2020.

[98] H. Talbi, P.E. Just, and L. Dao. Electropolymerization of aniline on carbonized polyacrylonitrile aerogel electrodes: Applications for supercapacitors. *Journal of Applied Electrochemistry*, 33(6):465–473, 2003.

[99] Z. Sun, J. Zhang, F. Ye, W. Wang, G. Wang, Z. Zhang, S. Li, Y. Zhou, and J. Cai. Vulcanization treatment: An effective way to improve the electrochemical cycle stability of polyaniline in supercapacitors. *Journal of Power Sources*, 443:227246, 2019.

[100] P.A. Anquetil, H.H. Yu, J.D. Madden, T.M. Swager, and I.W. Hunter. Recent Advances in Thiophene Based Molecular Actuators. In *Smart Structures and Materials 2003: Electroactive Polymer Actuators and Devices (EAPAD)*, volume 5051, pages 42–53. International Society for Optics and Photonics, 2003.

[101] M. Heeney, C. Bailey, K. Genevicius, M. Shkunov, D. Sparrowe, S. Tierney, and I. McCulloch. Stable Polythiophene Semiconductors Incorporating Thieno[2,3-b]thiophene. *Journal of the American Chemical Society*, 127(4):1078–1079, 2005.

[102] B. Yan, Y. Wu, and L. Guo. Recent advances on polypyrrole electroactuators. *Polymers*, 9(9):446, 2017.

[103] A. Della Santa, D. De Rossi, and A. Mazzoldi. Performance and work capacity of a polypyrrole conducting polymer linear actuator. *Synthetic Metals*, 90(2): 93–100, 1997.

[104] Z. Tetsuji, H. Susumu, T. Wataru, and K. Keiichi. Comparison of Conducting Polymer Actuators Based on Polypyrrole Doped with BF4-, PF6-, CF3SO3-, and ClO4-. *Bulletin of the Chemical Society of Japan*, 78(3):506–511, 2005.

[105] J.D. Larson, C.V. Fengel, N.P. Bradshaw, I.S. Romero, J.M. Leger, and A.R. Murphy. Enhanced actuation performance of silk-polypyrrole composites. *Materials Chemistry and Physics*, 186:67–74, 2017.

[106] S.H. Lee, C.K. Lee, S.R. Shin, B.K. Gu, S.I. Kim, T.M. Kang, and S.J. Kim. Enhanced actuation of PPy/CNT hybrid fibers using porous structured DNA hydrogel. *Sensors and Actuators B: Chemical*, 145(1):89–92, 2010.

[107] W. Zheng, P.G. Whitten, and G.M. Spinks. Polypyrrole actuators: the effects of polymer thickness and voltage scan rate on fractional charging and isotonic actuation strain. *Multifunctional Materials*, 1(1):014002, 2018.

[108] A. Kesküla, A.L. Peikolainen, R. Kiefer, and T. Tamm. Consistent response from conducting polymer actuators: Potential window and embedded charges to avoid mixed ion transport. *Synthetic Metals*, 268:116502, 2020.

[109] T.W. Lewis, G.G. Wallace, C.Y. Kim, and D.Y. Kim. Studies of the overoxidation of polypyrrole. *Synthetic Metals*, 84(1):403–404, 1997.

[110] T.I.W. Schnoor, U. Vainio, L.H. Shao, E.T. Lilleodden, M. Müller, A. Schreyer, K. Schulte, and B. Fiedler. Nanostructured MWCNT/Polypyrrole Actuators with Anisotropic Strain Response. *Advanced Engineering Materials*, 18(4):597–607, 2016.

[111] T. Shimidzu, A. Ohtani, T. Iyoda, and K. Honda. Charge-controllable polypyrrole/polyelectrolyte composite membranes: Part II. Effect of incorporated anion size on the electrochemical oxidation-reduction process. *Journal of Electroanalytical Chemistry and Interfacial Electrochemistry*, 224(1-2):123–135, 1987.

[112] P. Chiarelli, A.D. Santa, D. de Rossi, and A. Mazzoldi. Actuation Properties of Electrochemically Driven Polypyrrole Free-Standing Films. *Journal of Intelligent Material Systems and Structures*, 6(1):32–37, 1995.

[113] M. Satoh, K. Kaneto, and K. Yoshino. Dependences of electrical and mechanical properties of conducting polypyrrole films on conditions of electrochemical polymerization in an aqueous medium. *Synthetic Metals*, 14(4):289–296, 1986.

[114] K. Kaneto. Research Trends of Soft Actuators based on Electroactive Polymers and Conducting Polymers. In *Journal of physics: conference series*, volume 704, page 012004. IOP Publishing, 2016.

[115] I. McCue, E. Benn, B. Gaskey, and J. Erlebacher. Dealloying and dealloyed materials. *Annual Review of Materials Research*, 46:263–286, 2016.

[116] T. Wada, K. Yubuta, A. Inoue, and H. Kato. Dealloying by metallic melt. *Materials Letters*, 65(7):1076–1078, 2011.

[117] Z. Lu, C. Li, J. Han, F. Zhang, P. Liu, H. Wang, Z. Wang, C. Cheng, L. Chen, and A. Hirata. Three-dimensional bicontinuous nanoporous materials by vapor phase dealloying. *Nature Communications*, 9(1):1–7, 2018.

[118] S. Parida, D. Kramer, C. Volkert, H Rösner, J. Erlebacher, and J. Weissmüller. Volume change during the formation of nanoporous gold by dealloying. *Physical Review Letters*, 97(3):035504, 2006.

[119] N.A. Senior and R.C. Newman. Synthesis of tough nanoporous metals by controlled electrolytic dealloying. *Nanotechnology*, 17(9):2311, 2006.

[120] A.A. Vega and R.C. Newman. Nanoporous metals fabricated through electrochemical dealloying of Ag-Au-Pt with systematic variation of Au: Pt ratio. *Journal of the Electrochemical Society*, 161(1):C1, 2013.

[121] K. Sieradzki, R.R. Corderman, K. Shukla, and R.C. Newman. Computer simulations of corrosion: Selective dissolution of binary alloys. *Philosophical Magazine A*, 59(4):713–746, 1989.

[122] D. Artymowicz, J. Erlebacher, and R. Newman. Relationship between the parting limit for de-alloying and a particular geometric high-density site percolation threshold. *Philosophical Magazine*, 89(21):1663–1693, 2009.

[123] H.W. Pickering and P.J. Byrne. On Preferential Anodic Dissolution of Alloys in the Low-Current Region and the Nature of the Critical Potential. *Journal of the Electrochemical Society*, 118(2):209, 1971.

[124] J.D. Fritz and H.W. Pickering. Selective Anodic Dissolution of Cu-Au Alloys: TEM and Current Transient Study. *Journal of the Electrochemical Society*, 138 (11):3209, 1991.

[125] J. Erlebacher and K. Sieradzki. Pattern formation during dealloying. *Scripta Materialia*, 49(10):991–996, 2003.

[126] J. Erlebacher. An atomistic description of dealloying: Porosity evolution, the critical potential, and rate-limiting behavior. *Journal of the Electrochemical Society*, 151(10):C614, 2004.

[127] Y. Li, B.N.D. Ngô, J. Markmann, and J. Weissmller. Topology evolution during coarsening of nanoscale metal network structures. *Physical Review Materials*, 3 (7):076001, 2019.

[128] T. Krekeler, A.V. Straßer, M. Graf, K. Wang, C. Hartig, M. Ritter, and J. Weissmüller. Silver-rich clusters in nanoporous gold. *Materials Research Letters*, 5(5):314–321, 2017.

[129] A. El-Zoka, B. Langelier, G. Botton, and R. Newman. Morphological evolution of Pt-modified nanoporous gold after thermal coarsening in reductive and oxidative environments. *npj Materials Degradation*, 4(1):1–6, 2020.

[130] Y.C.K. Chen-Wiegart, S. Wang, Y.S. Chu, W. Liu, I. McNulty, P.W. Voorhees, and D.C. Dunand. Structural evolution of nanoporous gold during thermal coarsening. *Acta Materialia*, 60(12):4972–4981, 2012.

[131] S. Kuwano-Nakatani, T. Fujita, K. Uchisawa, D. Umetsu, Y. Kase, Y. Kowata, K. Chiba, T. Tokunaga, S. Arai, and Y. Yamamoto. Environment-sensitive thermal coarsening of nanoporous gold. *Materials Transactions*, page MF201403, 2015.

[132] S. Sadki, P. Schottland, N. Brodie, and G. Sabouraud. The mechanisms of pyrrole electropolymerization. *Chemical Society Reviews*, 29(5):283–293, 2000.

[133] N. Yi and M.R. Abidian. Conducting polymers and their biomedical applications. In *Biosynthetic Polymers for Medical Applications*, pages 243–276. Woodhead Publishing, 2016.

[134] E. Genies, G. Bidan, and A. Diaz. Spectroelectrochemical study of polypyrrole films. *Journal of Electroanalytical Chemistry and Interfacial Electrochemistry*, 149(1-2):101–113, 1983.

[135] G.G. Wallace, P.R. Teasdale, G.M. Spinks, and L.A. Kane-Maguire. *Chapter 2 - Synthesis and structure of Polypyrroles*. CRC press, 2002.

[136] S.J. Sutton and A.S. Vaughan. On the morphology and growth of electrochemically polymerized polypyrrole. *Polymer*, 36(9):1849–1857, 1995.

[137] W. Zheng, J.M. Razal, G.M. Spinks, V.T. Truong, P.G. Whitten, and G.G. Wallace. The Role of Unbound Oligomers in the Nucleation and Growth of Electrodeposited Polypyrrole and Method for Preparing High Strength, High Conductivity Films. *Langmuir*, 28(29):10891–10897, 2012.

[138] R.H. Geiss, G.B. Street, W. Volksen, and J. Economy. Polymer structure determination using electron diffraction techniques. *IBM Journal of Research and Development*, 27(4):321–329, 1983.

[139] C. Alemán, J. Casanovas, J. Torras, O. Bertrán, E. Armelin, R. Oliver, and F. Estrany. Cross-linking in polypyrrole and poly(N-methylpyrrole): Comparative experimental and theoretical studies. *Polymer*, 49(4):1066–1075, 2008.

[140] T.F. Otero. *Conducting polymers, electrochemistry, and biomimicking processes*. Springer, 2002.

[141] B.J. Hwang, D.T. Shieh, W.C. Chieh, D.J. Liaw, and L.J. Li. Electropolymerization of pyrrole and 4-(3-Pyrrolyl)butane-sulfonate on Pt substrate: An in situ EQCM study. *Thin Solid Films*, 301(1):175–182, 1997.

[142] B. Roschning and J. Weissmüller. Stress-charge coupling coefficient for thin-film polypyrrole actuators - Investigation of capacitive ion exchange in the oxidized state. *Electrochimica Acta*, 318:504–512, 2019.

[143] K.E. Heusler and K. Suk Yun. Electron transfer reactions at film covered metal electrodes. *Electrochimica Acta*, 22(9):977–986, 1977.

[144] V. Ho, A.G. Narenji, L. Kulinsky, and M. Madou. The detachment process and release efficiency of polypyrrole/gold bilayer actuators. *Journal of Microelectromechanical Systems*, 24(5):1616–1621, 2015.

[145] Y. Hou, L.Y. Chen, L. Zhang, J.L. Kang, T. Fujita, J.H. Jiang, and M.W. Chen. Ultrahigh capacitance of nanoporous metal enhanced conductive polymer pseudocapacitors. *Journal of Power Sources*, 225:304–310, 2013.

[146] Y. Hou, L.Y. Chen, P. Liu, J.L Kang, T. Fujita, and M.W. Chen. Nanoporous metal based flexible asymmetric pseudocapacitors. *Journal of Materials Chemistry A*, 2(28):10910–10916, 2014.

[147] M. Salmon, A.F. Diaz, A.J. Logan, M. Krounbi, and J. Bargon. Chemical modification of conducting polypyrrole films. *Molecular Crystals and Liquid Crystals*, 83(1):265–276, 1982.

[148] R. Ansari. Polypyrrole conducting electroactive polymers: Synthesis and stability studies. *E-Journal of Chemistry*, 3(4):186–201, 2006.

[149] S.J. Dong and J. Ding. Study on polypyrrole film by electrochemical polymerization in aqueous solution. *Synthetic Metals*, 20(1):119–124, 1987.

[150] J. Bonastre, R. Lapuente, P. Garcés, and F. Cases. Electrochemical and chemical characterization of polypyrrole/phosphotungstate coatings electrosynthesized on carbon steel electrodes in acetonitrile medium. *Synthetic Metals*, 159(17):1723–1730, 2009.

[151] K.A. Noh, D.W. Kim, C.S. Jin, K.H. Shin, J.H. Kim, and J.M. Ko. Synthesis and pseudo-capacitance of chemically-prepared polypyrrole powder. *Journal of Power Sources*, 124(2):593–595, 2003.

[152] A.F. Diaz and B. Hall. Mechanical properties of electrochemically prepared polypyrrole films. *IBM Journal of Research and Development*, 27(4):342–347, 1983.

[153] M. Zhou and J. Heinze. Electropolymerization of pyrrole and electrochemical study of polypyrrole. 3. Nature of "water effect" in acetonitrile. *The Journal of Physical Chemistry B*, 103(40):8451–8457, 1999.

[154] T.F. Otero and M. Bengoechea. UV-Visible Spectroelectrochemistry of Conducting Polymers. Energy Linked to Conformational Changes. *Langmuir*, 15(4): 1323–1327, 1999.

[155] L.F. Warren and D.P. Anderson. Polypyrrole Films from Aqueous Electrolytes: the Effect of Anions upon Order. *Journal of The Electrochemical Society*, 134 (1):101–105, 2019.

[156] F. Mohammad. Comparative studies on diffusion behaviour of electrochemically prepared polythiophene and polypyrrole: Effect of ionic size of dopant. *Synthetic Metals*, 99(2):149–154, 1999.

[157] Y.F. Li and J. Yang. Effect of electrolyte concentration on the properties of the electropolymerized polypyrrole films. *Journal of Applied Polymer Science*, 65 (13):2739–2744, 1997.

[158] J. Rodriguez, T.F. Otero, H. Grande, J. Moliton, A. Moliton, and T. Trigaud. Optimization of the electrical conductivity of polypyrrole films electrogenerated on aluminium electrodes. *Synthetic Metals*, 76(1-3):301–303, 1996.

[159] E.L. Kupila and J. Kankare. Electropolymerization of pyrrole: Effects of pH and anions on the conductivity and growth kinetics of polypyrrole. *Synthetic Metals*, 55(2-3):1402–1405, 1993.

[160] A. Kassim, Z.B. Basar, and H.E. Mahmud. Effects of preparation temperature on the conductivity of polypyrrole conducting polymer. *Journal of Chemical Sciences*, 114(2):155–162, 2002.

[161] L.M. Dai. *Conducting Polymers*, pages 41–80. Springer London, London, 2004.

[162] T.H. Le, Y. Kim, and H. Yoon. Electrical and electrochemical properties of conducting polymers. *Polymers*, 9(4):150, 2017.

[163] J.L. Bredas and G.B. Street. Polarons, bipolarons, and solitons in conducting polymers. *Accounts of Chemical Research*, 18(10):309–315, 1985.

[164] L.Z. Fan and J. Maier. High-performance polypyrrole electrode materials for redox supercapacitors. *Electrochemistry Communications*, 8(6):937–940, 2006.

[165] Q.J. Xie, S. Kuwabata, and H. Yoneyama. EQCM studies on polypyrrole in aqueous solutions. *Journal of Electroanalytical Chemistry*, 420(1):219–225, 1997.

[166] K.C. Tsay, L. Zhang, and J.J. Zhang. Effects of electrode layer composition/thickness and electrolyte concentration on both specific capacitance and energy density of supercapacitor. *Electrochimica Acta*, 60:428–436, 2012.

[167] J. Guay, R. Paynter, and L.H. Dao. Synthesis and characterization of poly (diarylamines): A new class of electrochromic conducting polymers. *Macromolecules*, 23(15):3598–3605, 1990.

[168] D.Y. Qu. Studies of the activated carbons used in double-layer supercapacitors. *Journal of Power Sources*, 109(2):403–411, 2002.

[169] M. Grden. The interfacial capacitance of an oxidised polycrystalline gold electrode in an aqueous HClO4 electrolyte. *Thin Solid Films*, 545:332–340, 2013.

[170] P. Sharma and T.S. Bhatti. A review on electrochemical double-layer capacitors. *Energy Conversion and Management*, 51(12):2901–2912, 2010.

[171] X.Y. Lang, H.T. Yuan, Y. Iwasa, and M.W. Chen. Three-dimensional nanoporous gold for electrochemical supercapacitors. *Scripta Materialia*, 64(9):923–926, 2011.

[172] B.E. Conway. *Electrochemical supercapacitors: Scientific fundamentals and technological applications*. Springer Science & Business Media, 2013.

[173] S. Wang, B. Hsia, C. Carraro, and R. Maboudian. High-performance all solid-state micro-supercapacitor based on patterned photoresist-derived porous carbon electrodes and an ionogel electrolyte. *Journal of Materials Chemistry A*, 2(21): 7997–8002, 2014.

[174] C. Costentin, T.R. Porter, and J.M. Saveant. How do pseudocapacitors store energy? Theoretical analysis and experimental illustration. *ACS Applied Materials & Interfaces*, 9(10):8649–8658, 2017.

[175] Y. Gogotsi and R.M. Penner. Energy Storage in Nanomaterials - Capacitive, Pseudocapacitive, or Battery-like? *ACS Nano*, 12(3):2081–2083, 2018.

[176] M. Forghani and S.W. Donne. Method comparison for deconvoluting capacitive and pseudo-capacitive contributions to electrochemical capacitor electrode behavior. *Journal of The Electrochemical Society*, 165(3):A664, 2018.

[177] K. Dawson, A. Wahl, A. Pescaglini, D. Iacopino, and A. O'Riordan. Gold nanowire electrode arrays: Investigations of non-faradaic behavior. *Journal of the Electrochemical Society*, 161(2):B3049, 2013.

[178] A. Ray, A. Roy, S. Saha, and S. Das. Transition metal oxide-based nano-materials for energy storage application. *Science, Technology and Advanced Application of Supercapacitors*, pages 1–17, 2019.

[179] J. Tamm, A. Hallik, A. Alumaa, and V. Sammelselg. Electrochemical properties of polypyrrole/sulphate films. *Electrochimica Acta*, 42(19):2929–2934, 1997.

[180] K. Kaneto, F. Hata, and S. Uto. Structure and size of ions electrochemically doped in conducting polymer. *Journal of Micromechanics and Microengineering*, 28(5):054003, 2018.

[181] T.F. Otero. Soft, wet, and reactive polymers. Sensing artificial muscles and conformational energy. *Journal of Materials Chemistry*, 19(6):681–689, 2009.

[182] K. Kaneto, Y. Sonoda, and W. Takashima. Direct measurement and mechanism of electro-chemomechanical expansion and contraction in polypyrrole films. *Japanese Journal of Applied Physics*, 39(10R):5918, 2000.

[183] T.F. Otero, H.J. Grande, and J. Rodrĺguez. Reinterpretation of polypyrrole electrochemistry after consideration of conformational relaxation processes. *The Journal of Physical Chemistry B*, 101(19):3688–3697, 1997.

[184] T.F. Otero and H. Grande. Thermally enhanced conformational relaxation during electrochemical oxidation of polypyrrole. *Journal of Electroanalytical Chemistry*, 414(2):171–176, 1996.

[185] L. Bay, T. Jacobsen, S. Skaarup, and K. West. Mechanism of actuation in conducting polymers: Osmotic expansion. *The Journal of Physical Chemistry B*, 105(36):8492–8497, 2001.

[186] S. Skaarup, N. Mogensen, L. Bay, and K. West. Polypyrrole actuators for tremor suppression. In *Smart Structures and Materials 2003: Electroactive Polymer Actuators and Devices (EAPAD)*, volume 5051, pages 423–428. International Society for Optics and Photonics, 2003.

[187] Y. Velmurugu and S. Skaarup. Ion and solvent transport in polypyrrole: Experimental test of osmotic model. *Ionics*, 11(5-6):370–374, 2005.

[188] M. Kertész, F. Vonderviszt, and S. Pekker. Change of geometry of polyacetylene upon charge transfer. *Chemical Physics Letters*, 90(6):430–433, 1982.

[189] R.H. Baughman. Conducting polymer artificial muscles. *Synthetic Metals*, 78(3): 339–353, 1996.

[190] F. Larché and J.W. Cahn. A linear theory of thermochemical equilibrium of solids under stress. *Acta Metallurgica*, 21(8):1051–1063, 1973.

[191] S. Shi. *Chemo-mechanical Coupling in Nanoporous Palladium-hydrogen.* Thesis, Technische Universität Hamburg, 2019.

[192] F.L. Tian, Y.and Yang and W.S. Yang. Redox behavior and stability of polypyrrole film in sulfuric acid. *Synthetic Metals*, 156(16):1052–1056, 2006.

[193] K. Wang. *Composites of Nanoporous Gold and Polymer*. Thesis, Technische Universität Hamburg, 2015.

[194] R. Bilewicz, R.A. Osteryoung, and J. Osteryoung. Comparison of linear scan and staircase voltammetry: Experimental results. *Analytical Chemistry*, 58(13): 2761–2765, 1986.

[195] A.W. Bott. A comparison of cyclic voltammetry and cyclic staircase voltammetry. *Current Separations*, 16:23–26, 1997.

[196] C. Montella. Further investigation of the equivalence of staircase and linear scan voltammograms. III-averaged-current staircase voltammetry applied to electrochemical reactions involving adsorbed species. *Journal of Electroanalytical Chemistry*, 808:348–361, 2018.

[197] A. Izadi-Najafabadi, D.T. Tan, and J.D. Madden. Towards high power polypyrrole/carbon capacitors. *Synthetic Metals*, 152(1-3):129–132, 2005.

[198] F.E. Chen, G.Q. Shi, M.X. Fu, L.T. Qu, and X.Y. Hong. Raman spectroscopic evidence of thickness dependence of the doping level of electrochemically deposited polypyrrole film. *Synthetic Metals*, 132(2):125–132, 2003.

[199] K.S. Teh, Y. Takahashi, Z. Yao, and Y.W. Lu. Influence of redox-induced restructuring of polypyrrole on its surface morphology and wettability. *Sensors and Actuators A: Physical*, 155(1):113–119, 2009.

[200] H. Grande, T.F. Otero, and J. Rodriguez. Optimization of electrical and redox properties of electrogenerated polypyrroles. *PLASTICS ENGINEERING-NEW YORK-*, 45:17–46, 1998.

[201] F. Beck, R. Michaelis, F. Schloten, and B. Zinger. Filmforming electropolymerization of pyrrole on iron in aqueous oxalic acid. *Electrochimica Acta*, 39(2): 229–234, 1994.

[202] C. Cassignol, P. Olivier, and A. Ricard. Influence of the dopant on the polypyrrole moisture content: Effects on conductivity and thermal stability. *Journal of Applied Polymer Science*, 70(8):1567–1577, 1998.

[203] A. Hallik, H. Roosalu, K.and Mändar, L. Joosu, M. Marandi, and J. Tamm. Thickness dependence of the porosity of PPy/DDS films. *European Polymer Journal*, 70:118–124, 2015.

[204] M. Hepel. The electrocatalytic oxidation of methanol at finely dispersed platinum nanoparticles in polypyrrole films. *Journal of the Electrochemical Society*, 145 (1):124, 1998.

[205] M.A. Genshaw, A. Damjanovic, and J.O.M. Bockris. Hydrogen peroxide formation in oxygen reduction at gold electrodes: I. Acid solution. *Journal of Electroanalytical Chemistry and Interfacial Electrochemistry*, 15:163–172, 1967.

[206] S. Trasatti and O.A. Petrii. Real surface area measurements in electrochemistry. *Pure and Applied Chemistry*, 63(5):711–734, 1991.

[207] Y. Zhong, J. Markmann, H.J. Jin, Y. Ivanisenko, L. Kurmanaeva, and J. Weissmüller. Crack Mitigation during Dealloying of Au25Cu75. *Advanced Engineering Materials*, 16(4):389–398, 2014.

[208] P.S. Germain, W.G. Pell, and B.E. Conway. Evaluation and origins of the difference between double-layer capacitance behaviour at Au-metal and oxidized Au surfaces. *Electrochimica Acta*, 49(11):1775–1788, 2004.

[209] U.E. Zhumaev, A.S. Lai, I.V. Pobelov, A. Kuzume, A.V. Rudnev, and T. Wandlowski. Quantifying perchlorate adsorption on Au(111) electrodes. *Electrochimica Acta*, 146:112–118, 2014.

[210] N. Mameka, K. Wang, J. Markmann, E.T. Lilleodden, and J. Weissmüller. Nanoporous gold-testing macro-scale samples to probe small-scale mechanical behavior. *Materials Research Letters*, 4(1):27–36, 2016.

[211] C. Mahr, P. Kundu, A. Lackmann, D. Zanaga, K. Thiel, M. Schowalter, M. Schwan, S. Bals, A. Wittstock, and A. Rosenauer. Quantitative determination of residual silver distribution in nanoporous gold and its influence on structure and catalytic performance. *Journal of Catalysis*, 352:52–58, 2017.

[212] H. Fu, Z.J. Du, W. Zou, H.Q. Li, and C. Zhang. Carbon nanotube reinforced polypyrrole nanowire network as a high-performance supercapacitor electrode. *Journal of Materials Chemistry A*, 1(47):14943–14950, 2013.

[213] Y.H. Xue, J. Markmann, H.L. Duan, J. Weissmüller, and P. Huber. Switchable imbibition in nanoporous gold. *Nature Communications*, 5(1):1–8, 2014.

[214] S.J. HHahn, W.E. Stanchina, W.J. Gajda, and P. Vogelhut. The effect of growth rate variation on the conductivity and morphology of polypyrrole thin films. *Journal of Electronic Materials*, 15(3):145–149, 1986.

[215] M.N. Akieh, W.E. Price, J. Bobacka, A. Ivaska, and S.F. Ralph. Ion exchange behaviour and charge compensation mechanism of polypyrrole in electrolytes containing mono-, di-and trivalent metal ions. *Synthetic metals*, 159(23-24):2590–2598, 2009.

[216] Z.L. Wang, S.C. Ning, P. Liu, Y. Ding, A. Hirata, T. Fujita, and M.W. Chen. Tuning Surface Structure of 3D Nanoporous Gold by Surfactant-Free Electrochemical Potential Cycling. *Advanced Materials*, 29(41):1703601, 2017.

[217] K. Kakaei, M.D. Esrafili, and A. Ehsani. Graphene-Based Electrochemical Supercapacitors. In *Interface Science and Technology*, volume 27, pages 339–386. Elsevier, 2019.

[218] I.J. Suárez, T.F. Otero, and M. Márquez. Diffusion Coefficients in Swelling Polypyrrole: ESCR and Cottrell Models. *The Journal of Physical Chemistry B*, 109(5):1723–1729, 2005.

[219] M. Gsell, P. Jakob, and D. Menzel. Effect of Substrate Strain on Adsorption. *Science*, 280(5364):717, 1998.

[220] Y.D. Jin and S.J. Dong. Probing UPD-Induced Surface Atomic Rearrangement of Polycrystalline Gold Nanofilms with Surface Plasmon Resonance Spectroscopy and Cyclic Voltammetry. *The Journal of Physical Chemistry B*, 107(50):13969–13975, 2003.

[221] A.S. Hutchison, T.W. Lewis, S.E. Moulton, G.M. Spinks, and G.G. Wallace. Development of polypyrrole-based electromechanical actuators. *Synthetic Metals*, 113(1):121–127, 2000.

[222] G.M. Spinks, D. Zhou, L. Liu, and G.G. Wallace. The amounts per cycle of polypyrrole electromechanical actuators. *Smart Materials and Structures*, 12(3): 468, 2003.

[223] G.M. Spinks, T.E. Campbell, and G.G. Wallace. Force generation from polypyrrole actuators. *Smart Materials and Structures*, 14(2):406, 2005.

[224] M.R. Warren and J.D. Madden. A structural, electronic and electrochemical study of polypyrrole as a function of oxidation state. *Synthetic Metals*, 156(9-10):724–730, 2006.

[225] T.F. Otero. Coulovoltammetric and dynamovoltammetric responses from conducting polymers and bilayer muscles as tools to identify reaction-driven structural changes. A review. *Electrochimica Acta*, 212:440–457, 2016.

[226] C. Song and J. Zhang. *Electrocatalytic oxygen reduction reaction*, pages 89–134. Springer, 2008.

[227] A.M. Hodge, J. Biener, J.R. Hayes, P.M. Bythrow, C.A. Volkert, and A.V. Hamza. Scaling equation for yield strength of nanoporous open-cell foams. *Acta Materialia*, 55(4):1343–1349, 2007.

[228] C.A. Volkert, E.T. Lilleodden, D. Kramer, and J. Weissmüller. Approaching the theoretical strength in nanoporous Au. *Applied Physics Letters*, 89(6):061920, 2006.

[229] N.J. Briot and T.J. Balk. Developing scaling relations for the yield strength of nanoporous gold. *Philosophical Magazine*, 95(27):2955–2973, 2015.

[230] I.J. Gibson and M.F. Ashby. The mechanics of three-dimensional cellular materials. *Proceedings of the Royal Society of London. A. Mathematical and Physical Sciences*, 382(1782):43–59, 1982.

[231] H.J. Jin, J. Weissmüller, and D. Farkas. Mechanical response of nanoporous metals: A story of size, surface stress, and severed struts. *MRS Bulletin*, 43(1): 35, 2018.

[232] P. Murray, G.M. Spinks, G.G. Wallace, and R.P. Burford. Electrochemical induced ductile-brittle transition in tosylate-doped (pTS) polypyrrole. *Synthetic Metals*, 97(2):117–121, 1998.

[233] M. Gandhi, G.M. Spinks, R.P. Burford, and G.G. Wallace. Film substructure and mechanical properties of electrochemically prepared polypyrrole. *Polymer*, 36(25):4761–4765, 1995.

[234] W. Plieth. *Electrochemistry for materials science*. Elsevier, 2008.

[235] Y. Tezuka, S. Ohyama, T. Ishii, and K. Aoki. Observation of propagation speed of conductive front in electrochemical doping process of polypyrrole films. *Bulletin of the Chemical Society of Japan*, 64(7):2045–2051, 1991.

[236] Y. Tezuka and K. Aoki. Direct demonstration of the propagation theory of a conductive zone in a polypyrrole film by observing temporal and spatial variations of potentials at addressable microband array electrodes. *Journal of Electroanalytical Chemistry*, 273(1-2):161–168, 1989.

[237] W. Zheng. *Analysis of high performance polypyrrole actuators*. Thesis, University of Wollongong, 2011.

[238] B. Sun, J. Jones, R. Burford, and M. Skyllas-Kazacos. Stability and mechanical properties of electrochemically prepared conducting polypyrrole films. *Journal of Materials Science*, 24(11):4024–4029, 1989.

[239] P.V. Pillai, I.W. Hunter, and E. Hernandez. Application of stochastic system identification to the study of the compliance of electroactive polymers. *Review of Scientific Instruments*, 82(2):025103, 2011.

[240] S. Murakami, K. Senoo, S. Toki, and S. Kohjiya. Structural development of natural rubber during uniaxial stretching by in situ wide angle X-ray diffraction using a synchrotron radiation. *Polymer*, 43(7):2117–2120, 2002.